Int. J. Advanced Design and Manufacturing Technology, 2025, Vol. 18, No. 1, pp. 1-5

DOI: *ISSN: 2252-0406* *https://admt.isfahan.iau.ir*

Modified Lattice Structure with Close-To-Zero Poisson's Ratio for Enhanced Energy Absorption: A Numerical Study

Abolfazl Sharifi *
Department of Mechanical Engineering,
Shahid Bahonar university of technology, Kerman, Iran
E-mail: abolfazlsharifi587@gmail.com
*Corresponding author

Received: 23 July 2024, Revised: 16 October 2024, Accepted: 11 December 2024

Abstract: Lattice structures have garnered significant interest across various sectors due to their unique characteristics, such as a high strength-to-weight ratio and a high damping coefficient. In addition, honeycomb structures necessitate a zero Poisson's ratio to prevent unnecessary stress and strain. To address this issue, a cellular honeycomb core that incorporates in-plane corrugated U-shaped beams with close-to-zero Poisson's ratio was proposed. This research assesses a method to increase the capacity of structure to absorb energy. To achieve this goal, a circular cylinder was utilized to improve the mechanical properties. The compressive characteristics of the modified structure were analyzed and compared to the conventional structure. The objective of this study was to boost the energy absorption capabilities of the conventional structure while maintaining the Poisson's ratio.

Keywords: Energy Absorption, Finite Element Analysis, Lattice Structure, Poisson's Ratio

Biographical notes: Abolfazl Sharifi received his BSc degree in mechanical engineering from Shahid Bahonar University of Technology, Kerman, Iran, in 2018. He is currently a member of the research group at the Panganco, Kerman, Iran. His current research interest includes lattice structure and Finite element analysis.

Research paper

1 INTRODUCTION

Researchers have extensively attempted to modify the current existing structures' geometric parameters or introduce new structures in the hope of enhancing mechanical performance [1-2]. The cellular metastructure stands out for its ability to achieve a range of exceptional characteristics such as being lightweight and high strength, exhibiting negative expansion [3], negative stiffness, zero Poisson's ratio [4], compression-torsion coupling, and multi-stability [5]. These features are crucial in military, aerospace, medical, and other industries. The traditional hexagonal and re-entrant honeycombs, known for their positive and negative Poisson's ratio, have been commonly utilized in various industries. Many studies have been carried out to examine their elastic and nonlinear mechanical characteristics using theoretical approaches, finite element methods, and experimental studies [6-11]. Dong et al. [12] Combined 2D similar re-entrant with conventional re-entrant structure (CRS) to create a new self-similar re-entrant auxetic metamaterial(SREAM) and studied the mechanical characteristics of SREAM and CRS under quasi-stratic compression test. The experimental and finite element results show that SREAM achieves better mechanical stability than CRS because of increased stiffness while maintaining the comparatively good negative Poisson's ratio. Choudhry et al. [13] demonstrated the in-plane energy absorption characteristics of a modified re-entrant auxetic honeycomb. According to their analysis, adding more nodes with low rotational stiffness increased the modified re-entrant structure's failure strain and enhanced its capacity to absorb energy. Chen et al. [14] proposed a novel auxetic honeycomb structure by incorporating self-similar inclusion into the conventional re-entrant structure. In comparison to the original construction, the new re-entrant honeycomb shows improved auxeticity and stiffness. The new auxetic structure has a specific energy absorption that is approximately ten times greater than the previous structure. Materials with Zero Poisson's ratio (ZPR) maintain constant transverse width under longitudinal strain. Instead of changing the chemical composition of materials, a lot of engineering effort is concentrated on creating micro-structural architectures to change the mechanical properties of those materials. As a result, meta-material is created, which can have characteristics not present in natural material. However, while some materials, like glasses and corks, exhibit a Poisson's ratio of near zero [15], none of these materials can be used to create lattice structures. Various cellular structures have been developed to meet diverse performance criteria, exhibiting positive, negative, and zero Poisson's ratios. Zero Poisson's ratio(ZPR) structure has not been studied as much as the negative and positive Poisson's ratio (NPR) structure [16]. Chen et al. [17] suggested a new honeycomb by incorporating a rib into each cell of the existing zero Poisson's ratio configuration, semi re-entrant honeycomb. It is demonstrated theoretically, numerically, and experimentally that the new honeycomb has zero Poisson's ratio (ZPR) characteristic. Liu et al. [18] proposed a novel honeycomb structure with zero Poisson's ratio. The findings indicated that by adjusting the geometric parameters, the honeycomb structure's mechanical characteristics can be customized. From the review above, It is evident that researchers have proposed new lattice designs that can enhance the energy absorption of lattice structures. however, few research studies have been done on improving the energy absorption of close-to-zero Poisson's ratio structures while maintaining the Poisson's ratio. This study's main objective is to numerically investigate the in-plane mechanical characteristics of the close-to-zero Poisson's ratio structure. Two lattice structures were designed to examine the correlations between their Load-Displacement curve and Poisson's ratio value. The principal objective of this research is to investigate numerically the in-plane mechanical characteristics of the close-to-zero Poisson's ratio structure. Two lattice structures were designed to examine the correlations between their Load-Displacement curve and Poisson's ratio values.

2 LATTICE STRUCTURE

2.1. The Unit Cell's Geometric Configuration

Regarding structural design, a lattice structure can be formed through the repetition of a unit cell following a specific pattern. Consequently, the design of a lattice structure involves the design of unit cells and patterns. Two lattice structures were selected for this investigation: the U-type structure and the U-type structure with circular cylinder (modified), as displayed in "Fig. 1". These cellular structures comprise a regular pattern of unit cells, as shown in "Fig. 1".

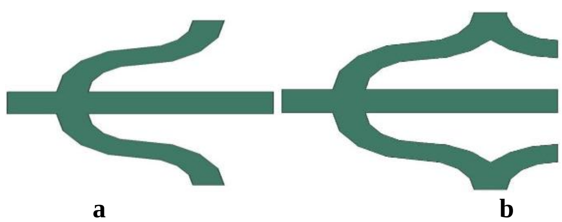

Fig. 1 Unit cells: (a): U-type, and (b): U-type with circular cylinder.

2.2. Energy Absorption

Specimen Energy absorption is the amount of external energy absorbed, which is determined by the force-displacement curve integral:

$$EA = \int_0^d F(x)\,dx \tag{1}$$

Where, d stands for the maximum displacement under compression and F for the compression load, the term "specific energy absorption" describes the amount of absorbed energy per mass, which is determined by dividing the total amount of absorbed energy by the structure's weight.

3 FINITE ELEMENT ANALYSIS

ABAQUS/Standard was employed to simulate the uni-axial compression of the conventional and modified structures. A 2D lattice structure was designed in Abaqus ("Fig. 2"). The global mesh size was set at 0.3 mm and to verify the effect of mesh size, a mesh convergence study was conducted. To apply vertical displacement load, the upper reference point was used. Table 1 presents the geometric parameters of both the conventional and modified lattice structures.
The lattice structure is 50 mm × 47 mm × 20 mm.

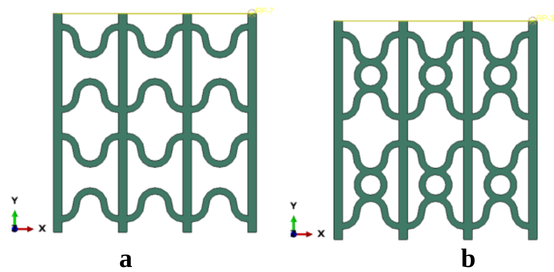

Fig. 2 lattice structures :(a): U-type, and (b): U-type with circular cylinder.

Table 1 Geometrical parameters of the Aluminum structures

structures	Volume	FE.Mass
conventional	15479 mm^3	41.8 g
Modified	17854 mm^3	48.2 g

4 RESULTS

This section compares Poisson's ratio, Load-Displacement curve, and energy absorption of the conventional and modified structures.

4.1. Poisson's Ratio

Zero Poisson's ratio honeycomb structures are the structures that show zero or negligible deformation in the lateral direction when stretched or compressed in the longitudinal direction. The modified structure has a close-to-zero Poisson's ratio and is not sensitive to different displacements. The Poisson ratio of the modified structure is determined through numerical analysis using the displacements of two specific nodes, as shown in "Fig. 3".

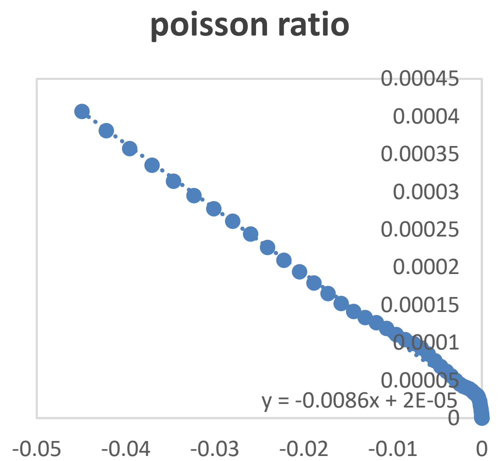

Fig. 3 The Poisson ratio of the modified structure.

4.2. Load-Displacement Curve

The lattice structure is designed to increase energy absorption. In addition, the mechanical characteristics of the lattice structure such as Young's modulus must be at an acceptable level. Figure 4 shows the numerical Load-Displacement curves of the lattice structures. Figure 6 shows Insignificant lateral deformation in the x direction.

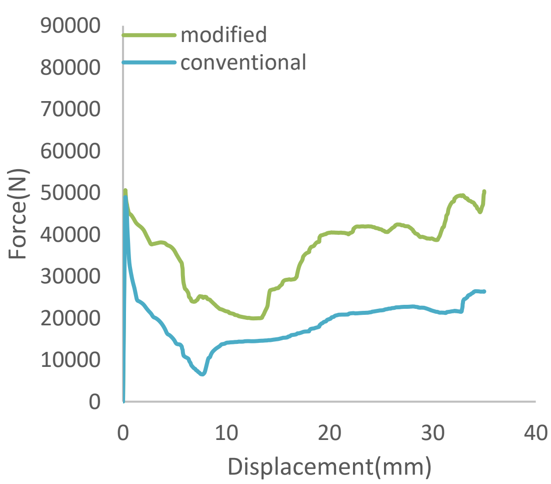

Fig. 4 Comparison of the numerical force–displacement curves of the conventional and modified lattice structures.

4.3. Energy Absorption

In the in-plane compressive analysis, the capacity of structures to absorb energy is a key performance indicator of structure. For this reason, a comparison of energy absorption of two lattice structures is shown in "Fig. 5".

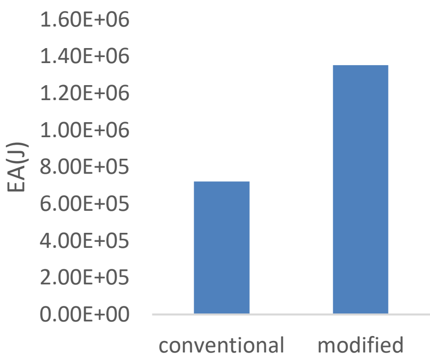

a

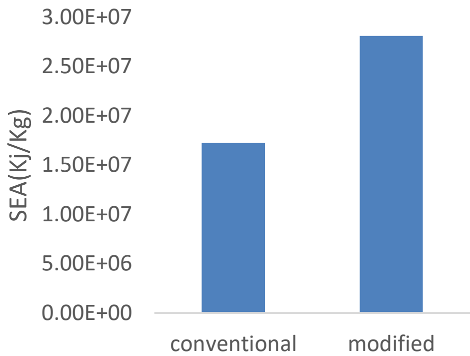

b

Fig. 5 (a): energy absorption of the two structures, and (b): specific energy absorption of the two structures.

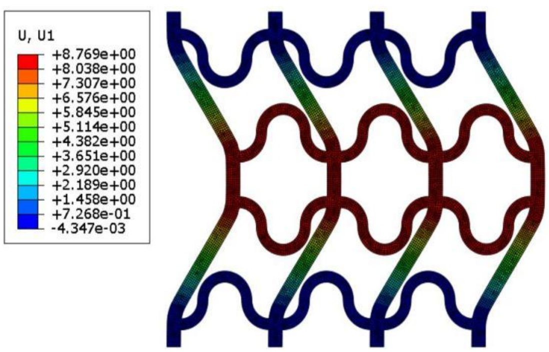

a

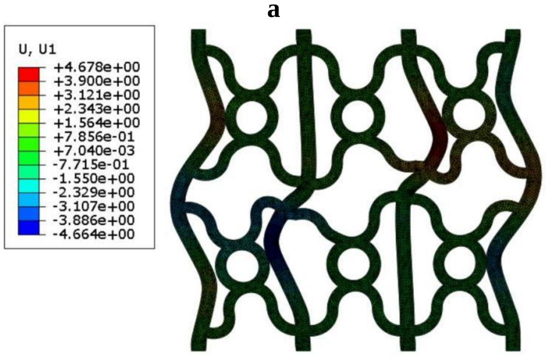

b

Fig. 6 FEA results of two selected configurations: (a): U-type, and (b): U-type with circular cylinder.

Energy absorption (EA) and specific energy absorption (SEA) of the modified structure are 87% and 63% better than the conventional structure, respectively, ("Fig. 6").

7 CONCLUSIONS

This study focused on analyzing the mechanical characteristics of U-type and U-type with circular cylinder (modified) structures through simulation. Aluminum was the chosen material for this investigation. The assessment included the estimation of mechanical properties like energy absorption and Poisson's ratio, revealing that both U-type and modified structures exhibit a Poisson's ratio close to zero. Furthermore, the findings indicated that the structure with a circular cylinder demonstrates higher energy absorption compared to the simple U-type.

REFERENCES

[1] Pan, Y., et al., The Out-of-Plane Compressive Behavior of Auxetic Chiral Lattice with Circular Nodes, Thin-Walled Structures, Vol. 182, 2023, pp. 110152.

[2] Zare Shiadehi, J., Zolfaghari, A., Design Parameters of A Kagome Lattice Structure Constructed by Fused Deposition Modeling: A Response Surface Methodology Study, Iranian Polymer Journal, Vol. 32, No. 9, 2023, pp. 1089-1100.

[3] Saxena, K. K., Das, R., and Calius, E. P.,Three Decades of Auxetics Research− Materials with Negative Poisson's Ratio: A Review, Advanced Engineering Materials, Vol. 18, No. 11, 2016, pp. 1847-1870.

[4] Huang, J., et al., Multi-Stiffness Topology Optimization of Zero Poisson's Ratio Cellular Structures, Composites Part B: Engineering, Vol. 140, 2018, pp. 35-43.

[5] Chi, Y., et al., Bistable and Multistable Actuators for Soft Robots: Structures, Materials, and Functionalities. Advanced Materials, Vol. 34, No. 19, 2022, pp. 2110384.

[6] Ashby, M. F., Gibson, L. J., Cellular Solids: Structure and Properties, Press Syndicate of the University of Cambridge, Cambridge, UK, 1997, pp. 175-231.

[7] Masters, I., Evans, K., Models for the Elastic Deformation of Honeycombs, Composite Structures, Vol. 35, No. 4, 1996, pp. 403-422.

[8] Bitzer, T., Honeycomb Core, in Honeycomb Technology: Materials, Design, Manufacturing, Applications and Testing. 1997, pp. 10-42.

[9] Gibson, L. J., et al., The Mechanics of Two-Dimensional Cellular Materials, Proceedings of the Royal Society of London, Mathematical and Physical Sciences, Vol. 382, No. 1782, 1982, pp. 25-42.

[10] Grediac, M., A Finite Element Study of The Transverse Shear in Honeycomb Cores, International Journal of

Solids and Structures, Vol. 30, No. 13, 1993, pp. 1777-1788.

[11] Abd El-Sayed, F., Jones, R., and Burgess, I., A Theoretical Approach to The Deformation of Honeycomb Based Composite Materials, Composites, Vol. 10, No. 4, 1979, pp. 209-214.

[12] Dong, P., et al., Novel Self-Similar Re-Entrant Auxetic Metamaterials (SREAM): Design, Mechanical Property, and Geometric Optimization, Polymer Testing, Vol. 122, 2023, pp. 108015.

[13] Choudhry, N. K., Panda, B., and Kumar, S., In-Plane Energy Absorption Characteristics of A Modified Re-Entrant Auxetic Structure Fabricated via 3D Printing, Composites Part B: Engineering, Vol. 228, 2022, pp. 109437.

[14] Chen, Z., et al., Enhanced Mechanical Properties of Re-Entrant Auxetic Honeycomb with Self-Similar Inclusion, Composite Structures, Vol. 331, 2024, pp. 117921.

[15] Kojima, S., Poisson’s Ratio of Glasses, Ceramics, and Crystals, Materials, Vol. 17, No. 2, 2024, pp. 300.

[16] Sahariah, B. J., et al., A Novel Strategy to Design Lattice Structures with Zero Poisson’s Ratio, Engineering Structures, Vol. 288, 2023, pp. 116214.

[17] Chen, Y., Fu, M. H., Mechanical Properties of A Novel Zero Poisson's Ratio Honeycomb, Advanced Engineering Materials, Vol. 20, No. 2, 2018, pp. 1700452.

[18] Liu, W., et al., Analyzing In-Plane Mechanics of A Novel Honeycomb Structure with Zero Poisson's Ratio, Thin-Walled Structures, Vol. 192, 2023, pp. 111134.

Int. J. Advanced Design and Manufacturing Technology, 2025, Vol. 18, No. 1, pp. 7-15
DOI: *ISSN: 2252-0406* *https://admt.isfahan.iau.ir*

Innovative Trajectory Planning of a Marker Robot on Steel Coils and Slabs

Mohammad Sajjad Mahdieh*
Department of Mechanical Engineering,
Shahid Chamran University of Ahvaz, Ahvaz, Iran
E-mail: s.mahdieh@scu.ac.ir
*Corresponding author

Received: 16 April 2024, Revised: 24 September 2024, Accepted: 2 November 2024

Abstract: Writing on steel coils and slabs (to mark them) is one of the problems faced by domestic steelmaking industries. Currently, this operation is done with the help of human power, which has its own drawbacks. In order to solve these problems, a marker robot is supposed to be applied. This robot writes letters, numbers, and signs on steel coils with an automatic paint spray gun. The robot intended for this purpose is a 5 degrees of freedom robot (5DOF), 3 degrees of freedom are related to the robot arm, and the other 2 degrees are related to the robot wrist. Due to the special conditions governing the problem, the solution of inverse kinematics has been done by the geometric method, which is simpler than the algebraic method. In order to determine the path of the robot (the path of letters and numbers), a series of time-dependent Equations have been applied. To show the accuracy of the planned trajectory, simulations have been carried out on the mentioned robot and the movement trajectory of the end-effector and the configuration of the arm have been graphically displayed. The programming of the robot's trajectory has been performed in MATLAB and LabVIEW and Visual Nastran has been applied to simulate the robot's trajectory.

Keywords: Innovative Solution, Inverse Kinematics, Marker Robot, Steel Coils and Slabs, Trajectory Planning

Biographical notes: Mohammad Sajjad Mahdieh received his PhD in Mechanical Engineering from the University of Tehran, Iran in 2016. He is currently an Assistant Professor at the Department of Mechanical Engineering, Shahid Chamran University of Ahvaz, Iran. His research areas are inverse engineering, 3D printing, and metal forming.

Research paper

1 INTRODUCTION

In today's world industry, the use of robots in different parts of the production line is increasing [1-4]. For example, applying different kinds of robots is a privilege in steel factories [5-6]. An example of these robots is the writer (or marker) robot, which draws letters, numbers, and symbols on steel coils and slabs using a mobile automatic paint spray (pistol) [7-8]. Carrying out such proportional movements requires the proper design of the path of the robot's end-effector. In 1991, "Su" and his colleagues presented an effective and optimal method for designing the trajectory of paint-spraying robots, which was used in the future. Designing a suitable trajectory for paint spraying robots was a vital thing in the industry at that time because it prevented the wastage of a significant amount of paint, resulting in a significant saving in time and cost [9]. In addition, the final stage of the design of the robot requires several analytical and numerical methods such as finite element methods [10-14]. In 1994, Antonio conducted research on the design of the movement trajectory of a robot that covered different parts by spraying and obtained results. The research conducted by Antonio was the foundation of the next industrial projects [15]. In 1997, Asakawa developed a new method of designing the trajectory of car body paint spraying robots. His method, which was implemented under the title of Teachingless robots, was successful and saved time and money for the Hyundai company [16]. In 1996, Hertling conducted research on the design of complex and curved paths of the paint-spraying robot. Of course, Hertling's work remained a research project, but his research was very valuable for subsequent research [17]. To truly manufacture the marker robot, several precise manufacturing and production methods such as forming and machining should be applied [18-27]. Currently, in the steel industries of our country, writing on the steel coils and slabs is done by human power, which has its own problems. Therefore, according to the domestic industry's need for such robots, a research plan was defined, and the results related to the trajectory planning of the robot arm are presented in this article. According to the parameters and characteristics of the designed robot, it is necessary to first solve the direct and inverse kinematics of the problem in order to obtain the transformation matrix of the joints. Next, the trajectory planning of the robot to write letters is done, and position-time Equations of the path of writing letters are extracted. After obtaining the Equations of the path, the angles of each joint during the operation of writing letters are obtained with the help of programming in MATLAB and LabVIEW. In the end, the result of the simulation was done by Visual Nastran software.

2 RESEARCH METHOD

2.1. Solving Inverse Kinematics for Writing on Slabs

In order to determine the transformation matrix of the joints, the parameters of the Denavit-Hartenberg robot according to “Fig. 1” are given in “Table 1” [28].

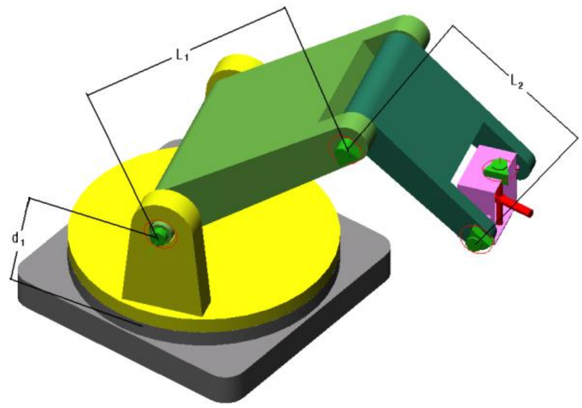

Fig. 1 Schematic view of the robot and its parameters.

Table 1 Denavit-Hartenberg parameters of the robot

i	α_{i-1}	a_{i-1}	d_i	θ_i
1	0	0	d_1	θ_1
2	-90	0	0	θ_2
3	0	L_1	0	θ_3
4	0	L_2	0	θ_4
5	90	0	0	θ_5

The frameworks considered to solve the problem according to “Fig. 2” are the basic framework (0), the final end-effector framework (EE), and the panel framework (S). The frame of the painting is mounted on a stationary slab.

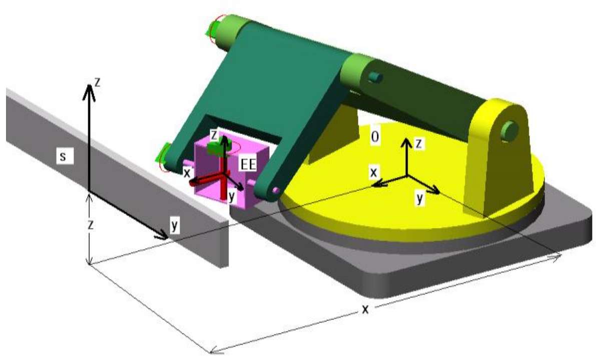

Fig. 2 Display of the basic frameworks, the EF, and the slab.

Thus, the relationship between the transformation matrices of the frames is according to Equation (1):

$$^{0}T_{E} = {}^{0}T_{S}\,{}^{S}T_{E} \tag{1}$$

The transformation matrix of the end-effector relative to the base of the robot is equal to $^{0}T_{E}$. The matrix $^{0}T_{5}$ is obtained by multiplying the transformation matrices 1 to 5 (according to Equation (2)).

$$^{0}T_{5} = {}^{0}T_{1}\;{}^{1}T_{2}\;{}^{2}T_{3}\;{}^{3}T_{4}\;{}^{4}T_{5} \tag{2}$$

Finally, the matrix $^{0}T_{E}$ can also be expressed according to Equation (3):

$$^{0}T_{E} = \begin{bmatrix} 1 & 0 & 0 & px \\ 0 & 1 & 0 & py \\ 0 & 0 & 1 & pz \\ 0 & 0 & 0 & 1 \end{bmatrix} \tag{3}$$

The pistol should be perpendicular to the table while writing, however, the part related to the transformation matrix $^{0}T_{E}$ is equal to the identity matrix [29].

px, py, pz are the final positions of the robot's end-effector from the base, which is explained in the trajectory planning section 2-3. As stated, due to the special conditions governing the problem, the geometric method has been used to obtain the inverse kinematics of the robot. The special condition of the problem is the verticality of the robot's end-effector on the table, which must be maintained at all times.

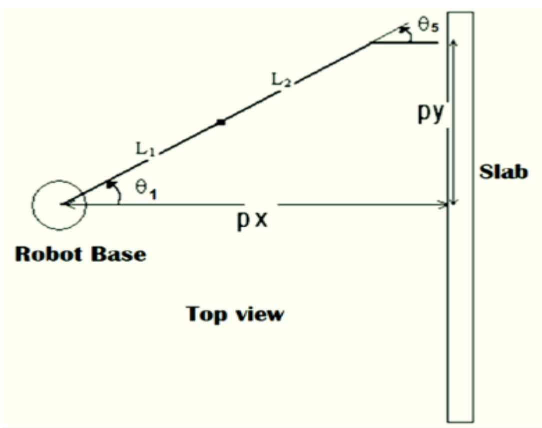

Fig. 3 Robot top view for expressing θ_1 and θ_5.

According to the explanations provided, the method of obtaining the angles from θ_1 to θ_5 has been examined in the following. As it is clear from "Fig. 3", θ_1 and θ_5 are obtained from Equations (4 and 5):

$$\theta_1 = \tan^{-1}(py/px) \tag{4}$$

$$\theta_5 = -\tan^{-1}(py/px) = -\theta_1 \tag{5}$$

It should be noted that since the conventional rotation directions of θ_1 and θ_5 are opposite to each other, so their signs are also opposite.

According to "Fig. 4", θ_3 is obtained from Equation (6):

$$w^2 = pz^2 + (px/\cos\theta_1)^2$$
$$w^2 = L_1^{\,2} + L_2^{\,2} + 2L_1L_2\cos(\pi - \theta_3)$$
$$\Rightarrow \theta_3 = \cos^{-1}\left(\frac{pz^2 + (px/\cos\theta_1)^2 - L_1^{\,2} - L_2^{\,2}}{2L_1L_2}\right) \tag{6}$$

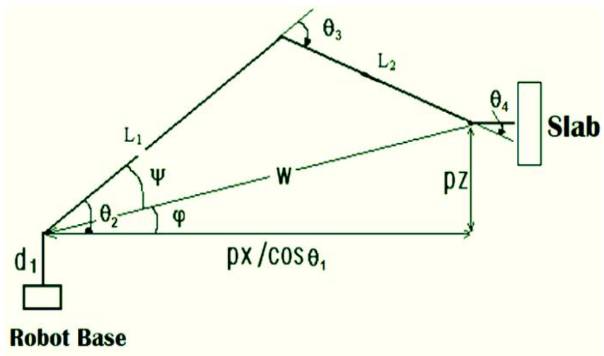

Fig. 4 View of the robot to express θ_2, θ_3 and θ_4.

Also, θ_2 is obtained as Equation (7) after the following calculations:

$$\theta_2 = -\psi - \varphi$$
$$\varphi = \tan^{-1}\left(\frac{pz}{px/\cos\theta_1}\right)$$
$$\frac{L_2}{\sin\psi} = \frac{L_1}{\sin\alpha} = \frac{w}{\sin(\pi - \theta_3)}$$
$$\psi = \sin^{-1}\left(\frac{L_2\sin(\pi - \theta_3)}{\sqrt{pz^2 + (px/\cos\theta_1)^2}}\right)$$
$$\Rightarrow \theta_2 = -\sin^{-1}\left(\frac{L_2\sin(\pi - \theta_3)}{\sqrt{pz^2 + (px/\cos\theta_1)^2}}\right) - \tan^{-1}\left(\frac{pz}{px/\cos\theta_1}\right) \tag{7}$$

And according to "Fig. 4", θ_4 is obtained according to Equation (8):

$$\theta_4 = -\theta_2 - \theta_3 \tag{8}$$

2.2. Solving Inverse Kinematics for Writing on Coils

The parameters of Denavit Hartenberg are similar to "Table 1". In this way, it is possible to obtain the transformation matrix of the joints in relation to each other. For example, below (Equation (9)) is the transformation matrix of the third joint compared to the second:

$$ {}^{2}T_3 = \begin{bmatrix} \cos(\theta_3) & -\sin(\theta_3) & 0 & L_1 \\ \sin(\theta_3) & \cos(\theta_3) & 0 & 0 \\ 0 & 0 & 1 & 0 \\ 0 & 0 & 0 & 1 \end{bmatrix} \quad (9) $$

The frameworks considered to solve the problem according to "Fig. 5" are the basic framework (0), the end-effector framework (EE), and the panel framework (S). The panel frame is mounted on the coil.

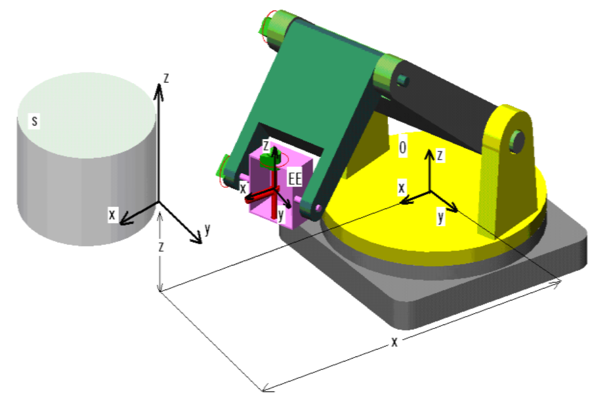

Fig. 5 Display of the basic frameworks, the end-effector, and the panel (coil).

The paint pistol should be perpendicular to the coil when writing. Therefore, due to the special status of the project, the geometric method has been used to obtain the inverse kinematics of the robot. The special condition of the problem is the verticality of the robot's end-effector on the coil, which must be maintained at every moment. With the explanations provided, the angles θ_1 to θ_5 can be obtained in the following order. As it is clear from "Fig. 6", θ_1 is obtained from Equations (10 and 11):

$$ \begin{aligned} &\theta_1 = \tan^{-1}(k / px) \\ &k = R \sin\alpha \\ &px = X + x(t) \end{aligned} \quad (10) $$

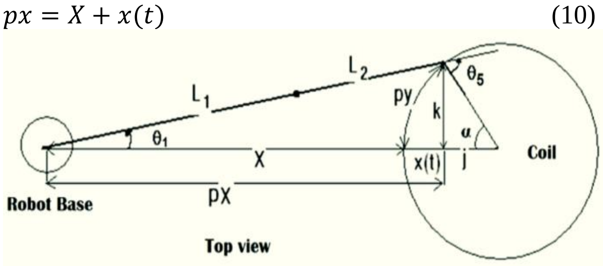

Fig. 6 The top view of the robot to express θ_1 and θ_5.

Where, R is the radius of the coil and X is the longitudinal distance of the coil from the base of the robot ("Fig. 6").

$$ \begin{aligned} &\theta_1 = \tan^{-1}(R \sin\alpha / px) \\ &\alpha = py / R \end{aligned} \quad (11) $$

α is expressed in radians:

$$ \Rightarrow \theta_1 = \tan^{-1}\left(\frac{R \sin(py/R)}{px} \right) \quad (12) $$

According to "Fig. 6", θ_5 is obtained from Equations (13):

$$ \begin{aligned} &\theta_5 = -\theta_1 - \alpha \\ &\alpha = py / R \\ &\Rightarrow \theta_5 = -\left[R - R\cos(py/R) + py/R \right] \end{aligned} \quad (13) $$

θ_2, θ_3, and θ_4 are the same as writing on the slabs:

$$ \theta_3 = \cos^{-1}\left(\frac{pz^2 + (px/\cos\theta_1)^2 - L_1{}^2 - L_2{}^2}{2L_1L_2} \right) \quad (14) $$

$$ \theta_2 = -\sin^{-1}\left(\frac{L_2 \sin(\pi - \theta_3)}{\sqrt{pz^2 + (px/\cos\theta_1)^2}} \right) - \tan^{-1}\left(\frac{pz}{px/\cos\theta_1} \right) \quad (15) $$

$$ \theta_4 = -\theta_2 - \theta_3 \quad (16) $$

2.3. Trajectory Planning

A reference point (0,0) is determined for each letter, and the movement starts from this point and ends at this point. As mentioned, due to the use of an automatic paint spray gun (automatic change of disconnecting and connecting action), there is no need for the final operator to move away from the keyboard anymore, and the letters are written continuously, therefore, its complete path should be considered for each letter. Thus, it starts from the reference point and includes all the components of the letters as well as the interface between the components. Finally, it returns to the reference point. For example, according to "Fig. 7", to write the letter E, eight lines should be used, four of which are main (2, 3, 5, 7) and four are auxiliary (1, 4, 6, and 8). The paint spray gun is on when crossing the main lines (solid lines) and off when crossing the auxiliary lines (pale lines). Also, the path of the letter C is also shown, in which segments 1 and 3 are auxiliary and arc 2 is main.

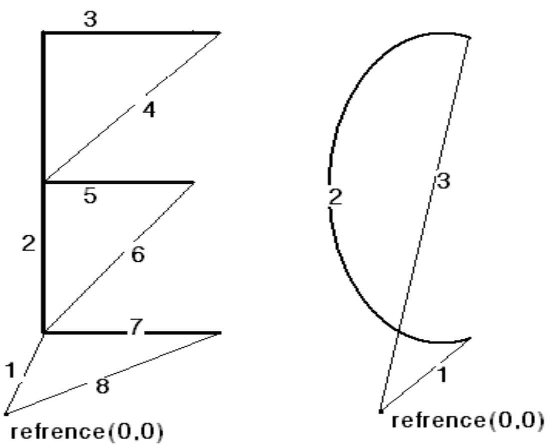

Fig. 7 The moving path of letters E and C.

The path of other letters is obtained similarly. Now the Equations of the lines and curves forming each letter or number should be written as locus Equations. For example, the Equations of the first three-line segments of the letter E are in the form of Equation (17):

$$\begin{aligned} z &= -0.2857y \\ z &= 20 \\ y &= -10 \end{aligned} \tag{17}$$

Also, polar coordinates should be used to write the Equations of circular or ellipse components of letters. For example, the Equation of the elliptical arc of the letter C is given in Equation (18):

$$\begin{cases} y = 50\sin\theta - 60 \\ z = 80\cos\theta + 100 \\ -0.54\pi \le \theta \le 0.54\pi \end{cases} \tag{18}$$

Now the Equations that are in terms of locus should be converted into locus-time Equations. This work is achieved according to the speed of the robot's performers and its acceleration time. For example, the Equation of the first line segment of the letter E in terms of time is according to Equation (19):

$$\begin{cases} y(t) = -48.0762t \\ z(t) = 13.735t \\ 0 \le t \le 1.456 \end{cases} \tag{19}$$

Also, the Equation of the elliptical arc of the letter C in terms of time is according to Equation (20):

$$\begin{cases} \theta = -0.4727t + 3.9611 \\ y(t) = 80\cos\theta + 100 \\ z(t) = 50\sin\theta - 60 \\ 1.46 \le t \le 8.46 \end{cases} \tag{20}$$

Thus, the values of px, py, and pz used in the transformation matrix are according to Equation (21):

$$\begin{cases} px = X \\ py = 300 + y(t) \\ pz = Z + z(t) \end{cases} \tag{21}$$

Where, X and Z are the longitudinal distance and height of the board/panel from the base of the robot. For example, in order to write on the slab, the transformation matrix ${}^{0}T_{E}$ for the first segment of the letter E is as Equation (22):

$${}^{0}T_{E} = \begin{bmatrix} 1 & 0 & 0 & X \\ 0 & 1 & 0 & 300 - 48.0862t \\ 0 & 0 & 1 & 13.735t + Z \\ 0 & 0 & 0 & 1 \end{bmatrix} \tag{22}$$

For writing on the coils, x(t) according to “Fig. 8” is obtained as Equation (23):

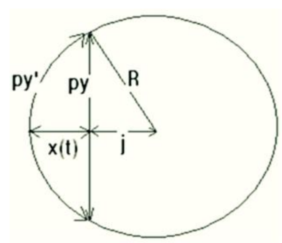

Fig. 8 The conversion of a flat panel to a circular panel (coil).

$$\begin{aligned} & x(t) = R - j \\ & j = R\cos\alpha \\ & x(t) = R - R\cos\alpha \\ & \alpha = py / R \\ & \Rightarrow x(t) = R - R\cos(py/R) \end{aligned} \tag{23}$$

For example, the ${}^{0}T_{E}$ conversion matrix for the first segment of the letter E is according to Equation (24):

$$
{}^{0}T_{E} = \begin{bmatrix} 1 & 0 & 0 & X + R - R\cos\left((300 - 28.086t)/R\right) \\ 0 & 1 & 0 & 300 - 48.0862t \\ 0 & 0 & 1 & 13.735t + Z \\ 0 & 0 & 0 & 1 \end{bmatrix} \tag{24}
$$

3 SIMULATION AND RESULTS

3.1. Simulations for Writing on Steel Slabs

The inverse kinematics programming of the robot is done in MATLAB software, whose inputs are six letters or numbers and robot parameters such as the length of the members and the distance from the base of the robot and the output of the robot angles program, which is obtained from the inverse kinematics solution. The angles obtained from the output of the program can be checked by the direct kinematic Equations of the robot, which are shown in “Fig. 9” of the related diagrams.

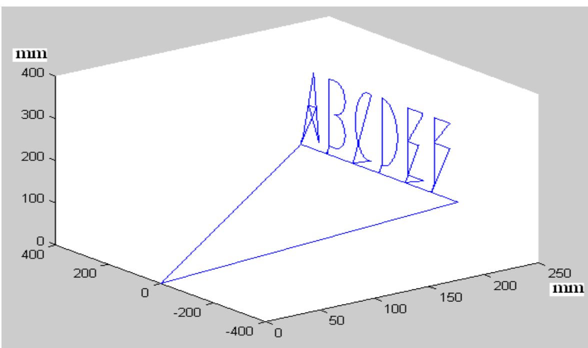

Fig. 9 Testing the program for writing on the slab.

Simulink and Visual Nastran software have been used to simulate the robot's movement path. Figure 10 shows the model designed in Simulink for kinematic simulation [30].

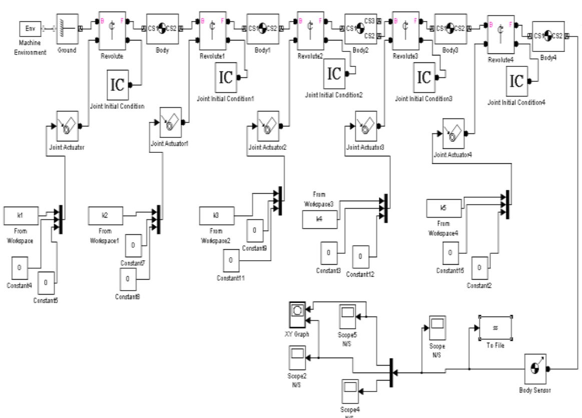

Fig. 10 Model designed in Simulink.

Also, in “Fig. 11”, two states of the machine (robot arm system) simulated for the designed model are shown. The simulated machine follows the trajectory of the given letters.

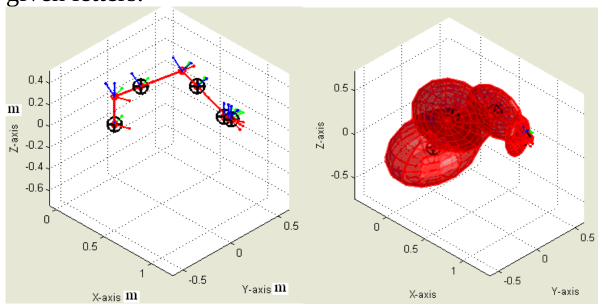

Fig. 11 Two states of the machine simulated for the designed model.

According to the simulation performed in Simulink, the final position is obtained in terms of two y-z axes, whose diagram is shown in “Fig. 12”.

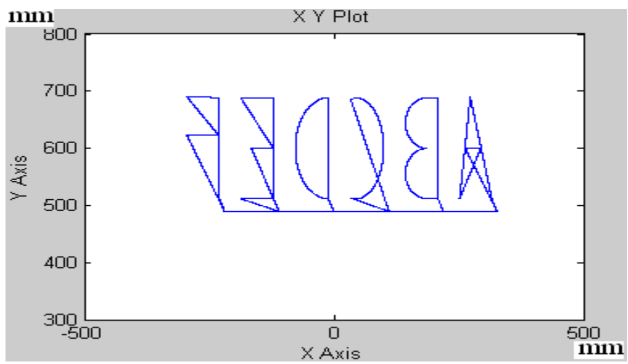

Fig. 12 Position of the end-effector.

In fact, “Fig. 12” shows the verification of the simulation results with Simulink because the end-effector has exactly followed the path of the desired letters. Nastran is a powerful simulation software that provides reliable results. Figure 13 shows four states of the robot in the simulation operation in Visual Nastran.

As it is clear from “Fig. 13”, the robot follows the path of the letters exactly, and this means the accuracy of the path design and solving the inverse kinematics problem. Also, according to “Fig. 13”, it is evident that the end-effector of the robot is perpendicular to the slab at any moment. As a result, the spray gun is perpendicular to the surface of the slab at any moment, and this causes the dispersion of the paint from the gun to be minimized and the best quality of the written text is achieved.

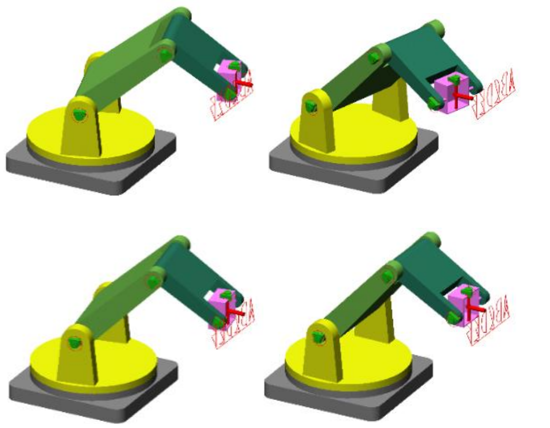

Fig. 13 Different states of the robot during the simulation operation.

3.2. Simulations for Writing on Steel Coils

The inverse kinematics programming of the robot is done in MATLAB software, whose inputs are six letters or numbers and robot parameters such as the length of the links, the distance of the coil from the base of the robot, the radius of the coil, and the output of the robot angles program, which is obtained from solving the inverse kinematics. The angles obtained from the output of the program can be tested by direct kinematic Equations of the robot, which are shown in “Fig. 14” of the program test diagram.

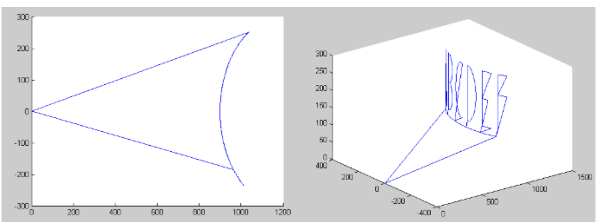

Fig. 14 Testing the program for writing on the coil.

As it is clear from “Fig. 14”, the path of the end-effector is located on the arc of the circle that corresponds to the circumference of the steel coil. Also, “Fig. 15” shows the Block Diagram view of the program written in LabVIEW software.

Similar to the program written in MATLAB, it takes 6 letters or numbers as input, and according to the parameters of the robot set in the Block Diagram, the angles of the robot obtained from the kinematics solution save the results obtained as output in the corresponding files. Figure 16 shows the Front panel view of the written program after its execution. As it is known, the proposed test diagram is completely consistent with the test diagram drawn in MATLAB.

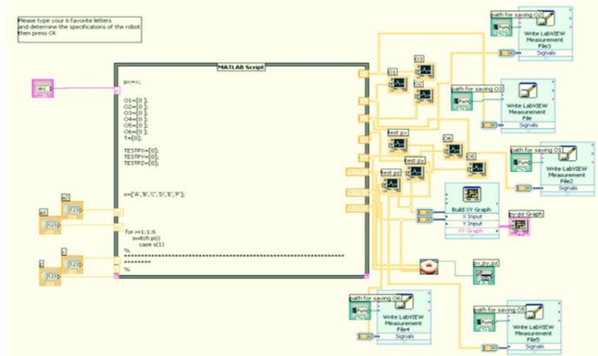

Fig. 15 The block diagram view of the program written in LabVIEW.

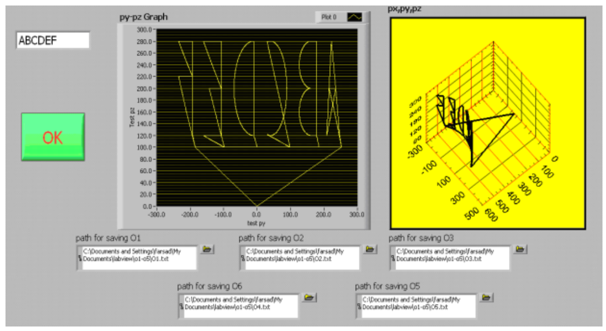

Fig. 16 Front panel view of the executed program.

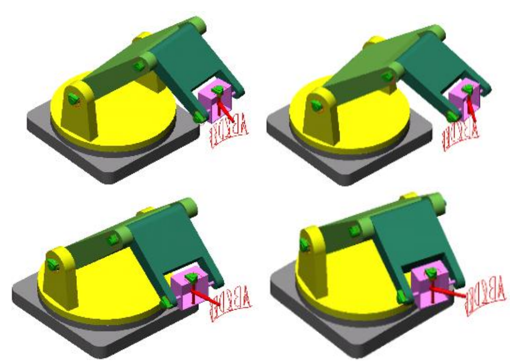

Fig. 17 Different states of the robot while writing on the coil.

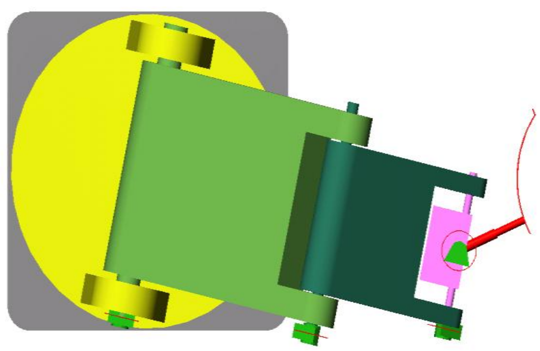

Fig. 18 The view from the top of the robot after the end of the simulation.

In addition, Visual Nastran software has been used to simulate the movement of the robot. Figure 17 shows the four states of the robot during the simulation operation, as well as the top view of the robot after the end of the simulation operation is shown in “Fig. 18” in the Visual Nastran software.
As it is clear from “Figs. 17 and 18”, the end-effector is perpendicular to the coil at any moment, and the path of writing the letters is circular and in line with the body of the coil, and this indicates the verification of solving the problem.

4 CONCLUSIONS

The goal of this article was to design the path of the robot designed for marking on the steel slabs and coils, which obtained the following results:
1- The first step to achieve this goal is the direct kinematics solution of the problem, which was done after determining the robot's Denavit-Hartenberg parameters and then the matrices Joint transformation was obtained.
2- Due to the special conditions governing the problem, the inverse kinematics of the robot was performed using the geometric method, which is much simpler and more reliable than the algebraic method.
3- Designing the path of the robot was done with the help of designing the path of the letters and the required angles of the joints were extracted during the operation.
4- Finally, the verification of solving the problem was ensured by carrying out simulation operations with strong and reliable software such as Nastran and LabVIEW.

ACKNOWLEDGMENTS

We are grateful to the Research Council of Shahid Chamran University of Ahvaz for financial support (SCU.EM1403.39184).

REFERENCES

[1] Goel, R., Gupta, P., Robotics and Industry 4.0, A Roadmap to Industry 4.0: Smart Production, Sharp Business and Sustainable Development, 2020, pp. 157-169.

[2] Day, C. P., Robotics in Industry—Their Role in Intelligent Manufacturing, Engineering, Vol. 4, No. 4, 2018, pp. 440-445.

[3] Bragança, S., et al., A Brief Overview of the Use of Collaborative Robots in Industry 4.0: Human Role and Safety, in Occupational and Environmental Safety and Health, P.M. Arezes, et al., Editors, Springer International Publishing: Cham., 2019, pp. 641-650.

[4] Tantawi, K. H., Sokolov, A., and Tantawi, O., Advances in Industrial Robotics: From Industry 3.0 Automation to Industry 4.0 Collaboration. in 2019 4th Technology Innovation Management and Engineering Science International Conference (TIMES-iCON), 2019.

[5] Javaid, M., et al., Substantial Capabilities of Robotics in Enhancing Industry 4.0 Implementation. Cognitive Robotics, Vol. 1, 2021, pp. 58-75.

[6] Kerber, E., et al. Towards Robotic Fabrication in Joining of Steel, In ISARC, Proceedings of the International Symposium on Automation and Robotics in Construction, IAARC Publications, 2018.

[7] Crisnapati, P. N., et al., Pasang Aksara Bot: A Balinese Script Writing Robot Using Finite State Automata Transliteration Method, In Journal of Physics: Conference Series, IOP Publishing, 2019.

[8] Meena, J., Kumar, T. S., and Amal, T., Design and Implementation of a Multi-Purpose End-Effector Tool for Industrial Robot, In 2021 International Symposium of Asian Control Association on Intelligent Robotics and Industrial Automation (IRIA), IEEE, 2021.

[9] Suh, S. H., et al., A Prototype Integrated Robotic Painting System: Software and Hardware Development, In Proceedings of 1993 IEEE/RSJ International Conference on Intelligent Robots and Systems (IROS'93), IEEE, 1993.

[10] Mahdieh, M. S., Esteki, M. R., Feasibility Investigation of Hydroforming of Dental Drill Body by FEM Simulation, Journal of Modern Processes in Manufacturing and Production, Vol. 11, No. 2, 2022, pp. 71-83.

[11] Mahdieh, M. S., Monjezi, A., Investigation of an Innovative Cleaning Method for the Vertical Oil Storage Tank by FEM Simulation, Iranian Journal of Materials Forming, 2022.

[12] Mahdieh, M. S., et al., A Study on Stamping of Airliner’s Tail Connector Part Through FEM Simulation, Journal of Simulation and Analysis of Novel Technologies in Mechanical Engineering, 2023.

[13] Mahdieh, M. S., Zadeh, H. M. B., and Reisabadi, A. Z., Improving Surface Roughness in Barrel Finishing Process Using Supervised Machine Learning, Journal of Simulation and Analysis of Novel Technologies in Mechanical Engineering, Vol. 15, No. 2, 2023, pp. 5-15.

[14] Sajjad Mahdieh, M., Nazari, F., and Khairullah, A. R., A Study on The Effects of Different Pad Materials on Brake System Performance of a High-Capacity Elevator by FEM Simulation. International Journal of Advanced Design and Manufacturing Technology, Vol. 65, 4, 2024, pp. 61.

[15] Antonio, J. K., Optimal Trajectory Planning for Spray Coating, In Proceedings of the 1994 IEEE International Conference on robotics and Automation, IEEE, 1994.

[16] Asakawa, N., Takeuchi, Y., Teachingless Spray-Painting of Sculptured Surfaces by An Industrial Robot, In

Proceedings of the International Conference on Robotics and Automation, IEEE, 1997.

[17] Hertling, P., et al., Task Curve Planning for Painting Robots, Process Modeling and Calibration, IEEE Transactions on Robotics and Automation, Vol. 12, No. 2, 1996, pp. 324-330.

[18] Mahdieh, M. S., The Surface Integrity of Ultra-Fine Grain Steel, Electrical Discharge Machined Using Iso-Pulse and Resistance–Capacitance-Type Generator, Proceedings of the Institution of Mechanical Engineers, Part L: Journal of Materials: Design and Applications, Vol. 234, No. 4, 2020, pp. 564-573.

[19] Mahdieh, M. S., Recast Layer and Heat-Affected Zone Structure of Ultra-Fined Grained Low-Carbon Steel Machined by Electrical Discharge Machining. Proceedings of the Institution of Mechanical Engineers, Part B: Journal of Engineering Manufacture, Vol. 234, No. 5, 2020, pp. 933-944.

[20] Mahdieh, M. S., Improving Surface Integrity of Electrical Discharge Machined Ultra-Fined Grain Al-2017 by Applying RC-Type Generator, Proceedings of the Institution of Mechanical Engineers, Part E: Journal of Process Mechanical Engineering, 2023, pp. 09544089231202329.

[21] Mahdieh, M. S., Mahdavinejad, R., Comparative Study on Electrical Discharge Machining of Ultrafine-Grain Al, Cu, and Steel, Metallurgical and Materials Transactions A, Vol. 47, No. 12, 2016, pp. 6237-6247.

[22] Mahdieh, M. S., Mahdavinejad, R., Recast Layer and Micro-Cracks in Electrical Discharge Machining of Ultra-Fine-Grained Aluminum, Proceedings of the Institution of Mechanical Engineers, Part B: Journal of Engineering Manufacture, Vol. 232, No. 3, 2018, pp. 428-437.

[23] Mahdieh, M. S., Mahdavinejad, R. A., A Study of Stored Energy in Ultra-Fined Grained Aluminum Machined by Electrical Discharge Machining. Proceedings of the Institution of Mechanical Engineers, Part C: Journal of Mechanical Engineering Science, Vol. 231, No. 23, 2017, pp. 4470-4478.

[24] Mahdieh, M. S., Zare-Reisabadi, S., Effects of Electro-Discharge Machining Process on Ultra-Fined Grain Copper, Proceedings of the Institution of Mechanical Engineers, Part C: Journal of Mechanical Engineering Science, Vol. 233, No. 15, 2019, pp. 5341-5349.

[25] Saraeian, P., et al., Influence of Vibratory Finishing Process by Incorporating Abrasive Ceramics and Glassy Materials on Surface Roughness of CK45 Steel. ADMT Journal, Vol. 9, No. 4, 2016, pp. 1-6.

[26] Vakili Sohrforozani, A., et al., A Study of Abrasive Media Effect on Deburring in Barrel Finishing Process, Journal of Modern Processes in Manufacturing and Production, Vol. 8, No. 3, 2019, pp. 27-39.

[27] Vakili Sohrforozani, A., et al., Effects of Abrasive Media on Surface Roughness in Barrel Finishing Process, ADMT Journal, Vol. 13, No. 3, 2020 pp. 75-82.

[28] Craig, J. J., Introduction to Robotics, Pearson Educacion, 2006.

[29] Lewis, F., Mechanical Engineering Handbook Ed. Frank Kreith Boca Raton: CRC Press LLC, 1999.

[30] Karris, S. T., Introduction to Simulink with Engineering Applications, Orchard Publications, 2006.

Int. J. Advanced Design and Manufacturing Technology, 2025, Vol. 18, No. 1, pp. 17-27

DOI: *ISSN: 2252-0406* *https://admt.isfahan.iau.ir*

Numerical Investigation of The Weld Length Effect and Sheet Thickness on Stress and Mechanical Characterization of The Diaphragm Bellows

Farshad Nazari *
Department of Mechanical Engineering,
Shahid Chamran University of Ahvaz, Iran
*Corresponding author
E-mail: F.nazari@scu.ac.ir

Anna Bahrami
Department of Mechanical Engineering,
Shahid Chamran University of Ahvaz, Iran
E-mail:

Received: 26 July 2024, Revised: 5 November 2024, Accepted: 11 December 2024

Abstract: Diaphragm bellows are one of the essential parts in sealings and rotary equipment which are affected by their design parameters. This paper investigated the effect of weld length and plate thickness, on the mechanical characterization of diaphragm bellows. The mechanical characterization includes stress distribution, bellows deflection, spring constant, and fatigue life of the welded metal bellows. Finite element analysis was employed to study the effect of weld length and sheet thickness on the diaphragm bellows. In this regard, 12 models were designed based on experimental parameters. The number and combination of tests were designed by the response surface method and the results were evaluated by ANOVA analysis. According to the results, if weld length and sheet thickness increase, the maximum stress and deflection of the bellows decrease, and the spring constant increases. The effect of sheet thickness on the behavior of the bellows is greater than weld length and it creates a limitation due to the effect on the spring constant. In the acceptable ranges of weld length and sheet thickness, based on fatigue analysis, the maximum life cycle is 1.2×10^6 and the minimum life cycle is 1.7×10^3.

Keywords: Diaphragm Bellows, Fatigue Life, Finite Element Method (FEM), Mechanical Characterization, Welded Bellows

Biographical notes: Farhad Nazari is an Assistant Professor of Mechanical Engineering at Shahid Chamran University of Ahvaz, Iran. He received his PhD in Mechanical Engineering–Manufacture and Production from the Kashan University in 2019. **Anna Bahrami** received her BSc in Mechanical Engineering from Shahid Chamran University of Ahvaz in 2023. Her current research interest includes simulation and research in solid mechanics.

Research paper

1 INTRODUCTION

Bellows are thin, flexible structures commonly used for sealing and in pressure piping systems because of vibrations during operations, assemblage deformations, and thermal effects [1-2]. Duffy et al. [3] used bellows in place of a piston in a motor to eliminate leakage and improve the efficiency of aircraft propulsion. Based on bellows configuration, there are two types of them: diaphragm or welded bellows and accordion-like or toroidal bellows. The mechanical behavior of the bellows is significantly affected by their geometry and shape. In practical applications, V-shape, U-shape, and S-shape bellows are common forms of accordion-like bellows [4].

Diaphragm or welded bellows are manufactured by alternately welding thin metallic circular disks at the inner and outer edges. Welding two disks creates one convolution and by welding numerous convolutions, a diaphragm bellows is manufactured [5]. This type of bellows has wide usage in mechanical seals of compressors, hydraulic accumulators and actuators. Most researchers focused on the mechanical characteristics of bellows with different designs and geometries. Tarabrin [6] studied the spatial bellows and formulated theoretical calculations regarding the bellows' stress-strain state while subjected to a longitudinal-axial compressive force.

Yuan et al. [7] investigated the behavior of reinforced S-shaped bellows under different conditions and found that stress is largely concentrated in the wave trough and also that, stress decreases as the number of convolutions increases. Gheni et al. [8] analyzed the stiffness and the flexibility of welded metal bellows numerically by changing the number of convolutions and found that stress has an inversely proportional relation with the number of convolutions but, after a certain number of increases in the number of convolutions, their data showed that the number of convolutions does not have much effect on the maximum stress.

Also, they presented that as the number of convolutions increases, the overall static stiffness shows a sharp decrease at first but the rate slows down. Xiang et al. [9] investigated load capacity and deformation and energy dissipation of different bellows joints and they discovered that the multi-convolution bellows joint had a load capacity comparable to the single-convolution joint. They also observed that the energy absorption increased proportionally with the number of convolutions. Li et al. [10] analyzed single-layer and double-layer S-shaped welded bellows subjected to axial force. They found that strain increases with compression load and that double-layer bellows are more resistant to elastic deformation.

Piao et al. [11] predicted the spring constant of welded bellows using numerical analysis results and bellows geometry and validated it with experimental data. Gheni et al. [4] in another study, analyzed the flexibility of the welded bellows after a shape optimization method was used. Cho et al. [12-13] created a program to determine the structural design of a welded metal bellows by changing the desired variables using commercial CAD software and ANSYS Workbench.

Nuer et al. [14] carried out a finite element analysis on a diaphragm bellows and a V-shape bellows and the results showed that the maximum stress in the diaphragm bellows is smaller than the maximum stress in the V-shape bellows.

There has been research conducted on the thickness of metal bellows. Prasanna Naveen Kumar et al. [15] analyzed the design parameters of metal bellows and showed that the wall thickness of the U-shaped bellows has a significant impact on the static mechanical behavior of the bellows. Yan et al. [16] studied the U-shaped metal bellows and concluded that grain size and wall thickness of bellows are major factors in their failure. A few research on the hydroforming process of bellows has also accounted for the wall thickness of bellows [17-19].

Jiang et al. [20] studied the welding process of bellows, forming, and the microstructure of the weld zone. They found one optimal welding condition based on microstructure analysis. Also, seam welding resulted in greater hardness than fusion welding. Guo et al. [21] examined welded bellows when subjected to tensile stress and determined that fatigue fracture began close to the weld. Krovvidi et al. [22] investigated the failure of welded bellows and determined that failure occurs at the inner weld of the bellows.

There have been many studies on accordion-like bellows over the years while lower research has focused on the diaphragm bellows. According to the literature review, the effect of weld placement and sheet thickness of the diaphragm bellows on mechanical characteristics and bellows behavior were not considered. In this research, the effect of weld length and sheet thickness on maximum stress, bellows deflection, spring constant, and fatigue life of the welded bellows have been investigated using the Finite element method, and the results were evaluated by variance analysis.

2 MATERIALS AND METHODS

The material of the diaphragm bellows was AISI 304 austenitic stainless steel. This is the common material used in metal bellows. Austenitic stainless steel is used in corrosive and high-temperature environments. It exhibits good mechanical properties in handling axial, lateral, and angular motions [15]. The mechanical properties of AISI 304 are presented in "Table 1".

Table 1 The mechanical properties of AISI 304 [23]

Young's modulus	Poisson's ratio	Fatigue strength	Yield strength	Tensile strength
203 GPa	0.275	490 MPa	690 MPa	1030 MPa

To investigate the effect of weld length and sheet thickness on maximum stress, bellows deflection, spring constant, and fatigue life of the welded bellows, finite element (FE) and analytical methods were utilized. Numerical simulation was based on a practical bellows which consists of 10 convolutions, inner diameter 39 mm and outer diameter 49 mm, weld length 1 mm, and sheet thickness 0.15 mm. A sectional view of the diaphragm bellows and the plate geometry of the bellows is shown in "Fig. 1". To examine the influence of weld length and sheet thickness on the performance of welded metal bellows, an axisymmetric model was developed in Abaqus commercial package. The inner diameter of the bellows does not change with varying parameters, and the outer diameter only varies by changes in the weld length of the bellows. In this model, the element type CAX4R was used to simulate the bellows behavior, and a 0.018 mm mesh size was selected for all models based on a mesh sensitivity analysis [24-25]. The results of the mesh sensitivity analysis revealed that the mesh size selected optimized the processing time and also provided high-accuracy outputs. Figure 2 shows the mesh configuration and boundary condition of the finite element model.

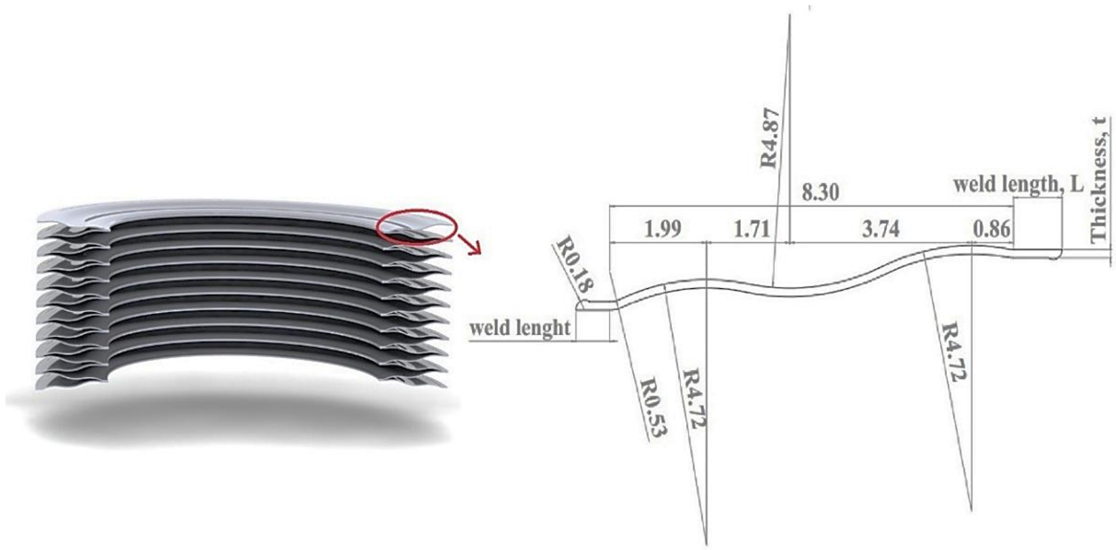

Fig. 1 Sectional view of the diaphragm bellows and the geometry of plates of the practical bellows (All dimensions in mm).

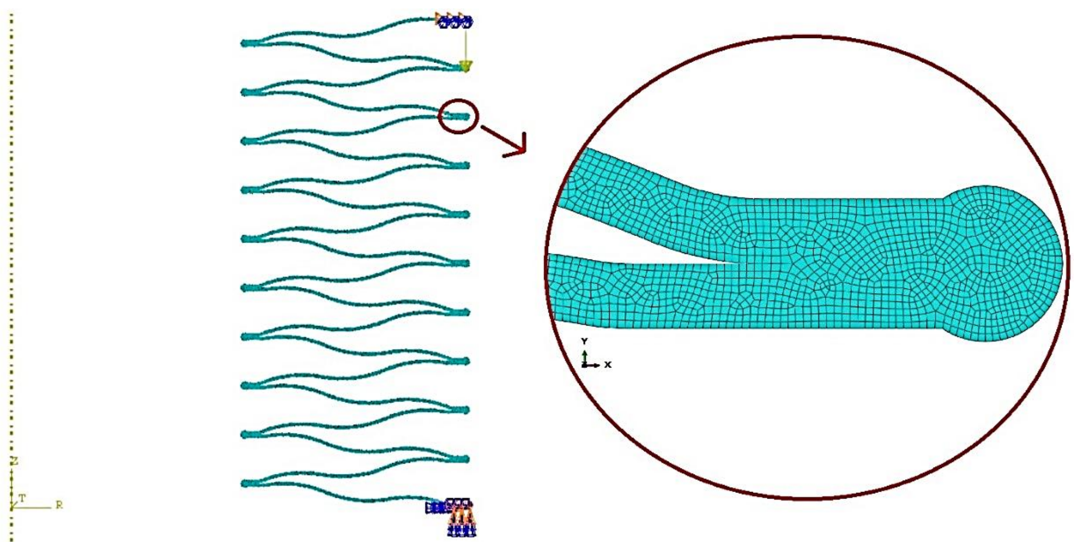

Fig. 2 Mesh configuration and boundary condition of the FE-model.

To determine the allowable range of the weld length of a diaphragm bellows, eight models with weld lengths of 0.5, 1, 1.5, 2, 2.5, 3, 3.5, and 4 mm were analyzed. Based on the practical weld length, eight different models with sheet thicknesses of 0.1, 0.15, 0.2, 0.25, 0.3, 0.35, 0.4, and 0.45 mm were simulated to determine the allowable range of sheet thickness. All models consisted of 10 convolutions and were compressed by a load of 10 kg. The quadric central composite response surface method was utilized to investigate the interaction between the effect of the parameters and the results were examined using ANOVA analysis. The analysis was computed using Design-Expert commercial software and, the set of experiments is presented in "Table 2".

Table 2 Sequence of experiment

Run	Weld length mm	Sheet thickness mm	Maximum stress MPa	Deflection mm	Sprint constant kN/m
1	3	0.35	133.6	0.892	109.933
2	3	0.15	421.8	6.165	15.9059
3	1	0.35	158.5	0.8416	116.516
4	2	0.15	442	6.269	15.642
5	1	0.25	233.3	1.958	50.0817
6	1	0.15	483.4	6.519	15.0422
7	2	0.35	145.3	0.8597	114.063
8	3	0.25	213	1.982	49.4753
9	2	0.25	172.9	1.955	50.1586

To examine the fatigue life of the bellows, modified Goodman criteria [26] were utilized to predict the life cycle by developing an analytical model as a code in MATLAB software. Equation (1) presents the modified Goodman criteria for calculating reversible stress in fatigue phenomena, as follows.

$$\sigma_{rev} = \frac{\sigma_a}{1 - \frac{\sigma_m}{S_{ut}}} \tag{1}$$

In these relations σ_{rev} is completely reversible stress, σ_a is the amplitude of the stress, σ_m is the mean stress, and S_{ut} represents tensile strength.

$$N = \left(\frac{\sigma_{rev}}{a}\right)^{\frac{1}{b}}$$

$$a = \frac{(f S_{ut})^2}{S_e} \tag{2}$$

$$b = \frac{-\log\left(\frac{f S_{ut}}{S_e}\right)}{3}$$

Equations (2) are used to evaluate the number of cycles that a mechanical component can undergo before failure. Where N is the number of cycles to failure, and Se is the endurance limit. a and b are constants defined respectively at 10^3 and 10^6 cycles for fully reversible stress on the S-N curve, and f is a fatigue strength fracture which is equal to 0.788 for this material [26]. Also, the spring constant was calculated using relation (3), in which k, F, and δ denote spring constant, applied force, and bellows deflection, respectively.

$$k = \frac{F}{\delta} \tag{3}$$

3 RESULTS AND DISCUSSION

Simulation of the practical bellows and the evaluation of their results indicated that the results have good agreement with the practical data and as both bellows and springs have low energy dissipation, the reaction force was used to validate the results. The external load applied to the bellows was 98.9 N (10 kg) and the reaction force of the simulation was 98.82 N which shows the results, with a 0.77% error, are acceptable. Investigating the stress contribution shows that maximum stress is concentrated where two plates are joined to make a convolution, and the critical point is located on the welded joints.

When the bellows is under compressive load, investigating the contribution of σ_y shows the rest of the bellows are under compressive stress, and an equilibrium of compression-tension is concentrated in the weld zone. Figure 3 illustrates the distribution of stress in the practical bellows (Run number 6 in "Table 2").

Investigating the effect of sheet thickness and weld length on maximum stress and bellows deflection showed that increasing the sheet thickness from 0.1 to 0.45 led to an 84% reduction in stress and a 97% reduction in deflection. Inversely, increasing the weld length from 0.5 to 4 resulted in a nearly 20% decrease in stress and an 8% decrease in deflection.

Also, increasing thickness and weld length in their respective range causes an increase in spring constant by approximately 94% and 4%, respectively. Figures 4 and 5 indicate the effect of weld length and sheet thickness on stress, deflection, and spring constant of bellows.

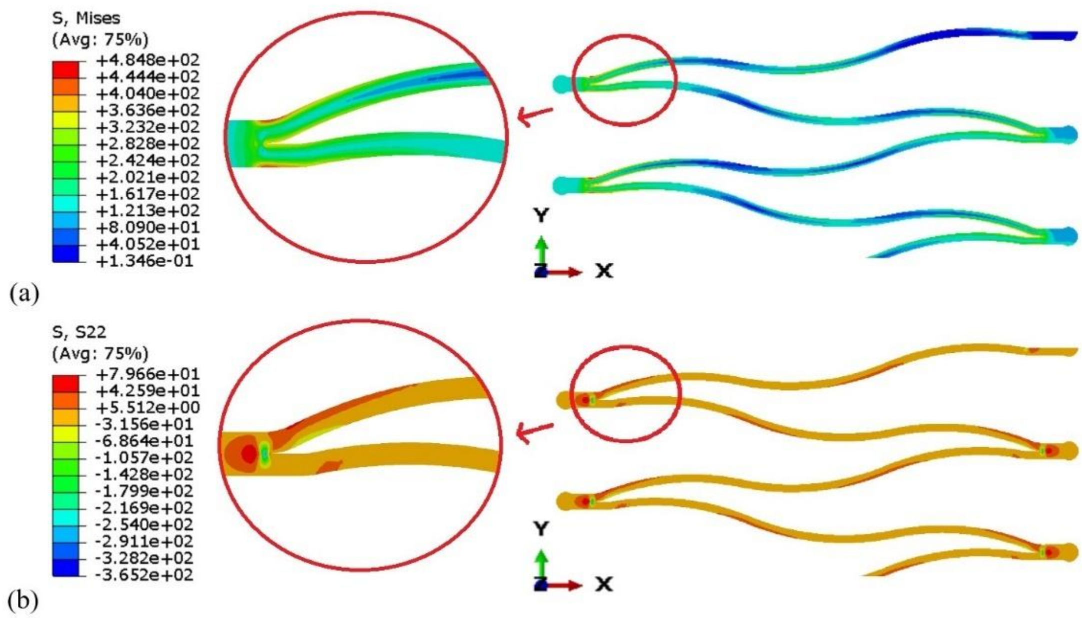

Fig. 3 Stress distribution in the bellows with 0.15 mm sheet thickness and 1 mm weld length: (a): effective stress, and (b): stress distribution in the vertical direction (σy).

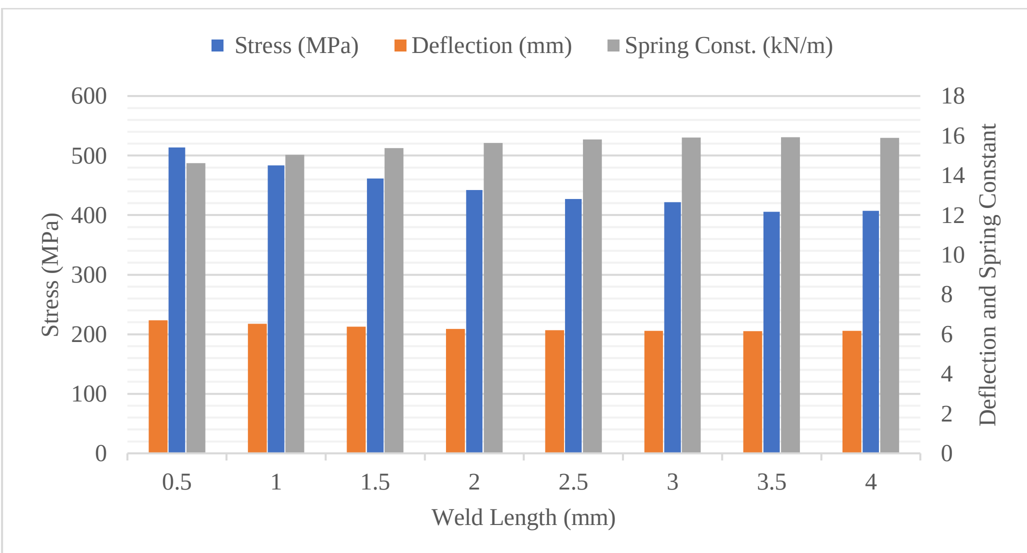

Fig. 4 Effect of weld length on the behavior of bellows.

In “Fig. 4”, studying the allowable range of the weld length shows that if the weld length is less than 1 mm, the maximum stress is over the fatigue strength which is not desirable for the bellows life that is because of stress concentration. Also, the weld lengths that are more than 3 mm do not affect the maximum stress significantly. So, the acceptable range of weld length is between 1 to 3 mm.

According to “Fig. 5”, if the sheet thickness is less than 0.15 mm, the maximum stress is over the yield strength and the plastic deformation occurs in the bellows. Also, if the sheet thickness is more than 0.35 mm, the change in maximum stress is not significant while deflection becomes limited and the spring constant extremely increases. Therefore, the acceptable range of sheet thickness is between 0.15 to 0.35 mm.

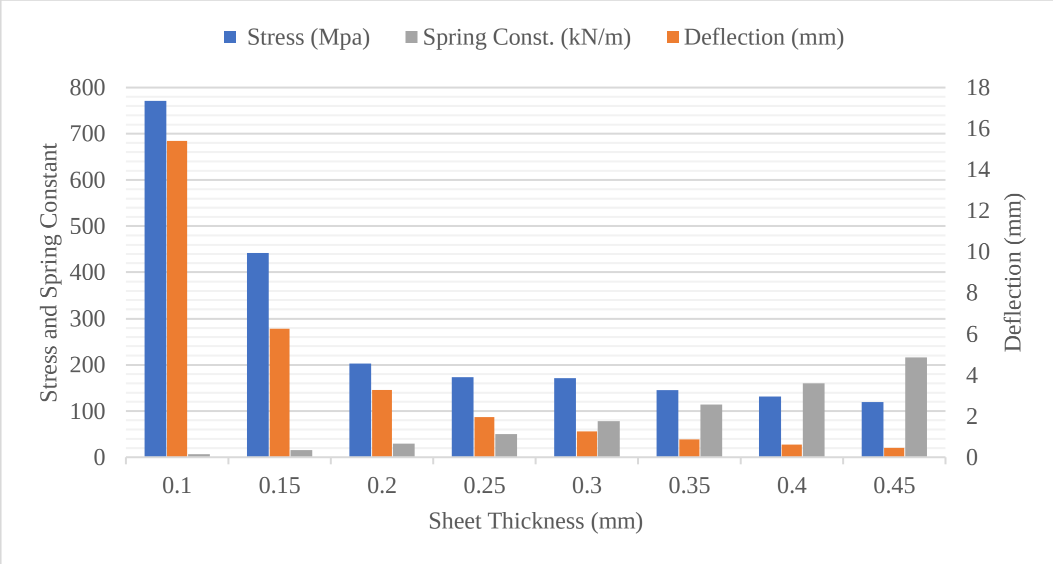

Fig. 5 Effect of sheet thickness on the behavior of bellows.

Investigating the results of analysis on weld length and sheet thickness showed, under a constant working force (10 Kg), with increasing weld length, the stress and deflection of the bellows decrease, and subsequently spring constant increases. Also, by Increasing sheet thickness, spring constant rises, and stress and deflection both fall. Therefore, an increase in sheet thickness has a greater effect on bellows behavior than an increase in weld length. But as the sheet thickness of the bellows becomes thicker, its spring effect becomes less effective and, diminishes bellows proficiency.

According to the determined range of sheet thicknesses and weld lengths, a set of experiments was designed using the response surface method and, the effects of both parameters on the mechanical behavior of the bellows were investigated. The designed experiments are presented in "Table 2". Figure 6 shows the stress distribution on the two groups of bellows with 0.15 mm constant sheet thickness and different weld lengths, and 1 mm constant weld length and various sheet thicknesses (Runs 2-6 in "Table 2").

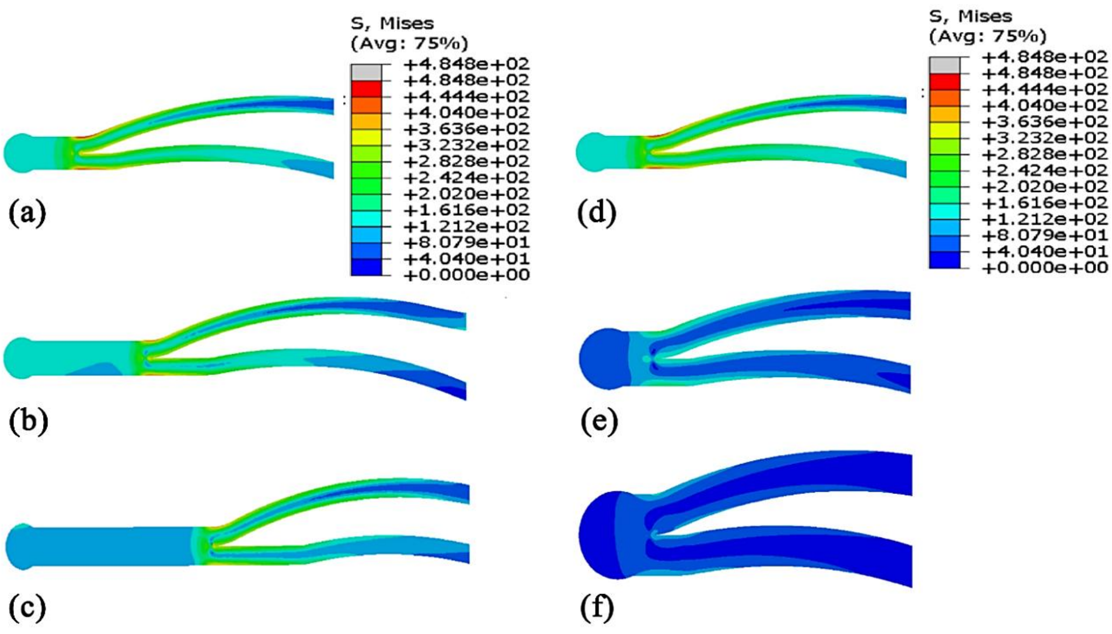

Fig. 6 The distribution of stress on bellows with 0.15 mm sheet thickness: (a): 1 mm, (b): 2 mm, (c): 3 mm weld lengths, and 1 mm weld length, (d): 0.15 mm, (e): 0.25 mm, and (f): 0.35 mm sheet thickness.

3.1. Effect of Weld Length and Sheet Thickness on Maximum Stress

Evaluation of the response surface results showed that there is a quadratic relation between weld length and sheet thickness with maximum stress of the bellows. The predictive model based on weld length (A) and sheet thickness (B) is presented in Equation 4. Based on the results, this model has a P-value of 0.0019 which shows the model is significant.

$$Stress\ (MPa) = +192.71 - 17.80 \times A - 151.63 \times B + 9.18 \times A \times B + 20.53\,A^2 + 91.03\,B^2 \quad (4)$$

The determination coefficient R^2 for this model is 0.9931 which indicates that the predicted values have a reasonable agreement with the numerical data. The linear pattern of the normal residuals plot and the plot of predicted-actual values show that there are no abnormalities in the data. Figure 7 illustrates the normal residuals plot and "Table 3" represents the result of ANOVA analysis

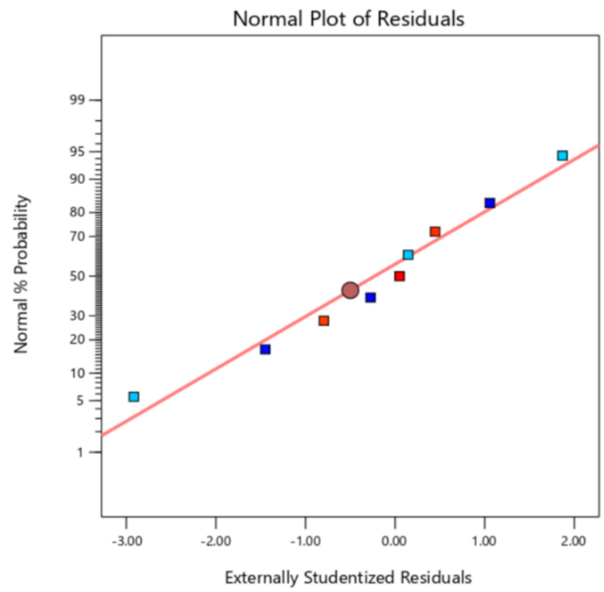

Fig. 7 Normal plot of residuals for maximum stress.

Table 3 ANOVA results of the model of maximum stress

Source	Sum of Squares	df	Mean Square	F-value	p-value	
Model	157611.1	5	31522.23	86.6798	0.0019	significant
A-Weld length	1901.04	1	1901.04	5.2274	0.1063	
B-Sheet thickness	137956	1	137956	379.3514	0.0002	
AB	336.7225	1	336.7225	0.9259	0.4069	
A^2	843.2356	1	843.2356	2.3187	0.2251	
B^2	16574.14	1	16574.14	45.5755	0.0066	

With a comparison of P-values of weld length and sheet thickness, it is realized that the effect of sheet thickness on maximum stress is much greater than weld length. Also, their interactive effect on maximum stress according to their P-value is not significant. Increasing sheet thickness causes a steep decrease in maximum stress, and after sheet thickness reaches 3 mm, the decreasing rate slows down to near zero.

The slope of change in maximum stress under the effect of weld length is nearly constant compared to sheet thickness. Maximum stress occurs when sheet thickness and weld length are minimum and with increasing sheet thickness, the maximum stress decreases. Figure 8 shows the interaction contour of the weld length and sheet thickness on maximum stress.

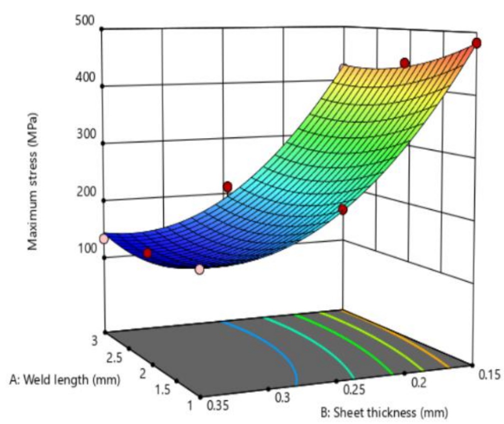

Fig. 8 The interaction contour of weld length and sheet thickness on maximum stress of bellows.

3.2. Effect of Weld Length and Sheet Thickness on Deflection

To predict the effect of the weld length and the sheet thickness on deflection, the following quadratic model is presented in Equation (5). The results show that the P-value of the model is 0.0001, which is lower than 0.05 and therefore it is a significant model. The determination coefficient R^2 for this model is 0.9998 which indicates that the predicted values have good agreement with the numerical data and linearity of the plots of normal residuals shows that there are no abnormalities in the data. Figure 9 illustrates the normal residuals plot and "Table 4" represents the results of ANOVA analysis.

$$Stress\ (MPa) = +1.94 - 0.0466 \times A - 2.73 \times B + 0.1011 \times A \times B + 0.0317\ A^2 + 1.63\ B^2 \quad (5)$$

Table 4 ANOVA results of the model of deflection

Source	Sum of Squares	df	Mean Square	F-value	p-value	
Model	49.950	5	9.990	2491.640	1.27E-05	significant
A-Weld length	0.013	1	0.013	3.249	0.169	
B-Sheet thickness	44.606	1	44.606	11125.352	1.88E-06	
AB	0.040	1	0.040	10.197	0.049	
A^2	0.002	1	0.002	0.501	0.529	
B^2	5.288	1	5.288	1318.900	4.59E-05	

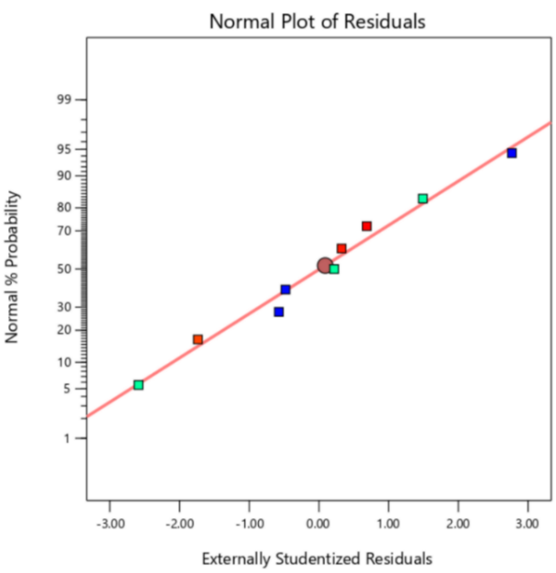

Fig. 9 The plot of residuals for deflection.

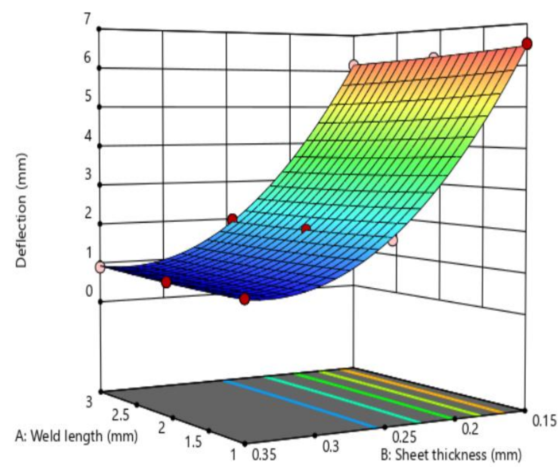

Fig. 10 The interaction contour of weld length and sheet thickness on bellows deflection.

According to the presented P-values of the weld length and the sheet thickness in "Table 3", the effect of sheet thickness on deflection is much greater than weld length and their interactive effect on bellows deflection is significant. As sheet thickness increases to 3 mm, there is a steep decrease in the deflection, and for more than 3 mm thickness the change rate slows down to a near-constant one. The deflection is highest when the sheet thickness and weld length are at their minimum, and lowest when they are at their maximum. The interaction contour of the weld length and sheet thickness on the bellows deflection is illustrated in "Fig. 10".

3.3. Effect of Weld Length and Sheet Thickness on Spring Constant

Equation (6) is a quadratic model to predict the effect of weld length and sheet thickness on the spring constant. According to the results, this model has a P-value of 0.0001 which shows that it is significant.

$$Stress\ (MPa) = +50.21 - 1.05 \times A + 48.99 \times B - 1.86 \times A \times B - 0.4622\ A^2 + 14.61\ B^2 \quad (6)$$

The determination coefficient R^2 for this model is 0.9999 which indicates that the predicted values have adequate agreement with the numerical data. Evaluation of the normal residuals plot shows that there are no abnormalities in the data. The normal residuals plot is illustrated in “Fig. 11” and “Table 5” represents the ANOVA results.

Table 5 ANOVA results of the model of spring constant

Source	Sum of Squares	df	Mean Square	F-value	p-value	
Model	14846.31	5	2969.2619	4816.9378	4.72E-06	significant
A-Weld length	6.6699	1	6.6699	10.8204	0.0460	
B-Sheet thickness	14398.34	1	14398.3361	23357.9565	6.18E-07	
AB	13.8650	1	13.8650	22.4928	0.0177	
A^2	0.4272	1	0.4272	0.6931	0.4661	
B^2	427.0111	1	427.0110	692.7262	0.0001	

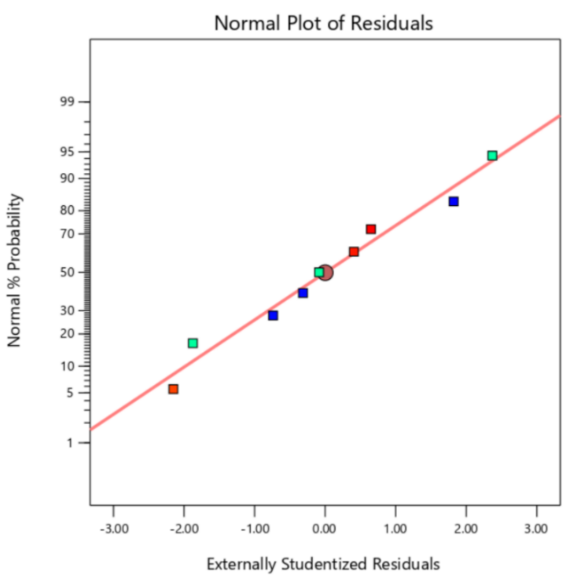

Fig. 11 The normal plot of residuals for spring constant.

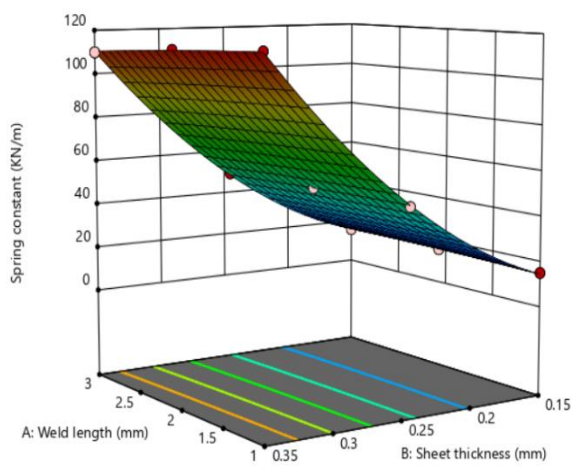

Fig. 12 The interaction contour of weld length and sheet thickness on bellows spring constant.

Investigating the P-values of weld length and sheet thickness indicates that both parameters are significant although the effect of sheet thickness is greater than weld length. Increasing sheet thickness causes to increase in the spring constant. The rate of variations spring constant under the effect of weld length is nearly constant compared to sheet thickness. Sheet thickness and weld length have a direct relation with the spring constant. Maximum spring constant occurs when the sheet thickness is maximum, and vice versa. Figure 12 shows the contour of interaction weld length and sheet thickness on spring constant.

3.4. Fatigue Life

As it has been displayed before, sheet thickness has a greater effect on the characteristics of bellows but due to its effect on deflection and spring constant, it can be indicated that it can bring certain limitations. According to the results and modified-goodman criteria, in weld length 2 mm with increasing sheet thickness from 0.15 mm to 0.35 mm, the life cycle of bellows increases from 2.95×10^3 cycles to 1.23×10^6 cycles. Also, in 0.15 mm sheet thickness with increasing weld length from 1 mm to 3 mm, the life cycle of bellows increases from 1.71×10^3 cycles to 3.90×10^3 cycles.

The increase in fatigue life is due to a decrease in stress and the maximum fatigue life with 1.23×10^6 cycles occurs in sheet thickness of 0.35 mm and weld length of 2 mm. The minimum fatigue life with 1.71×10^3 cycles occurs in sheet thickness of 0.15 mm and weld length of 1 mm, which shows that the effect of bellows design parameters is important on bellows fatigue life.

4 CONCLUSIONS

In this study, the effects of weld length and sheet thickness on the mechanical characteristics of welded bellows were investigated and the predictive models were constructed based on the response surface and ANOVA method. The summary of results is as follows:

- The results indicated that stress concentration occurs on the inside edges of the bellows where it is connected to the weld zone. Moreover, the acceptable range of the parameters was obtained.
- According to results, increasing sheet thickness and weld length causes a decrease in stress and deformation and increases bellows constant spring.
- It was realized that while both parameters affect the characteristic of bellows, the effect of sheet thickness was greater than that of the weld length.
- The effect of the parameters on the fatigue life of the bellows based on the modified-goodman criteria indicated that an increase in both parameters results in greater life cycles.

ACKNOWLEDGMENTS

We are grateful to the Research Council of Shahid Chamran University of Ahvaz for financial support (SCU.EM1402.73332).

REFERENCES

[1] Wen, H. J., Lo, Y. L., Chang, K. H., and Wen, F. L., Analysis of Feature and Welding Consideration for Metal Bellows. Key Engineering Materials, Vol. 486, 2011, pp. 225-228.

[2] Dureja, A., Sapra, M., Pandey, R., Chellapandi, P. Sharma, B., Kayal, J., Chetal, S., and Sinha, R., Design, analysis and Shape Optimisation of Metallic Bellows for Nuclear Valve Applications, 2011.

[3] Duffy, K. P., Szpak, G., Dynamic Bellows for a Pulse Tube Cryocooler Application, In AIAA SCITECH 2022 Forum, 2022.

[4] Gheni, M., Kikuchi, M., Shape Optimization of Metal Welded Bellows Seal Based on The Turing Reaction-Diffusion Model Coupled with FEM, Key Engineering Materials, Vol. 385, 2008, pp. 813-816.

[5] Nagamachi, T., Mishiba, T., and Katsuki, K., Deformation and fatigue characteristics of large Welded Bellows with Inclined External Edge, Materials Transactions, Vol. 49, No. 6, 2008, pp. 1249-1255.

[6] Tarabrin, G., Spatial Bellows-Type (Sylphon) Construction, Mechanics of Solids, Vol. 56, No. 2, 2021, pp. 162-170.

[7] Yuan, Z., Huo, S., and Ren, J., Mathematical Description and Mechanical Characteristics of Reinforced S-Shaped Bellows, International Journal of Pressure Vessels and Piping, Vol. 175, 2019, pp. 103931.

[8] Gheni, M., Musha, H., Yusup, N., and Baki, K., Flexibility Analysis of The Welded Metal Bellows of Mechanical Seal, Key Engineering Materials, Vol. 462, 2011, pp. 894-899.

[9] Xiang, X., Lu, G., Li, Z., and Lv, Y., Finite Element Analysis and Experimental Study on A Bellows Joint, Engineering Structures, Vol. 151, 2017, pp. 584-598.

[10] Li, H., Dong, J. Wang, J., Mei, Q., Ma, Y., and Wang, Z., Stress–Strain Analysis of S-Shaped Welded Metal Bellows Under Axial Load Based on Finite Element Analysis and Experimental Validation, Science of Advanced Materials, Vol. 14, No. 5, 2022, pp. 943-952.

[11] Piao, C. H., Cho, C. D., Kim, C. B., and Pang, Q., Experiment Study and Finite Element Analysis of Spring Constant of Welded Metal Bellows, Key Engineering Materials, Vol. 326, 2006, pp. 537-540.

[12] Cho, H. Y., Nam,G. J., Oh, B. K., Kim, Y. H., Lee, J. H., and Suh, J., A Development of CAD Program for Metal Bellows Diaphragm, Transactions of the Korean Society of Mechanical Engineers A, Vol. 27, No. 3, 2003, pp. 401-408.

[13] Kim, D. H., Park, J. G., Kim, D., Kim, J. O., Lee, I. H., and Cho, H. Y., CAD Program for Design of Metal Bellows. Global Journals of Research in Engineering, Vol. 13, No. A9, 2013, pp. 23-28.

[14] Nuer, R., Gheni, M., Ahmat, M., and Jia, L. H., Fem Analysis and Optimization for Welded Metal Bellows Seal, Advanced Materials Research, Vol. 33, 2008, pp. 1371-1376.

[15] Prasanna Naveen Kumar, J., Johns Kumar, S., Sarathi Jeyathilak, R., Venkatesh, M., Simon Christopher, A., and Ganesh, K., Effect of Design Parameters on The Static Mechanical Behaviour of Metal Bellows Using Design of Experiment and Finite Element Analysis, International Journal on Interactive Design and Manufacturing (Ijidem), Vol. 11, 2017, pp. 535-545.

[16] Yan, M., Wang, M. Y., Xu, Z. F., Liu, Y., Chen, L., and Huang, H. G., Analysis on the Bending Deformation Characteristic and Crack Failure Mechanism of Thin-Walled Stainless-Steel Bellows, Engineering Failure Analysis, Vol. 143, 2023, pp. 106900.

[17] Hwang, Y. M., Zhang, C. H., Chen, C. C., Yoshihara, S., Feeding Path and Movable Die Design in Tube Hydroforming of Metal Bellows, The International Journal of Advanced Manufacturing Technology, Vol. 129, No. 5, 2023., pp. 2399-2414.

[18] Ma, Y., Zhang, J.,Yuan, Q., Song, Z., Pang, H., and Su, T., Numerical and Experimental Investigation of Thin-Walled Bellows Considering Non-Uniform Wall Thickness Under Displacement Load, The International Journal of Advanced Manufacturing Technology, Vol. 129, No. 9, 2023, pp. 4059-4072.

[19] Wang, Q., Chu, G., Sun, L., Ling, C., and Liu, X., Numerical and Experimental Study on Axial Hydroforging Process of 5A03 Aluminium Alloy S-Shaped Bellows, The International Journal of Advanced Manufacturing Technology, 2023, pp. 1-16.

[20] Jiang, Z., Liang, D., Zhou, T., and Tong, L., Study on Welding Process of 7× 0.5 Multilayer 304 Bellows and Flange. in IOP Conference Series: Materials Science and Engineering, IOP Publishing, 2020.

[21] Guo, H., Wang, L., Yin, J., Yao, C., Zhang, C., and Luo, J., Finite Element Simulation Prediction of Repeated Bending Failure Zone of Roll-Welded Bellows Based on an Equivalent Welding Model, Engineering Failure Analysis, 2023, pp. 107371.

[22] Krovvidi, S. K., Das, C., Toppo, A., Ramesh, E., Ravikumar, R., Suresh, L., Parthasarathi, N., Mahadevan, S., Albert, S. K., and Sureshkumar, K., Failure Analysis of Large Stroke Welded Disk Bellows in Storage. Journal of Failure Analysis and Prevention, Vol. 23, No. 1, 2023, pp. 245-257.

[23] GRANTAEduPack Commercial Software, Documents, 2018.

[24] Azqandi1a, M. S., Hassanzadeh, M., and Arjmand M., Sensitivity Analysis Based on Complex Variables in FEM for Linear Structures, Vol. 4, 2019, pp. 15-32.

[25] Sheikhi Azqandi, M., Hassanzadeh, M., First-and Second-Order Sensitivity Analysis of Finite Element Models Using Extended Complex Variables Method, Archive of Applied Mechanics, Vol. 91, No. 10, 2021, pp. 4263-4277.

[26] Richard G. Budynas, J. K. N., Shigley's Mechanical Engineering Design. 9th ed. (McGraw-Hill series in mechanical engineering), New York: McGraw-Hill, 2011.

Int. J. Advanced Design and Manufacturing Technology, 2025, Vol. 18, No. 1, pp. 29-36

DOI: *ISSN: 2252-0406* *https://admt.isfahan.iau.ir*

Optimization of the Mechanical Properties of Al-C Nanocomposite via Response Surface Methodology: A Molecular Dynamics Study

Mostafa Yazdani, Aazam Ghassemi *, Mohamad Shahgholi, Javad Jaafari Fesharaki, Seyed Ali Galehdari
Department of Mechanical Engineering,
Najafabad branch, Islamic Azad University, Najafabad, Iran
*Corresponding author
Email: mostafayazdani2020@gmail.com, a_ghassemi@iau.ac.ir,
mohamad.shahgholi@iau.ac.ir, javafjafari@iau.ac.ir, ali.galehdari@iau.ac.ir

Received: 29 June 2024, Revised: 18 November 2024, Accepted: 11 December 2024

Abstract: Nowadays, various methods are being developed for new composites and nanocomposite compounds. Investigating the properties of nanocomposites and finding their optimal properties can enhance their utility. In this study, the mechanical molecular dynamics method was initially utilized to investigate the mechanical properties of an aluminum/carbon (Al/C) nanocomposite. Subsequently, the effect of temperature change, strain rate, and carbon content on the nanocomposite's elastic modulus and ultimate strength were investigated. To simultaneously investigate these three parameters and identify the optimal point for the elastic modulus and ultimate strength, the experimental design method for optimization was utilized. The Derringer method was utilized to determine the optimal parameters for the simultaneous optimization of two response variables, i.e., elastic modulus and ultimate strength. The findings reveal that the optimal conditions occur simultaneously at 300 K, strain rate of 0.01, and carbon content of 2 %, with an elastic modulus value of 51.046 GPa and an ultimate strength value of 5.1117 GPa. Finally, the results obtained from the RSM method were also compared with the molecular dynamics method.

Keywords: Mechanical Properties, Nanocomposites, Optimization, Response Surface Methodology

Biographical notes: Mostafa Yazdani received his MSc in Mechanical Engineering from the University of IAU Arak Branch in 2013. He is currently a PhD student at the Department of Mechanical Engineering, IAU Najafabad Branch. His current research interest includes Molecular Dynamic and Coating. **Azam Ghassemi** is an Associate Professor of Mechanical Engineering at the IAU Najafabad Branch. She received her PhD in Mechanical Engineering from Isfahan University of Technology in 2010. **Mohamad Shahgholi** is an Associate Professor of Mechanical Engineering at the IAU Najafabad Branch. He received his PhD in Mechanical Engineering from Politecnico di Milano in 2015. **Javad Jafari** is an Associate Professor of Mechanical Engineering at the IAU Najafabad Branch. He received his PhD in Mechanical Engineering from Kashan University in 2014. **Seyed Ali Galehdari** is an Assistant Professor of Mechanical Engineering at the IAU Najafabad Branch. He received his PhD in Mechanical Engineering from Ferdowsi University of Mashhad in 2015.

Research paper

1 INTRODUCTION

Numerous advancements are occurring in the field of novel materials, including composites [1]. Various research investigations are being carried out on novel composite and nanocomposite materials. In the realm of nanotechnology, there is a significant focus on conducting thorough studies utilizing innovative techniques [2]. Nanocomposites are advanced materials that possess exceptional properties due to their distinctive design and composition. With a yearly expansion rate of approximately 25%, these materials exhibit enormous potential for a diverse range of applications [3].

Nanocomposites demonstrate pragmatic characteristics. By integrating nanocomposites into material processing, it is feasible to manufacture ceramics and porous materials that are either single-phase or multi-phase and possess unique properties [4]. Over the past few years, carbon nanotube-reinforced metal composites have garnered interest from numerous researchers and scientists, owing to the distinct mechanical properties of CNTs [5-14]. In recent years, the aluminum/carbon nanotube composite has emerged as a popular topic of discussion and study within the field of metal composites [15]. Esawi et al. [16] utilized ball milling to incorporate 2 weight percent of carbon nanotubes into aluminum, resulting in a 21% rise in the tensile strength of aluminum.

Liu et al. [17] produced an aluminum/carbon nanotube composite utilizing a blend of powder metallurgy and Subsequent Friction Stir Processing (FSP). Microstructural analyses revealed that the carbon nanotubes were dispersed individually throughout the composites and had a tendency to disperse along the grain boundaries. Despite the shortening of carbon nanotubes and the formation of Al_4C_3 in the matrix, the layered structure of carbon nanotubes remained intact. Kim et al. [18] assessed the friction and wear properties of carbon nanotube composites under various conditions, such as dispersion rate, fabrication method, and carbon nanotube content. Wu et al. [19] examined the mechanical and thermal properties of aluminum/carbon nanotube composites. Using the Spark Plasma Sintering (SPS) method, they developed aluminum composites reinforced with multi-walled carbon nanotubes at concentrations ranging from 0 to 5.0 weight percent. The 0.5-weight percent multi-walled aluminum/carbon nanotube composite demonstrated a maximum thermal conductivity of 199 W/ m/ K and a maximum tensile strength of 130 MPa. These findings suggest that the multi-walled carbon nanotube aluminum matrix composite is a suitable material for high thermal conductivity applications.

Chen et al. [20] discovered that aluminum/carbon nanotube composite exhibits improved ductility with increased tensile strength. In a separate study, Izadi et al. [21] employed a multi-pass friction stir process to generate an aluminum/multi-walled carbon nanotube composite, which exhibited double the hardness of the original alloy.

Liu et al. [22] examined the carbon nanotube shortening and strength of aluminum/carbon nanotube composites produced through multi-pass friction stir processing. The carbon nanotubes were dispersed in an aluminum matrix with a concentration of 4.5 vol. % CNT. Their analysis revealed that the change in length of carbon nanotubes has a linear relationship with the mechanical properties of the composite. Bakshi et al. [23] analyzed the tensile strength data of aluminum/carbon nanotube composites to investigate the impact of carbon nanotube dispersion and volume fraction on the elastic modulus, strength, and hardness of composites. The highest strength was observed for carbon nanotubes with a volume fraction of less than 2 vol. %. Additionally, the tensile data of magnesium/carbon nanotube and copper/carbon nanotube composites were compared with aluminum/carbon nanotube composites, revealing that reinforcement is not effective in the absence of chemical interaction between the metal matrix and the carbon nanotube.

To enhance ductility, Salama et al. [24] introduced a microstructural design of aluminum/carbon nanotube composite, revealing that dual matrix structure composites have approximately 14.8% more ductility than single matrix structure composites. The effect of carbon nanotube damage on the mechanical properties of aluminum/carbon nanotube composites was investigated by Hassan et al. [25] using damaged carbon nanotubes, which resulted in a 97.5% increase in strength and 14.2% increase in modulus compared to pure aluminum. Park et al. [26] studied the strengthening mechanisms in aluminum/carbon nanotube composites and discovered that the yield strength and tensile strength of aluminum/carbon nanotube composites improved by 60% and 23%, respectively. Due to the time-consuming and costly nature of experimental studies, molecular dynamics simulations have been utilized to predict the mechanical properties of various nanocomposites, including carbon nanotube-metal nanocomposites.

Yan et al. [27] used the molecular dynamics method to study the tensile responses of copper/carbon nanotube nanocomposites, revealing that carbon nanotubes have a significant reinforcing effect on Young's modulus and yield strength of copper/carbon nanotube nanocomposites. Motamedi et al. [28] investigated the mechanical properties of Al/CNT nanocomposites using the molecular dynamics method, as well as the continuum model of the composite and finite element method. They also employed the molecular dynamics method to predict the mechanical properties of other nanostructures. Silvestre et al. [29] studied the compressive behavior of carbon nanotube-reinforced aluminum composites using the molecular dynamics method, revealing that Young's modulus of the composite increased by more than 60% compared to pure aluminum.

In previous studies, a large number of investigations have been conducted on aluminum-based composites; however, no significant study has been carried out on Al/C nanocomposites. Thus, in this research, first, the effect of different parameters including ambient temperature, strain rate, and carbon content utilized in the aluminum matrix have been assessed on the mechanical properties of Al/C nanocomposite. Then, the prediction and optimization of mechanical properties of Al/C nanocomposite have been fulfilled via response surface methodology.

2 SIMULATION METHOD

Molecular Dynamics (MD) simulation is a computational technique that enables the study of the macroscopic properties of a system by examining its microscopic properties. The simulation creates a scenario in which the atoms of the system interact with each other over a specified period of time. The simulation solves Newton's equation of motion for the atoms of the system, and numerical equations are used to determine their properties due to the high number of components in each system. In the present research, the aluminum-carbon nanocomposite was subjected to uniaxial tension using molecular dynamics simulation and LAMMPS package software, and periodic boundary conditions were considered (“Fig. 1”).

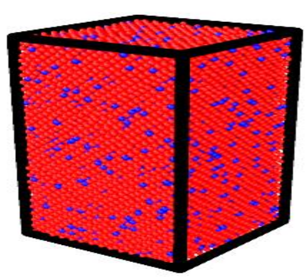

Fig. 1 Simulation box of Al-C.

The AIREBO [30-31], EAM [32], and Lennard-Jonse [33] potentials were utilized to describe the interactions between C-C, Al-Al, and Al-C atoms, respectively. The aluminum-carbon nanocomposite box's dimensions were set to 80 × 80 × 80 Å^3. The NPT ensemble was used to balance the system, with variables representing the number of atoms, ambient pressure, and temperature. The system was found to be in perfect equilibrium with a relaxation time of 1000 ps and a time step of 1 fs. The tensile properties of the aluminum-carbon nanocomposite, including elastic modulus and ultimate tensile strength, were investigated at different temperatures of 300, 400, 450, and 600 K and strain rates of 0.001 /ps, 0.003 /ps, 0.005 /ps, 0.007 /ps, and 0.01 /ps, under ambient pressure of 100 KPa and different percentages of carbon content in the alloy, ranging from 2 % to 6 %.

3 RESULTS AND DISCUSSION

3.1. Effect of Different Parameters on the Mechanical Properties

3.1.1. Effect of Ambient Temperature

In this part, the effect of different ambient temperatures of 300, 400, 450, and 600 K has been evaluated on the mechanical properties of the Al/C nanocomposite as can be shown in “Fig. 1”. The content of C used in the aluminum matrix is 2 %. Also, the Al/C nanocomposite has been simulated under uniaxial tension with a strain rate of 0.001/ps. “Table 1” shows the values of the mechanical properties derived from “Fig. 2”.

Table 1 The values of the mechanical properties of Al/C nanocomposite at different ambient temperatures

Temperature, K	Elastic modulus, GPa	Ultimate tensile strength, GPa
300	51.074	4.68
400	49.655	4.194
450	46.653	3.797
600	44.942	2.943

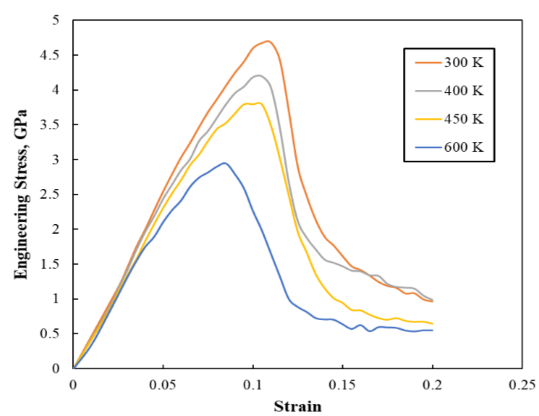

Fig. 2 Stress-strain curves of Al/C nanocomposite at different ambient temperatures.

It can be found from “Table 1” that by increasing the ambient temperature from 300 to 600 K, the elastic modulus and ultimate tensile strength have decreased by 12.006 % and 37.115 %, respectively.

3.1.2. Effect of the Strain Rate

In this subsection, the effect of different strain rates of 0.001, 0.003, 0.005, 0.007, and 0.01/ps has been evaluated on the mechanical properties of Al/C nanocomposite which has been simulated under uniaxial tension at the ambient temperature of 300 K. The carbon content used in the aluminum matrix is 2 %. Figure 3 shows the stress-strain curves at different strain rates and "Table 2" illustrates the values of obtained mechanical properties from "Fig. 3".

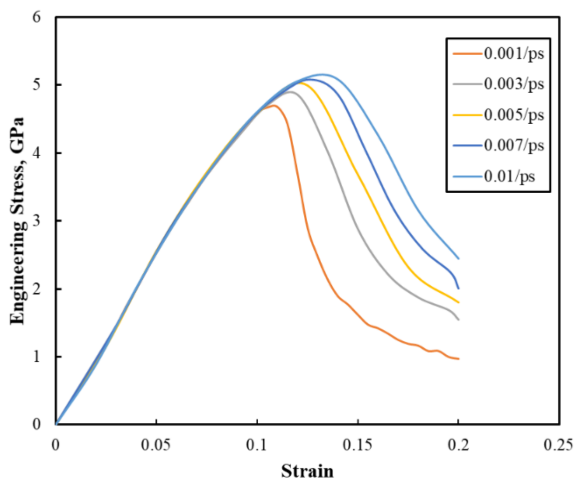

Fig. 3 Stress-strain curves of Al/C nanocomposite at different strain rates.

Table 2 The values of the mechanical properties of Al/C nanocomposite at various strain rates

Strain rate, 1/ps	Elastic modulus, GPa	Ultimate tensile strength, GPa
0.001	51.074	4.68
0.003	50.245	4.862
0.005	51.163	4.993
0.007	50.975	5.081
0.01	50.95	5.087

It can be understood from "Table 2" that by increasing the strain rate from 0.001/ps to 0.01/ps, the elastic modulus has remained constant and the ultimate tensile strength has enhanced by 8.696 %.

3.1.3. Effect of the Carbon Content

In this part, the effect of carbon content from 2 to 6 % utilized in the aluminum matrix has been assessed on the mechanical properties of Al/C nanocomposite. The nanocomposite has been simulated under uniaxial tension at the strain rate of 0.001/ps and the ambient temperature of 300 K. Figure 4 indicated stress-strain curves of Al/C nanocomposite with different carbon content and the values of the mechanical properties derived from this figure are reported in "Table 3".

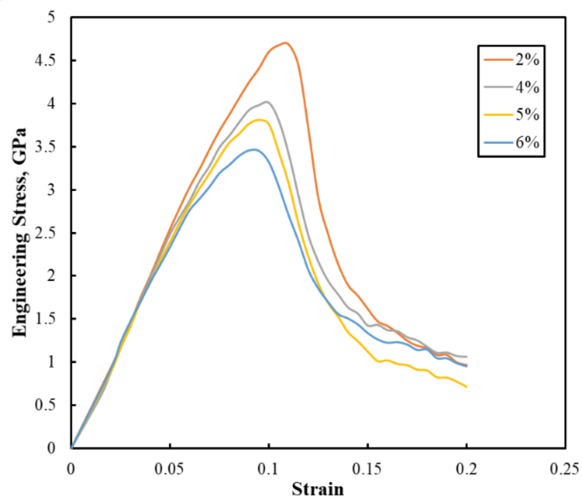

Fig. 4 Stress-strain curves of Al/C nanocomposite.

Table 3 The values of the mechanical properties of Al/C nanocomposite with different carbon content

Content, %	Elastic modulus, GPa	Ultimate tensile strength, GPa
2	51.074	4.68
4	50.392	4.008
5	48.119	3.808
6	48.087	3.459

It can be found from "Table 3" that by increasing the carbon content from 2 to 6 %, the values of elastic modulus and ultimate tensile strength have declined by 5.848 % and 26.089 %, respectively.

3.2. Statistical Modeling and Optimization

In the design of the experiment (DOE), some input parameters, which are known as independent variables, are chosen randomly. Then, some experiments or simulations are conducted to derive the results to utilize them as output parameters, which are known as dependent variables, in DOE and perform some optimizations on them. In this research, strain rate, temperature, and content of carbon utilized in the aluminum matrix are considered input variables, while the output variables are the modulus of Elasticity (E) and Ultimate Tensile Strength (UTS). Furthermore, MINITAB software has been used to execute the Response Surface Methodology (RSM) approach as a DOE method.

The Box-Behnken Design (BBD) is used as the experimentation strategy. The strain rate and temperature have been considered in 4 and 5 levels, respectively, and the number of the levels of carbon content is four, which can be observed in "Table 4".

Table 4 The levels of input parameters

Input parameters	Levels				
Temperature, K	300		400	450	600
Strain rate, 1/ps	0.001	0.003	0.005	0.007	0.01
Content, %	2	4	5		6

Table 5 The values of output variables

Run order	T (K)	S (1/ps)	C (%)	E (GPa)	UTS (GPa)
1	300	0.001	2	51.074	4.68
2	400	0.001	2	49.653	4.194
3	450	0.001	2	46.653	3.797
4	600	0.001	2	44.992	2.943
5	300	0.001	2	51.074	4.68
6	300	0.003	2	50.245	4.682
7	300	0.005	2	51.163	4.993
8	300	0.007	2	50.975	5.081
9	300	0.01	2	50.95	5.087
10	300	0.001	2	51.074	4.68
11	300	0.001	4	50.392	4.008
12	300	0.001	5	48.419	3.808
13	300	0.001	6	48.087	3.459
14	300	0.001	5	48.419	3.808
15	300	0.001	5	48.419	3.808

"Table 5" indicates the values of output variables for 15 simulations in different conditions. T, S, C, E, and UTS in "Table 5" show ambient temperature, strain rate, the content of carbon utilized in the aluminum matrix, elastic modulus, and ultimate tensile strength, respectively.

3.2.1. The Mathematical Modeling for Elastic Modulus

The mathematical modeling for elastic modulus is proposed by analysis of variance (ANOVA). The results of ANOVA for modulus of elasticity have been illustrated in Table 6. Furthermore, the mathematical model for elastic modulus is shown in Equation (1):

$$E = 61.86 - 0.0381\,T - 144\,S - 0.35\,C + 12566\,S*S \quad (1)$$

Where, T is the temperature in Kelvin, C is the carbon content in percent, and S is the strain rate in picoseconds.

As can be observed in Equation (1), the value of E can be obtained as a function of temperature, carbon content, and strain rate. According to the analysis of variance for elastic modulus, the confidence interval is 95 % because the probability value (P-Value) in "Table 6" is remarkably less than 5 %. Moreover, the R^2 and R^2 adjusted correlation coefficients are 93.07 % and 87.87 % for elastic modulus, which show appropriate fittings for the mathematical modeling of elastic modulus proposed by the ANOVA method.

Table 6 Analysis of variance for elastic modulus

Source	DF	Adj SS	Adj MS	F-Value	P-Value
Model	6	46.2788	7.7131	17.91	0.000
Linear	3	35.9790	11.9930	27.84	0.000
T	1	29.8141	29.8141	69.22	0.000
S	1	0.0021	0.0021	0.00	0.946
C	1	9.9389	9.9389	23.07	0.001
Square	3	0.3539	0.1180	0.27	0.843
T*T	1	0.2150	0.2150	0.5	0.500
S*S	1	0.0768	0.0768	0.18	0.684
C*C	1	0.0606	0.0606	0.14	0.717
Error	8	3.4458	0.4307		
Lack-of-Fit	4	3.4458	0.8615	*	*
Pure Error	4	0.0000	0.0000		
Total	14	49.7246			
R-sq = 93.07 %, R-sq(adj) = 87.87 %					

3.2.2. The Mathematical Modeling for Ultimate Tensile Strength

In this part, the mathematical modeling for the ultimate tensile strength method has been shown as follows:

$$UTS = 6.472 - 0.00364\,T + 94.1\,S - 0.301\,C - 4002\,S*S \quad (2)$$

Where, S is the strain rate in picoseconds, T is the ambient temperature in Kelvin, C is the content of carbon in percent, and UTS is the ultimate tensile strength in GPa.

"Table 7" indicates the ANOVA results for ultimate tensile strength.

Table 7 Analysis of variance for ultimate tensile strength

Source	DF	Adj SS	Adj MS	F-Value	P-Value
Model	6	5.83231	0.97205	199.37	0.000
Linear	3	3.72378	1.24126	254.59	0.000
T	1	2.29432	2.29432	470.57	0.000
S	1	0.16925	0.16925	34.74	0.000
C	1	1.19231	1.19231	244.55	0.000
Square	3	0.00998	0.00333	0.68	0.587
T*T	1	0.00319	0.00319	0.65	0.442
S*S	1	0.00778	0.00778	1.6	0.242
C*C	1	0.00002	0.00002	0.00	0.951
Error	8	0.03900	0.00488		
Lack-of-Fit	4	0.03900	0.00975	*	*
Pure Error	4	0.00000	0.00000		
Total	14	5.87132			
R-sq = 99.34 %, R-sq(adj) = 98.84 %					

It can be found from "Table 7" that the probability value of ultimate tensile strength is significantly less than 5 %, and this value is desirable. In addition, for this model, the correlation coefficients of R^2 and R^2 adjusted are 99.34 % and 98.84 %, respectively, which shows the accuracy and adequacy of this model.

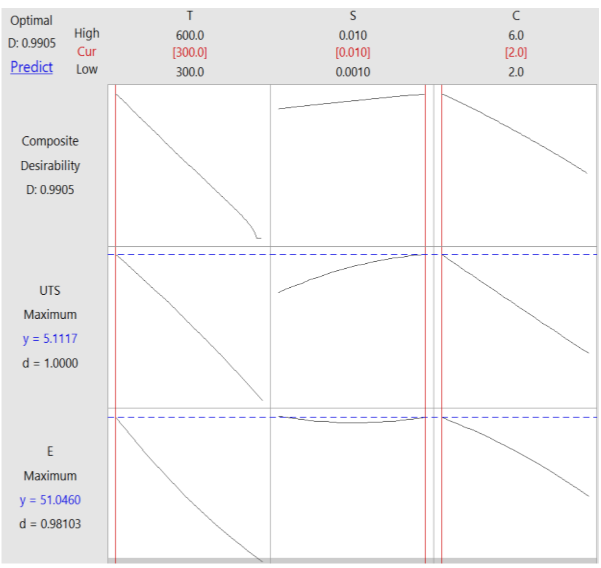

Fig. 5 The optimal values of elastic modulus and ultimate tensile strength proposed by RSM.

3.2.3. Optimization with Desirability Approach

The purpose of the optimization in this study is to maximize the values of ultimate tensile strength and modulus of elasticity by using the desirability approach. For this purpose, the results of the maximization of elastic modulus and ultimate tensile strength are shown in "Fig 5". It is clear in this figure that when the temperature, strain rate, and content of carbon are 300 K, 0.01/ps, and 2 %, respectively, ultimate tensile strength and elastic modulus have their maximum values. According to "Fig. 5", the maximum predicted values of ultimate tensile strength and elastic modulus are 5.1117 GPa and 51.046 GPa, respectively. Then, in order to verify the maximum predicted values of E and UTS, the simulation in the proposed conditions (T = 300 K, S = 0.01/ps, and C = 2 %) has been simulated, which can be seen in "Fig. 6". In this figure, the values of elastic modulus and ultimate tensile strength are 50.95 GPa and 5.087 GPa, respectively. The accuracy of the predicted and simulated value of elastic modulus is 99.811 %, also 99.514 % for ultimate tensile strength, which shows that the proposed model is profoundly desirable.

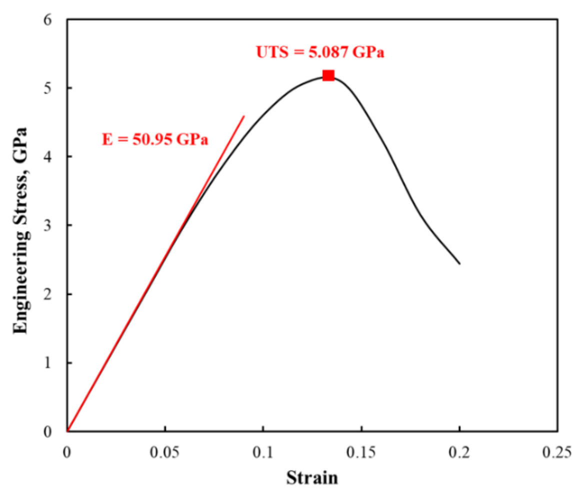

Fig. 6 Stress-strain curve of Al-Cu alloy for the proposed model.

4 CONCLUSIONS

In this study, first, the effect of ambient temperature, strain rate, and carbon content used in the aluminum matrix have been investigated on the mechanical properties of Al/C nanocomposite. The results showed that by increasing the temperature from 300 to 600 K, the elastic modulus and ultimate tensile strength decreased by 12.006 % and 37.115 %, respectively. Furthermore, by enhancing the strain rate from 0.001/ps to 0.01/ps, the E remained constant and UTS grew by 8.696 %. Moreover, the higher the carbon content, the lower the E and UTS. Then, some mathematical models were proposed by ANOVA for the prediction of E and UTS. Eventually, the E and UTS were simultaneously optimized through response surface methodology and validated via molecular dynamics simulation.

REFERENCES

[1] Kelly, A., Composites in Context, Composites Science and Technology, Vol. 23, No. 3, 1985, pp. 171-199.

[2] Thostenson, E. T., Li, C., and Chou, T. W., Nanocomposites in Context, Composites science and Technology, Vol. 65, No. 3, 2005, pp. 491-516.

[3] Camargo, P. H. C., Satyanarayana, K. G., and Wypych, F., Nanocomposites: Synthesis, Structure, Properties and New Application Opportunities, Materials Research, Vol. 12, No. 1, 2009, pp. 1-39.

[4] Komarneni, S., Nanocomposites, Journal of Materials Chemistry, Vol. 2, No. 12, 1992, pp. 1219-1230.

[5] Tsai, P. C., Jeng, Y. R., Lee, J. T., Stachiv, I., and Sittner, P., Effects of Carbon Nanotube Reinforcement and Grain Size Refinement Mechanical Properties and Wear Behaviors of Carbon Nanotube/Copper Composites, Diamond and Related Materials, Vol. 74, 2017, pp. 197-204.

[6] Bakshi, S. R., Lahiri, D., and Agarwal, A., Carbon Nanotube Reinforced Metal Matrix Composites-A Review, International Materials Reviews, Vol. 55, No. 1, 2010, pp. 41-64.

[7] Burkholder, G. L., Kwon, Y. W., and Pollak, R. D., Effect of Carbon Nanotube Reinforcement on Fracture Strength of Composite Adhesive Joints, Journal of Materials Science, Vol. 46, No. 10, 2011, pp. 3370-3377.

[8] Park, Y. G., Min, H., Kim, H., Zhexembekova, A., Lee, C. Y., and Park, J. U., Three-Dimensional High-Resolution Printing of Carbon Nanotube/Liquid Metal Composites with Mechanical and Electrical Reinforcement, Nano letters, Vol. 19, No. 8, 2019, pp. 4866-4872.

[9] Carreño-Morelli, E., Yang, J., Couteau, E., Hernadi, K., Seo, J. W., Bonjour, C., and Schaller, R., Carbon Nanotube/Magnesium Composites, Physica Status Solidi (a), Vol. 201, No. 8, 2004, pp. 53-55.

[10] Ni, X., Furtado, C., Fritz, N. K., Kopp, R., Camanho, P. P., and Wardle, B. L., Interlaminar to Intralaminar Mode I And Ii Crack Bifurcation Due to Aligned Carbon Nanotube Reinforcement of Aerospace-Grade Advanced Composites, Composites Science and Technology, Vol. 190, 2020, pp. 108014.

[11] Li, Q., Viereckl, A., Rottmair, C. A., Singer, R. F., Improved Processing of Carbon Nanotube/Magnesium Alloy Composites, Composites Science and Technology, Vol. 69, No. 7-8, 2009, pp. 1193-1199.

[12] Uddin, S. M., Mahmud, T., Wolf, C., Glanz, C., Kolaric, I., Volkmer, C., and Fecht, H. J., Effect of Size and Shape of Metal Particles to Improve Hardness and Electrical Properties of Carbon Nanotube Reinforced Copper and Copper Alloy Composites, Composites Science and Technology, Vol. 70, No. 16, 2010, pp. 2253-2257.

[13] Silvestre, N., State-of-the-Art Review on Carbon Nanotube Reinforced Metal Matrix Composites, International Journal of Composite Materials, Vol. 3, No. 6, 2013, pp. 28-44.

[14] Kuzumaki, T., Ujiie, O., Ichinose, H., and Ito, K., Mechanical Characteristics and Preparation of Carbon Nanotube Fiber-Reinforced Ti Composite, Advanced Engineering Materials, Vol. 2, No. 7, 2000, pp. 416-418.

[15] Tjong, S. C., Recent Progress in The Development and Properties of Novel Metal Matrix Nanocomposites Reinforced with Carbon Nanotubes and Graphene Nanosheets, Materials Science and Engineering, R: Reports, Vol. 74, No. 10, 2013, pp. 281-350.

[16] Esawi, A. M., Morsi, K., Sayed, A., Gawad, A. A., and Borah, P., Fabrication and Properties of Dispersed Carbon Nanotube–Aluminum Composites, Materials Science and Engineering: A, Vol. 508, No. 1-2, 2009, pp. 167-173.

[17] Liu, Z. Y., Xiao, B. L., Wang, W. G., and Ma, Z. Y., Singly Dispersed Carbon Nanotube/Aluminum Composites Fabricated by Powder Metallurgy Combined with Friction Stir Processing, Carbon, Vol. 50, No. 5, 2012, pp. 1843-1852.

[18] Kim, I. Y., Lee, J. H., Lee, G. S., Baik, S. H., Kim, Y. J., and Lee, Y. Z., Friction and Wear Characteristics of The Carbon Nanotube–Aluminum Composites with Different Manufacturing Conditions, Wear, Vol. 267, No. 1-4, 2009, pp. 593-598.

[19] Wu, J., Zhang, H., Zhang, Y., and Wang, X., Mechanical and Thermal Properties of Carbon Nanotube/Aluminum Composites Consolidated by Spark Plasma Sintering, Materials and Design, Vol. 41, 2012, pp. 344-348.

[20] Chen, B., Kondoh, K., Imai, H., Umeda, J., and Takahashi, M., Simultaneously Enhancing Strength and Ductility of Carbon Nanotube/Aluminum Composites by Improving Bonding Conditions, Scripta Materialia, Vol. 113, 2016, pp. 158-162.

[21] Izadi, H., Gerlich, A. P., Distribution and Stability of Carbon Nanotubes During Multi-Pass Friction Stir Processing of Carbon Nanotube/Aluminum Composites, Carbon, Vol. 50, No. 12, 2012, pp. 4744-4749.

[22] Liu, Z. Y., Xiao, B. L., Wang, W. G., and Ma, Z. Y., Analysis of Carbon Nanotube Shortening and Composite Strengthening in Carbon Nanotube/Aluminum Composites Fabricated by Multi-Pass Friction Stir Processing, Carbon, Vol. 69, 2014, pp. 264-274.

[23] Bakshi, S. R., Agarwal, A., An analysis of the Factors Affecting Strengthening in Carbon Nanotube Reinforced Aluminum Composites, carbon, Vol. 49, No. 2, 2011, pp. 533-544.

[24] Salama, E. I., Abbas, A., and Esawi, A. M., Preparation and Properties of Dual-Matrix Carbon Nanotube-Reinforced Aluminum Composites, Composites Part A: Applied Science and Manufacturing, Vol. 99, 2017, pp. 84-93.

[25] Hassan, M. T., Esawi, A. M., and Metwalli, S., Effect of Carbon Nanotube Damage on The Mechanical Properties of Aluminium–Carbon Nanotube Composites, Journal of Alloys and Compounds, Vol. 607, 2014, pp. 215-222.

[26] Park, J. G., Keum, D. H., and Lee, Y. H., Strengthening Mechanisms in Carbon Nanotube-Reinforced Aluminum Composites, Carbon, Vol. 95, 2015, pp. 690-698.

[27] Yan, Y., Lei, Y., and Liu, S., Tensile Responses of Carbon Nanotubes-Reinforced Copper Nanocomposites: Molecular Dynamics Simulation, Computational Materials Science, Vol. 151, 2018, pp. 273-277.

[28] Motamedi, M., Naghdi, A., and Jalali, K., Effect of Temperature on Properties of Aluminum/Single-Walled Carbon Nanotube Nanocomposite by Molecular Dynamics Simulation, Proc IMechE Part C: J. Mechanical Engineering Science, Vol. 234, No. 2, 2019, pp. 635-642

[29] Silvestre, N., Faria, B., and Lopes, J. N. C., Compressive Behavior of CNT-Reinforced Aluminum Composites Using Molecular Dynamics, Composites Science and Technology, Vol. 90, 2014, pp. 16-24.

[30] Stuart, S. J., Tutein, A. B., and Harrison, J. A., A Reactive Potential for Hydrocarbons with Intermolecular Interactions, The Journal of Chemical Physics, Vol. 112, No. 14, 2000, pp. 6472-6486.

[31] Wei, Y., Wu, J., Yin, H., Shi, X., Yang, R., and Dresselhaus, M., The Nature of Strength Enhancement and Weakening by Pentagon–Heptagon Defects in Graphene, Nature materials, Vol. 11, No. 9, 2012, pp. 759-763.

[32] Motamedi, M., Mehrvar, A., Nikzad, M., Mechanical Properties of Aluminum/SiNT Nanocomposite, Proceedings of the Institution of Mechanical Engineers, Part C: Journal of Mechanical Engineering Science, Vol. 236, No. 23, 2022, pp. 11322-11329.

[33] Motamedi, M., Mehrvar, A., and Nikzad, M., Statistical Modelling and Optimization of AL/CNT Composite Using Response Surface-Desirability Approach, Computational Particle Mechanics, Vol. 10, No. 1, 2023, pp. 143-153.

Int. J. Advanced Design and Manufacturing Technology, 2025, Vol. 18, No. 1, pp. 37-49

DOI: *ISSN: 2252-0406* *https://admt.isfahan.iau.ir*

Analyzing the Dynamic Performance of the Two-Stage Pusher Centrifuge

Mehdi Jafari Vardanjani*, Hamed Barghikar
Department of Mechanical Engineering,
National University of Skills (NUS), Tehran, Iran
E-mail: m-jafari@nus.ac.ir, hbarghikar@nus.ac.ir
*Corresponding author

Received: 1 June 2024, Revised: 9 November 2024, Accepted: 11 December 2024

Abstract: Mechanical filtration of solid and liquid phases with the help of a centrifuge mechanism is a common operation in industries, particularly for salt dehydration. The process is mainly based on the centrifuge action between particles and fluids. Currently, most of the studies have been performed on single-stage centrifuges while there it is required to know and analyze the behaviour of the multi-stage pusher centrifuges in order to optimize their efficiency. The structure and dynamic performance of the two-stage pusher centrifuge device have been analyzed in the current study in three phases: modal, particle behaviour, and transient state dynamics analysis. The results of the modal analysis have demonstrated that the safety margin obtained in the context of the resonance occurrence for the internal basket set and subset due to linear and rotational inertial forces has been 40%. Based on the results of the transient dynamics analysis, the stability of the particle behavior has been about 5.5 s or 68% of the particle feeding time, the maximum displacement at the critical point of the inner basket subset has been 0.51 mm, and the critical stress value has been about 27 MPa; which has been acceptable in terms of mechanical strength of the assembly versus the stresses and strains caused by the operation of the device. Thus, it is recommended based on the results to maintain the maximum rotational motion (36.68 rad/s) and no significant change in the particle feeding rate compared to the specified value (0.56 kg/s).

Keywords: Dynamic Analysis, Modal Analysis, Pusher Centrifuge

Biographical notes: Mehdi Jafari Vardanjani is an Assistant Professor of Mechanical Engineering at the National University of Skills (NUS), Iran. He received his PhD in Manufacturing from the University of Tehran, Iran in 2016 and his MSc from the Isfahan University of Technology, Iran. His current research interest includes vibrational effects in mechanics and manufacturing processes. **Hamed Barghikar** is an Assistant Professor of Mechanical Engineering at the National University of Skills (NUS), Iran. He received his PhD in Manufacturing from the Isfahan University of Technology, Iran in 2018, and his MSc from the Isfahan University of Technology, Isfahan, Iran. His current research interest includes machining, metal forming, and polymer processing.

Research paper

1 INTRODUCTION

Mechanical filtration of solid and liquid phases is a common operation in industries including chemical, pharmaceutical, wastewater treatment, and food industries [1]. In this regard, centrifuges are used for a wide range of applications, the most common of which is related to dewatering [2]. Pusher centrifuge device is used for dewatering, drying, and separating materials (fibers, crystals, and powders) continuously. Input mixture enters the centrifuge through the feed pipe and is distributed uniformly inside the centrifuge basket when it goes to the distributor. Then the solid phase formed on the basket can be washed away by water jets. In fact, the dehydration process is done by the centrifugal force created in the centrifuge while the discharge of the dried solid phase is done. Therefore, the performance of the device is influenced by parameters such as the rotational balance of the device during material feeding, dewatering, and separation operations, and the static strength. Thus, the performance of the device is considerably influenced by the feeding rate of materials and their circulation during the working cycle. These parameters also affect the depreciation and noise pollution of the device. Therefore, it is crucial to analysis the structure and dynamic performance of the device.

Bowl and tube centrifuges are used for the effective separation of fine solids due to their high centrifugal acceleration [3]. Sedimentation might also occur during the centrifugal process. The rheological behavior of the sediments affects its shape. However, the shape of the deposit has a significant effect on the flow conditions inside the centrifuge. This affects the efficiency and speed of the separation [4]. The performance of centrifuges has been evaluated in the initial studies based on the Sigma method [5]. In this method, the complexity of turbulent flow conditions and growing sediments are ignored. This causes discrepancies between the results of the evaluation of separation performance in practice and theoretical discussions [3].

Some studies have performed a complete analysis of the flow conditions in centrifuges based on computational fluid dynamics simulation. In this regard, various types of approaches have been observed for simulating turbulent multiphase flows. The approaches used in this field include standard and computational fluid dynamics (CFD) methods developed by researchers [6]. According to the analyzes carried out in the field of separation, it was determined that the examination of the separation process in shell and semi-continuous centrifuges is somewhat dependent on the simulation of the flow conditions. It should be mentioned that the use of simplified models to investigate the different flows of particles and liquids, along with the investigation of the sedimentation effects, have also provided favorable and appropriate results [7].

Since complex multiphase flows occur in the centrifuges, the arrangement of the centrifuge machine parts, process control parameters, and material properties affect the flow paradigm. Although to design a centrifuge or its mechanical separation process, it is necessary to know the flow conditions, the experimental investigation of the flow inside the centrifuges is very complicated. Therefore, CFD is a suitable alternative to practical testing. In this regard, Bürger and colleagues [7] investigated the sediment formation process using a simple approach in centrifuges. In this analysis, the settling behavior of materials is described only by the flux density function. The numerical results have shown a good agreement with the experimental results of a centrifugal process.

Romani et al [3] investigated the sedimentation process in a solid bowl centrifuge with Euler-Lagrangian characteristics. The flow of all three phases in centrifuges is directly resolved spatially and temporally, which requires a long time to perform calculations. Therefore, a period of time has been considered to analyze this trend. In general, the methods used in the previous studies in the past research considered compromises between all the results and the calculation time, which is a normal procedure.

Although there has been extensive research in the field of bowl and tube centrifuges, and the fluid laws that govern them, the topic of two-stage and multi-stage separator pusher centrifuges has rarely been analyzed [8]. Two-stage centrifuges are among the separating centrifuges whose discharge is done in stages that allow continuous operation. In these centrifuges, all steps of separation, washing, drying, and depletion can be done at the maximum speed of the device. In addition to designing a suitable structure, these centrifuges have a low power consumption, high capacity, and the capability to extract materials continuously and maintain humidity in low amounts. Therefore, this device is used in many chemical industries to separate materials from heterogeneous phases and dehydrate mixtures containing crystals or fibrous solids [9].

Currently different theoretical researches have been done on two-stage pusher centrifuges. The main reason for this issue is the complexity and variety of centrifuge separation processes. Mainly, the inability to determine the dimensions, shape, and movements of particles accurately due to the irregular conditions created on them, makes complex mathematical problems. This issue leads to difficulties in conducting theoretical studies of this process. On the other hand, parameter optimization based solely on experimental tests is not very reliable and costly. Therefore, in order to determine the laws governing fluid flow in the centrifuge process, appropriate mathematical models can be developed [10]. For spatial and temporal numerical simulations, an approach based on the fast Eulerian-Ferry method [11] has been devised to achieve a balance between the required physical accuracy and calculation time. In this method, the solid phase (desired salt powder particles) and the liquid phase are approximated as a mixed phase. Therefore, in order to consider the effect of different conditions of the flow behavior of the desired mixture, the average spatial and temporal viscosity of the fluid and the average size of the particles have been considered. The velocity field $v(\vec{x},t)$ for the mixed phase is calculated by solving Navier-Stokes Equation s. $\vec{x}$ is the position in space, and t is time. The particle velocity field ($v_p(\vec{x},t)$) can be evaluated based on the mixed phase velocity field $v(\vec{x},t)$ and the spatial settling velocity v_{Bulk}. This reduces the solution time compared to the classical Eulerian method. In this regard, a temporary spatial viscosity ($\eta_{MP}(\vec{x},t)$) was used in order to consider the different behaviors of the mixed phase:

$$\eta_{MP}(\vec{x},t) = A \cdot \eta_{Susp}(\vec{x},t) + B \cdot \eta_{Sed}(\vec{x},t) \tag{2}$$

In the above Equation , $\eta_{MP}(\vec{x},t)$ is calculated based on the viscosity of the mixture ($\eta_{Susp}(\vec{x},t)$) and virtual viscosity of the settling material ($\eta_{Sed}(\vec{x},t)$). A is the mixing coefficient and B is the sediment spatial coefficient. The values of A and B change between the values of 0 and 1 depending on the type of phase, depending on whether the phase is mixed or settled. Although coefficients have been used in this study to simplify the mixture analysis process and to investigate its behavior, the presented solution can be considered and even used to advance the goals of analysis and simulation.

In the present study, the analysis of the structure and dynamic performance of the two-stage pusher centrifuge device has been demonstrated. In this regard, the simulation task has been considered for the subsets of the inner basket, the outer basket, and the feeding chamber in three phases: modal analysis, particle behavior analysis, and transient state dynamics analysis. Finite element analysis results have been analyzed and compared with the experimental results.

2 METHODS

The 3-dimensional (3D) modelling and finite element analysis (FEA) procedure are explained here.

2.1. 3D Modelling

The intended set (“Fig. 1”) was designed as the inner basket subset, outer basket subset, rotating disc, and feeding shell according to Ferrum-P-32 model pusher centrifuge geometry.

“Table 1” lists the parts in the created design.

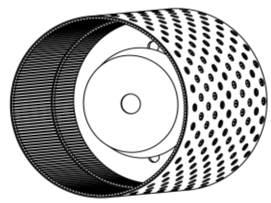

(a)

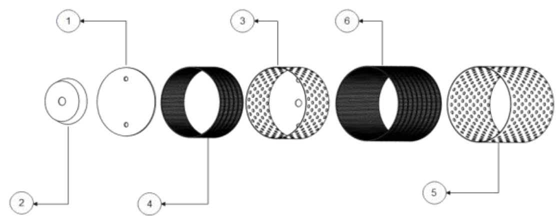

(b)

Fig. 1 3D model designed for finite element analysis; (a) Assembly; (b) Exploded view.

Table 1 List of parts of the 3D model designed

Number	Part Number	Type	Quantity
	SA-Basket-1	Assembly	1
	SA-Basket-2	Assembly	1
1	Rotating-Disk	Part	1
2	Cover	Part	1

Bill of Material: SA-Basket-1

Number	Part Number	Type	Quantity
3	Basket-1	Part	1
4	Wedge-Wire-1	Part	1

Bill of Material: SA-Basket-2

Number	Part Number	Type	Quantity
5	Basket-2	Part	1
6	Wedge-Wire-2	Part	1

2.2. Simulations

The desired dynamic analysis is done in two separate categories: modal analysis and transient dynamic analysis.

2.2.1. Modal Analysis

The preparatory steps including the boundary conditions and connections for the complete set and members can be defined as follows:

2.2.1.1. The Complete Set

Figure 2-a shows the model used to perform modal analysis for the entire configuration. In order to perform modal analysis in the software, boundary conditions, and connections were applied on the set and members according to “Fig 2-b”. The material used for the members was stainless AISI 304. The chemical composition of this steel is mentioned in “Table 2”and its important physical and mechanical properties are mentioned in “Table 3”.

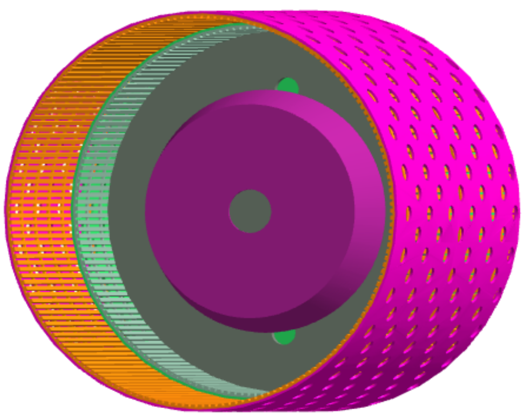

(a)

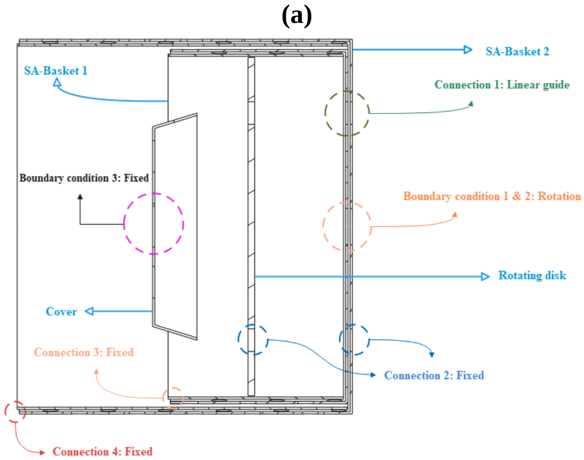

(b)

Fig. 2 Schematics of the model used for modal analysis: (a): 3D model of the assembly, and (b): The cut view of the model along with the display of connections and boundary conditions (The wedge-wires are depicted in a simple form for simplicity of the display.)

Table 6 Chemical composition of AISI 304 steel used for components

Element	**Percent**		
C	0	-	0.08
Cr	18	-	20
Fe	65.8	-	74
Mn	0	-	2
Ni	8	-	11
P	0	-	0.045
S	0	-	0.03
Si	0	-	1

Table 3 Physical and mechanical properties defined for the components

Parameter	Value
Density ($\frac{kg}{m^3}$)	7960
Elasticity modulus (MPa)	197
Yield strength (MPa)	258
Tensile strength (MPa)	565
Poison ratio	0.27
Hardness (HB)	175
Fatigue strength at 10^7 cycle (MPa)	241

2.2.1.2. The Inner Basket Sub-Set

The imported model of the inner basket sub-set (including wedge-wire and basket) can be seen in “Fig. 3”. This sub-set has also been subjected to modal analysis separately.

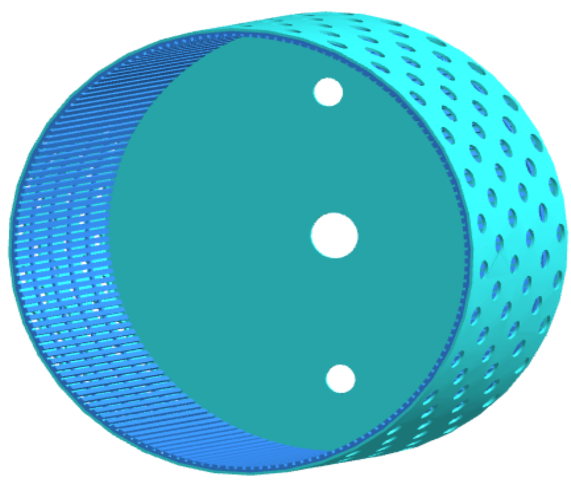

Fig. 32 Inner basket subset model.

2.2.2. Dynamic Behavior Analysis

Different available methods have been evaluated initially to choose the appropriate one in terms of practicality and precision. Since the input and output materials of the machine are both in the form of granular materials (powder), the following can be mentioned as different approaches to perform such an analysis:

- Flexible dynamic along with fluid dynamics analysis: this method is one of the most complex and time-consuming approaches that can be used here. Although in terms of assumptions, this method is closer to reality, the flexible dynamics of the desired member due to the relatively complex geometry of the wedge-wire, make it almost impossible to solve. In addition, the simultaneous calculation of fluids to investigate the behavior of salt powder would be another difficulty during the task.

- Flexible dynamic and fluid dynamics analysis separately: in this method, simulation is performed once in the form of rigid body dynamics to check the dynamic behavior of particles. This way, the number of contacts, pressure distribution, and the effect of random load caused by particles on the target member are obtained. Therefore, it is possible to extract the dynamic unbalanced load behavior caused by the particles and use it to find the load function of these particles on the desired member. Nevertheless, it should be noted that this loading function is dependent on the time and position inside the member. It is also necessary to mention that the duration of stability of particle behavior is obtained in fluid dynamics analysis. In other words, since the member starts moving from the stationary state until it reaches a constant speed, it will not be a definitive criterion for the stability of the behavior of this function; Rather, the duration of stability of the load behavior should be obtained according to the dynamic analysis and the particle outlet rate.
- Flexible dynamic and and discrete dynamic analysis of particles separately: this approach is the same as the previous approach, with the difference that the discrete method has been used to simulate powder and independent particles. Although this method is more compatible with the target problem, the solution of both methods will be relatively the same.
- Using the third method, the intended steps could be summarized as follows:

  - Discrete element simulation of particles
  - Extracting the loading function (stress distribution)
  - Transient state dynamics analysis
  - Extraction of mechanical parameters including distribution of stress and strain on the desired member

2.2.2.1. Discrete Elements Analysis of Particles

In order to simulate the dynamic behavior of powder particles, EDEM Rocky software was used as a discrete element analysis simulation tool. The steps are briefly described below:

- 3D Model

Figure 4 demonstrates the imported set to simulate the behavior of particles in the software.

- Feeding chamber

In order to simplify the solution and the possibility of repeating the simulation and modification, the complexities in the geometry of some components such as bolts and nuts are omitted and some components such as the guide bushings and coupling are not included in the model. Nevertheless, the function of these components is defined in the model. The inlet port of the feeder is defined with a diameter equal to the diameter of the shell of the feeder section according to “Fig. 5”.

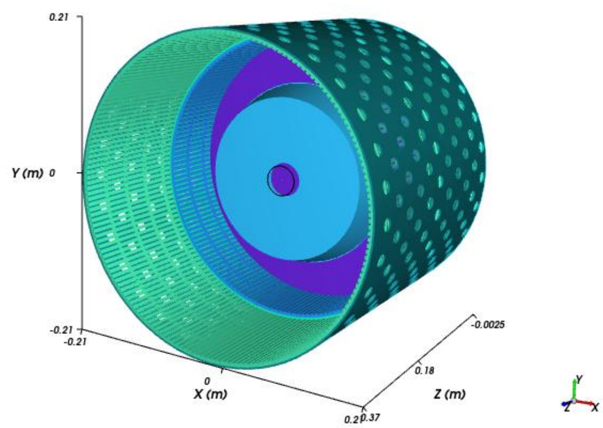

Fig. 4 The entire model used in the simulation software to check the behavior of particles.

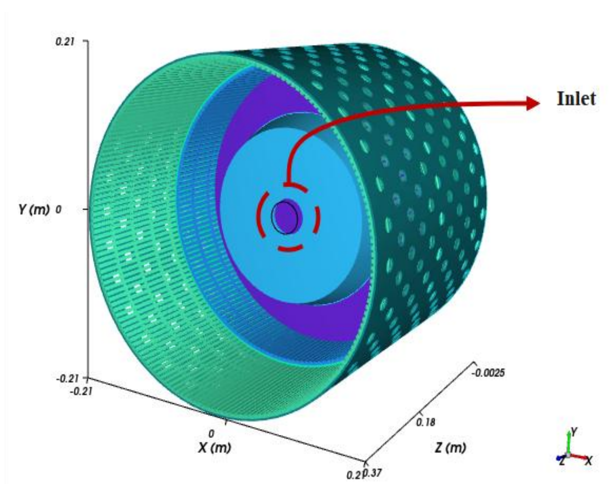

Fig. 5 Feeding inlet port in the model

Table 4 demonstrates the specifications applied in the software for feeding inlet. It should be noted that the concentration of particles in the water fluid is 18% and the feeding beginning time is considered to be at 8 s.

- Movements definitions

The required rotational and oscillating motions were applied to the disk, the inner basket subset, and the outer basket subset according to the values obtained from the actual operation of the device [6], [12]. Table 5 provides the applied values.

Table 7 Specifications of the fed particles inside the chamber for simulation

Parameter	Particle mass (kg)	Particle volume (m^3)	Particle density ($\frac{kg}{m^3}$)	Particles inlet mass flow rate ($\frac{kg}{s}$)	Particles inlet volume flow rate ($\frac{m^3}{s}$)
Value	424×10^{-6}	1.96×10^{-7}	2163	0.56	2.6×10^{-4}

Table 8 The values of the kinematic parameters applied for the components of the simulation

Part (subset)	Rotational speed ($\frac{rad}{s}$)	Reciprocation frequency (Hz)	Amplitude (m)
Rotating disk	36.65	0	0
Feeding shell	0	0	0
Inner basket subset	36.65	0.5	0.025
Outer basket subset	36.65	0	0

- Particle sedimentation rate

In order to take into account the particle sedimentation caused by centrifugal force in the fluid, the results of Reynold and Sokolov experiments [6] were used to investigate the behavior of particles during the simulation process and convert them into filtered mass (cake). According to the results of these experiments, the sedimentation speed (u) can be expressed as follows in the radius r of a turbulent area in terms of $\frac{m^3}{s}$:

$$u(r) = 1.75\,\eta_1 \left[\frac{d\omega^2 r(\rho_s - \rho_l)}{\rho_l}\right]^{0.5} \quad (3)$$

Where:

$$\eta_1 = (1 - x_s)^{5.5} \quad (4)$$

Where η_1 is the settling speed correction factor, x_s is the ratio of solid (powder) to mixture, d is the average diameter of the particles, ρ_l is the density of the liquid, ρ_s is the density of the solid (powder), and ω is the angular velocity of the liquid in radius r. The speed (ω) can be calculated using the following Equation [6]:

$$\omega(r) = \omega_0 \left[1 - \left(\beta \times \frac{Q}{\nu^{0.5} \cdot r_1}\right) \cdot \frac{\left(\frac{r_2}{r}\right)^2 - 1}{\left(\frac{r_2}{r_1}\right)^2 - 1}\right] \quad (5)$$

Where ω_0 is the angular velocity of the basket, r_1 is the radius of the free surface, r_2 is the radius of the basket wall (wedge-wire), Q is the inlet flow rate of the fluid mixture and powder, ν is the kinematic viscosity of the liquid, and $\beta = 2.6 \times 10^{-7} \frac{\sqrt{s}}{m}$. α is a constant coefficient assumed due to the nature of the fluid and algebraic simplifications of the Equation. The considered values for "Eq. (3) to (5)" are mentioned in "Table 6".

Table 9 The values considered for the "Eq. (3) to (5)**"** calculate the sedimentation rate of parties

Parameter	d (m)	$\rho_s \left(\frac{kg}{m^3}\right)$	$\rho_l \left(\frac{kg}{m^3}\right)$	x_s	$\omega_0 \left(\frac{rad}{s}\right)$	r_1 (m)	r_2 (m)	$\nu \left(\frac{m^2}{s}\right)$	$Q \left(\frac{m^3}{s}\right)$
Value	0.0072	2163	1000	0.2	36.65	0.18	0.1925	10^{-6}	0.002513

Figure 6 demonstrates the sedimentation rate of the particles ($u(r)$) inside the inner basket in versus radius (r). Also, according to the "Eq. (3)", the speed rates for the radius of the free surface (r_1) and maximum value (r_2) are obtained as $u(r_1) = 0.73\,\frac{m}{s}$ and $u(r_2) = 0.755\,\frac{m}{s}$, which indicates the small variation of this parameter along the radius. Therefore, the obtained changes and the sedimentation rate of the particles have a slight effect on the loading fluctuations and the imbalance of its behavior during the process. Therefore, it can be ignored with negligible error in calculations.

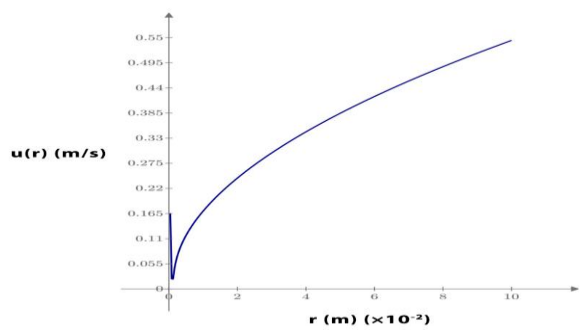

Fig. 6 Particle sedimentation rate ($\boldsymbol{u(r)}$) inside the inner basket (wedge-wire) versus radius ($\boldsymbol{r}$).

- Stress-time function

Contact spots are demonstrated 5 seconds after the beginning of the simulation (at the middle of the simulation durations) in the front view in “Fig. 7”. Although the contact points are not constant during the simulation process, it is important to check the critical points to obtain the appropriate variable stress distribution in the next stages of the simulation. Thus, in order to obtain the time-varying loading function, the regions A to D have been defined according to “Fig. 8” to retrieve average stress-time data in these regions. Figure 9 demonstrates the vertical stress variation diagram applied to region A as an example. As the diagram shows, the changes in load value have occurred in a certain range (between 0 and 5000 Pa).

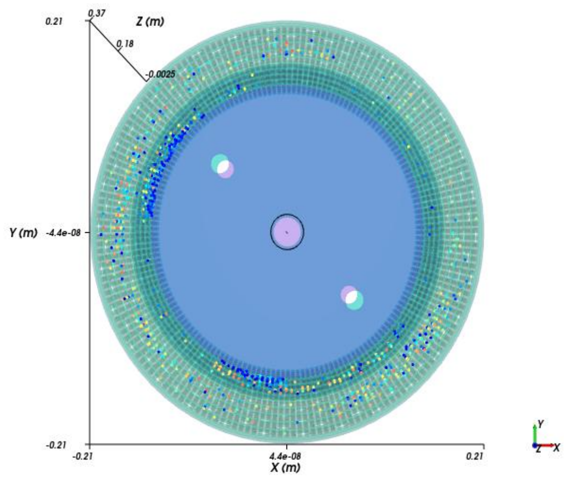

Fig. 7 The contact points of the particles and the inner basket at the middle of the simulation duration in colored dots in the front view. (For simplicity in the display, the feeding shell is hidden.)

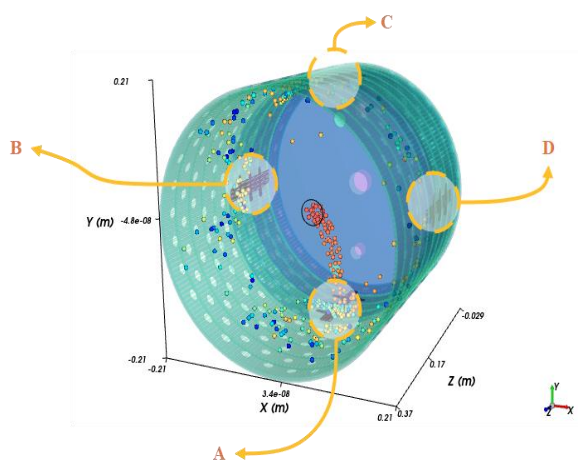

Fig. 8 Checkpoints defined to extract the average stress distribution diagram versus time (for simplicity in the display, the shell of the feeding section is hidden.)

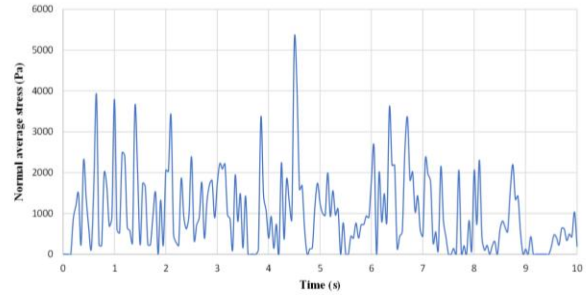

Fig. 9 An example of the average stress distribution diagram extracted in region A.

The values obtained from ranges A to D have been transformed to the stress-time table and have been indirectly applied as a coefficient of the time-dependent stress function on the inner surface of the inner basket in order to analyze the dynamic behavior in the transient state. To do this, the following steps were taken:

○ Obtaining stress distribution values of each region

First, the stress distribution values of all 4 regions were obtained according to “Fig. 10” during the simulation.

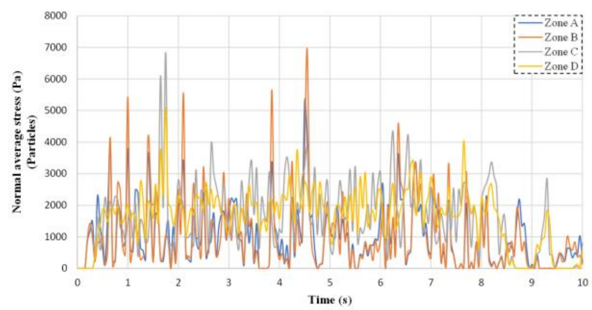

Fig. 10 Stress variations of regions A to D within the inner basket.

○ Calculation of normalized values

At this step, the normalized function of the average value was obtained in the range between 0 and 1, taking into account the maximum and minimum values according to “Fig. 11”.

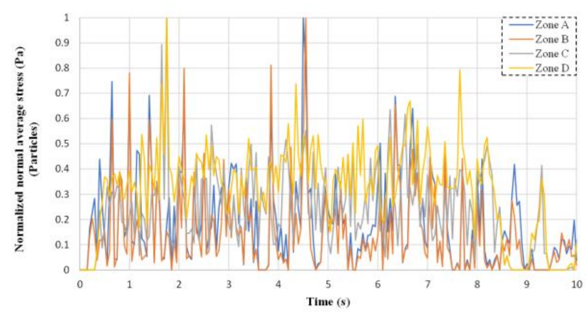

Fig. 11 Normalized values of the average stress variations in regions A to D within the inner basket.

○ Calculation of the mixture loading function

Since the powder particles are fed as a mixture with the liquid inside the assembly, the final pressure distribution will be a combination of the pressure caused by the liquid and the particles. Therefore, the final stress distribution is considered as the product of the normalized values of the stress caused by the particles in the hydraulic pressure of the centrifuge. The hydraulic pressure caused by the fluid on the basket wall can be calculated via the following Equation [13].

$$p_c = \rho\omega^2 \int_{r_1}^{R} r dr = \frac{1}{2}\rho\omega^2 (R^2 - r_1^2) \quad (6)$$

Where p_c is the hydraulic pressure of the centrifuge, ρ is the density of the fluid, ω is the rotational speed of the basket, r is the radius, R is the radius of the basket, and r_1 is the radius of the free surface of the fluid. The considered values for these parameters are mentioned in “Table 7”.

Table 10 The values considered for Equation (6) to calculate the stress (pressure) caused by the mixture

Parameter	$\rho\ \left(\frac{\text{kg}}{\text{m}^3}\right)$	$\omega\ \left(\frac{\text{rad}}{\text{s}}\right)$	R (m)	r_1 (m)
Value	1000	36.65	0.1925	0.18

Therefore, the distribution of stress (pressure) caused by the mixture of fluid and particles is assumed as “Fig. 12” in the transient dynamics analysis section.

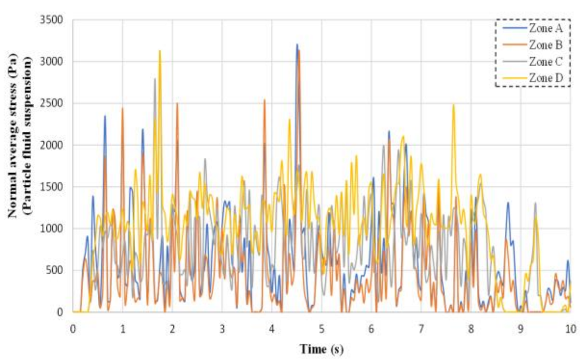

Fig. 12 The stress value versus time caused by the mixture of fluid and particles to be applied inside the inner basket subset to analyze the dynamic behavior in the transient state.

Since the diagram obtained in “Fig. 12” assumes a uniform pressure distribution in the internal space at any time, the imbalance in loading at different angle positions is not taken into account. Therefore, it is necessary to consider this imbalance somehow in the loading of different regions. In fact, the amount of load difference between the regions should be included in the values. In order to achieve this goal, the normalized value of the load distribution of each region in the diagram of “Fig. 12” has been multiplied and its product is considered as the time function required to be applied in the dynamic analysis of the transient state. In addition, in order to increase the accuracy of the analysis in the phase of transient dynamics analysis, the medial regions between the 4 initial regions have been considered and their values have been calculated by interpolating. Figure 13 shows the final arrangement of areas A to D and intermediate areas. Figure 14 exhibits the calculated final stress distribution values for the intermediate areas AB to DA.

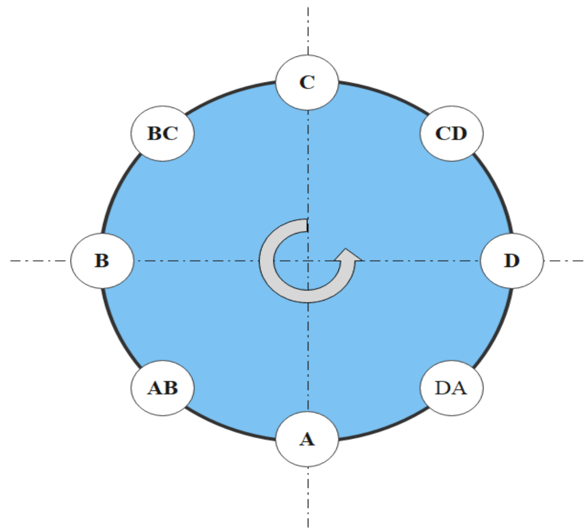

Fig. 13 The location of the regions A to D and intermediate regions (AB to DA) in the inner basket.

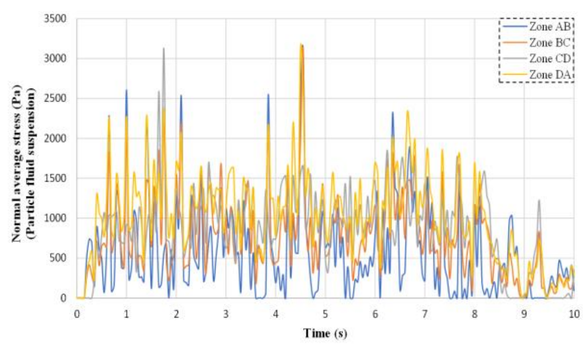

Fig. 14 Calculated values of fluid and particle mixture stress for the intermediate regions AB to DA.

2.2.2.2. Transient Dynamic Analysis

The model used to simulate the transient dynamic behavior is shown in “Fig. 2-a”. The boundary conditions and connections have been similar to those mentioned in the modal analysis section (“Fig. 2b”). The kinematic and dynamic parameters are defined according to “Table 5”. In order to apply the dynamic stress distribution obtained from the particle behavior analysis section, time-stress distribution functions were defined in the form of tabular functions in the regions A to D. Figures 15 & 16 show how these loads are set for area A. The aforementioned variable loading was defined for other regions AB to DA in a similar way.

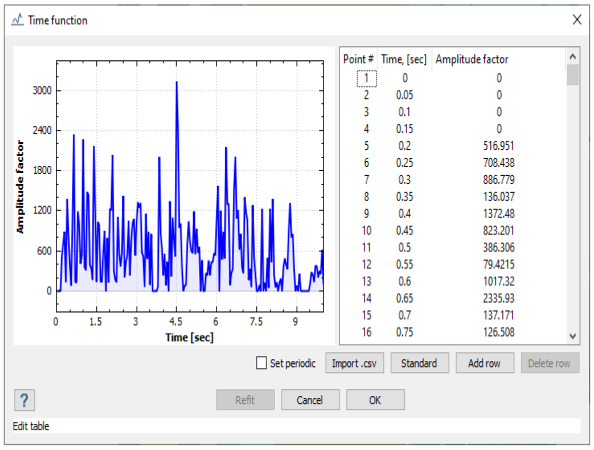

Fig. 15 The definition of the time-stress function extracted from the particle analysis section to analyze the dynamic behavior of the transient state.

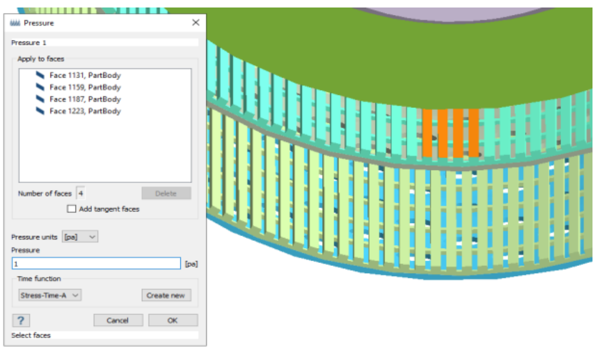

Fig. 16 Applying the time-stress function from the particle analysis section on region A to analyze the dynamic behavior of the transient state.

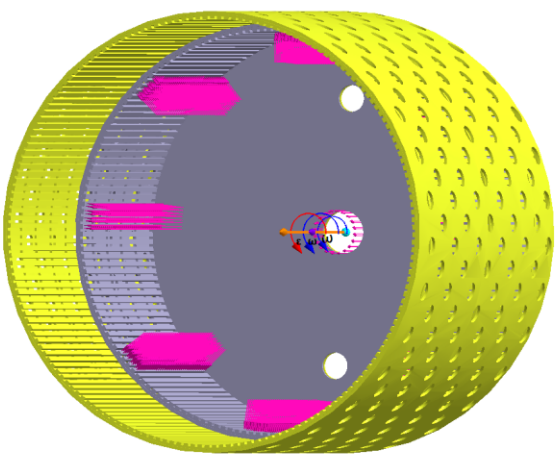

Fig. 17 The assembly with the predefined loading and reciprocating movement of the internal subset (The feeding chamber is hidden).

In order to define the rotation and the resulting inertia on the set with the desired angular velocity ("Table 5"), the angular velocity was defined for the whole set. Also, in order to define the reciprocating motion of the internal basket subset with the desired frequency ("Table 5"), an alternating sinusoidal motion on the internal basket subset was applied. Figure 17 shows the prepared assembly with applied loads and motions.

3 RESULTS AND DISCUSSION

The experimental validation of the results was assured about in range of force values and relative displacement according to previous studies conducted in this field [14-17]. According to the values obtained in these studies, the average value of the force measured due to the contact of particles with the inner surfaces of the basket differed by about 9%. Also, the difference in the average value of the relative displacement obtained in the practical test was about 4% compared to the obtained results here. The reasons for this scatter between experimental and simulation values can be related to factors such as simplifying assumptions applied in the geometry, measurement accuracy in dynamometers and strain gauges, and simplifying assumptions considered in the simulation.

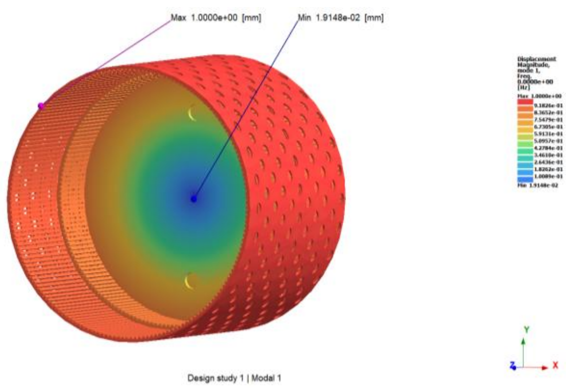

Fig. 18 The result obtained from the modal analysis performed on the assembly in mode 1 in the form of the color contour of the relative maximum displacement

3.1. Modal Analysis

The results obtained in this section include the relative displacements caused in the parts and the calculation of their natural frequency. In order to interpret the results of the modal analysis, the natural frequencies of the set and the subset of the inner basket have been compared with the normal working vibration frequency of the device. Then the resonance phenomenon for the critical mode has been investigated. The critical mode was assumed as the mode in which the maximum displacement occurred. Also, a comparison has been made between the natural frequency of the set and the subset of the internal basket. Figure 18 shows the maximum relative displacement in the first mode of the modal analysis. The results obtained for all modes are summarized in "Fig. 19". The natural frequency values for "Fig. 19" are mentioned in "Table 8".

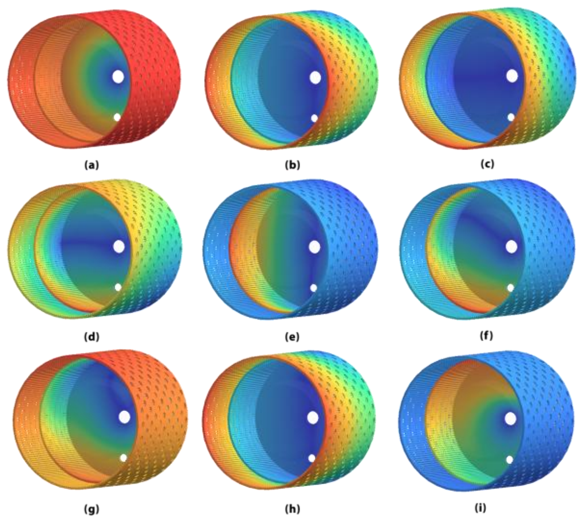

Fig. 19 The results of the modal analysis performed on the set in the form of a colored contour of the relative maximum displacement: (a): mode 1, (b): mode 2, (c): mode 3, (d): mode 4, (e): mode 5, (f): mode 6, (g): mode 7, (h): mode 8, and (i): mode 9, (The range of changes from the minimum (blue) to the maximum (red) is the same for all of the items).

Table 11 Natural frequency values in the investigated modes of the set

Mode No.	Natural frequency (Hz)	Mode No.	Natural frequency (Hz)
1	0.00	6	23.49
2	8.15	7	27.76
3	9.42	8	29.61
4	20.60	9	42.11
5	21.59		

According to the rotational speed of the device based on "Table 5" ($36.65\frac{\text{rad}}{\text{s}}$), it can be concluded that the normal working vibration frequency of the device is 5.83 Hz. According to the results found in "Fig. 19" and "Table 8", the natural frequencies of the modes are different from the normal working vibration frequency of the device. Thus, the probability of the resonance phenomenon is negligible for the set.

The relatively small difference between the vibration frequency of the device and the natural frequency in the second vibration mode ("Fig. 19-b") with a value of 8.15 Hz according to "Table 8" is not much of important, however, it should be considered while using the device. Regarding the resonant frequency of the inner basket subset, the matter seems a little different. Although, the extent of the displacement in the first mode is relatively high according to "Fig. 20-a", mode 4 ("Fig. 20-d") is more important here. As can be seen in this mode, the relative displacement has an almost large value compared to the other modes, which can represent the resonance in this mode. However, by comparing the natural frequency value of this mode and the normal working frequency range of the device (5.83 Hz), it is determined that the possibility of resonance is negligible according to the calculations.

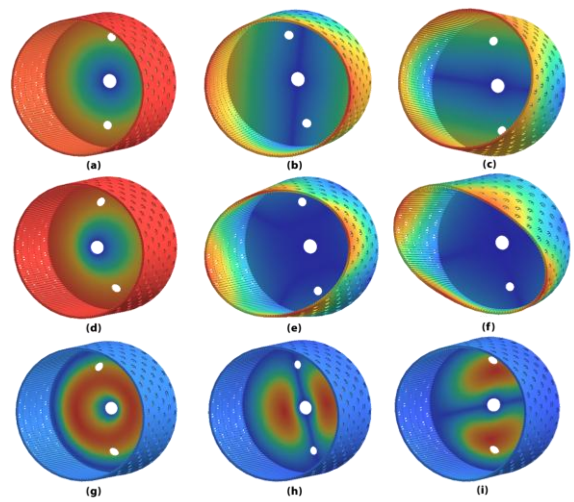

Fig. 20 The results of the modal analysis performed on the inner basket subset in the form of a colored contour of the relative maximum displacement: (a): mode 1, (b): mode 2, (c): mode 3, (d): mode 4, (e): mode 5, (f): mode 6, (g): mode 7, (h): mode 8, and (i): mode 9, (The range of changes from the minimum (blue) to the maximum (red) is the same for all of the items).

In overall, it should be stated that none of the calculated modes is equal to the working vibration frequency of the device. Although according to "Table 8", the value of the natural frequency obtained for mode 2 of the set has less difference than other values, since this value (8.15 Hz) is higher than the operating frequency of the device (5.83 Hz), reaching this value practically does not happen. Therefore, the margin of safety resulting from this comparison can be estimated at 40% after comparing the values in "Table 8" to the working conditions.

Table 12 Natural frequencies in the investigated modes of the inner basket subset

Mode No.	Natural frequency (Hz)	Mode No.	Natural frequency (Hz)
1	0.01	6	178.35
2	12.80	7	394.29
3	13.06	8	425.07
4	32.11	9	433.89
5	177.61		

By direct comparison of the natural frequency values in “Tables 8 & 9”, it turned out that the lowest difference value (2.5 Hz) belonged to mode 8 of the set and mode 4 of the inner basket subset. The more important point is the small difference (3.64 Hz) between the natural frequency values of mode 3 for the desired set and the subset. A similar result can be seen for mode 2 as well. According to “Fig. 20-c”, this vibration mode corresponds to displacement around a horizontal axis in the floor plane. Since such displacement and movement cannot be obtained directly by the normal operation of the device, it can be concluded that such vibration is far from expected.

3.2. Dynamic Behavior

The stress distribution and displacement results have been specifically discussed here. It should be noted that displacement in transient state dynamic analysis has been about the differential displacement, while kinematic displacement and motion analysis have not been directly analyzed here.

3.2.2. Particles

The contact points that occurred in the middle of the simulation process can be viewed in “Figs. 7 & 8” on the inner basket subset. Since the duration of feeding is considered from the beginning of the simulation to 8 s, the stress values obtained after the end of feeding duration have decreased according to data in “Fig. 10”. The reason was the gradual exit of the particles in the inner basket. As “Fig. 9” shows, the usual range of stress values was between 0 and 4000 Pa. Considering the area of the target section in regions A to D (0.004 m^2), the average force applied in these areas can be estimated between 0 and 16 N. The reason for the variations observed in this diagram (“Fig. 9”) is the consecutive and random contacts of the particles with the target region, which caused fluctuations in the obtained value. The data obtained from this section proves that the analyzed set has the required mechanical strength against the dynamic stress caused by the particles.

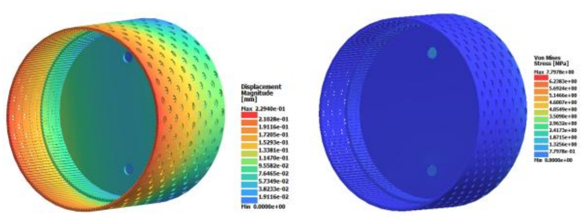

(a) (b)

Fig. 21 The displacements along with deformations: (a): and stress distribution, and (b): on the assembly in a critical state in the form of colored contours during the simulated process to check the dynamic behavior in transient state.

3.2.3. Transient State Dynamics

Figure 21 shows the results of the transient state dynamic analysis for the set. For simplicity in the display, the feeding section is hidden. According to “Fig. 21-a”, the amount of displacement that occurred in the set is higher for peripheral and endpoints. In other words, the amount of displacement has increased by moving far from the engaged points which is natural. As can be seen in “Fig. 21-b”, the amount of stress distribution caused in the subset of the external basket can be ignored, and what should be investigated more is the subset of the inner basket. Figure 22 shows the results of transient state dynamic analysis for the inner basket subset.

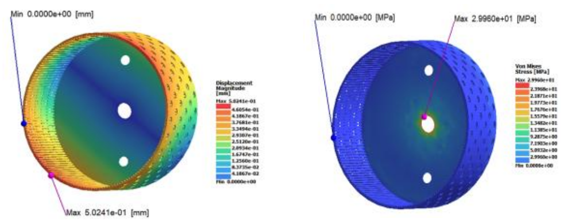

(a) (b)

Fig. 22 The displacements along with deformations: (a): and stress distribution, (b): on the inner basket subset in a critical state in the form of colored contours during the simulated process to check the dynamic behavior in transient state.

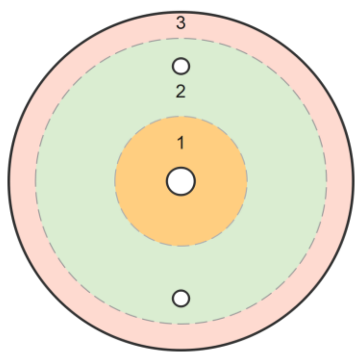

Fig. 23 Zoning of the bottom plate of the basket according to the significance of stress distribution.

As can be seen in the displacement distribution contour (“Fig 22-a”), the displacement is more in the peripheral and surrounding points than in the central and hole parts, although its amount is small and can be ignored. The distribution of the displacement that occurred on the bottom plane of the basket has also changed in layers. In other words, these changes have not been radial or circular. The same has been observed in a more regular way for the stress distribution (“Fig. 22-b”). In other words, the stress values around the central hole are the maximum, and the minimum values are at the peripheral points.

Also, on the bottom plane of the basket, the stress values in the outer ring are slightly higher than the inner ring. Regarding the stress distribution of the guiding rod holes, no special difference has been observed compared to the inner ring. Therefore, the stress distribution on the basket floor can be schematically divided into zones as displayed in “Fig. 23” in terms of importance.

Figure 24 shows the displacements in one of the peripheral points with critical conditions. The changes have occurred in short intervals and its high fluctuations are related to the lower values according to the diagram in “Fig. 24”.

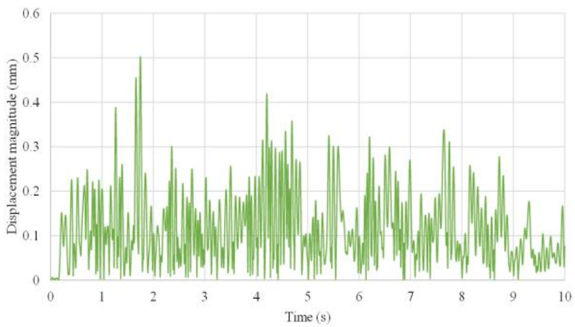

Fig. 24 Displacement variations during the simulation process on the critical point of the inner basket subset.

The graph also demonstrates the decreasing trend of the maximum values, which means the stabilization of its dynamic behavior after a certain period of time. The significant changes of the peaks have been relatively reduced after a period of 5 s and it can be said that the stability of the behavior is observed from this time onwards. Nevertheless, it should be noted that the reduction observed from the time interval of 9 s to the end is due to the interruption of the particles feeding at the time of 8 s, and it cannot be directly caused by variations in dynamic behavior and stability. A similar trend can be seen in the other way in “Fig. 25” regarding the changes of the stress value for the critical point in “Fig. 22-b”.

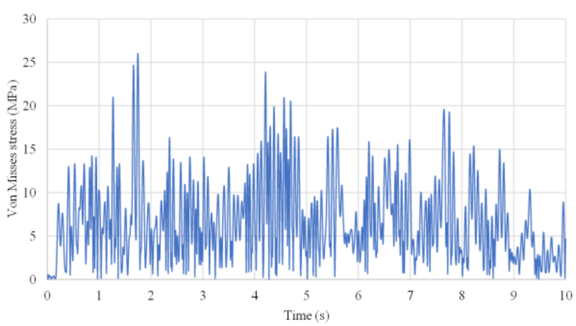

Fig. 25 Stress variations during the simulation process on the critical point of the inner basket subset.

Again, in this graph, the relative stability can be observed after 8 s. Therefore, the duration of stability of particle behavior is about 5.5 s or 68% of the particle inlet time period. The maximum von Mises equivalent stress value has been below 20 MPa. Although this value is not significant from the mechanical point of view, it is useful for examining the dynamic behavior. Overall, the maximum displacement at the critical point of the inner basket subset has been 0.51 mm and the critical stress imposed on it is about 27 MPa according to the results. As a result, the mechanical strength of the assembly versus the stresses and strains caused by the operation of the device can be acceptable.

4 CONCLUSIONS

In this study, the structure and dynamic performance of the two-stage pusher centrifuge were analyzed. In this regard, the simulation process was done in three phases: modal analysis, particle behavior analysis, and transient state dynamics analysis. The results of the modal analysis showed that the safety margin obtained in the context of the occurrence of the resonance phenomenon due to the normal working vibration frequency of the device and the natural frequency of the assembly due to the change in the trend of linear and rotational inertial forces was 40%. In addition, based on the results of the transient dynamics analysis, the stability of the particle behavior was about 5.5 s or 68% of the particle feeding time, the maximum displacement at the critical point of the inner basket subset was 0.51 mm, and the critical stress on it was about 27 MPa; which means the acceptable mechanical strength of the assembly versus the stresses and strains caused by the operation of the device. What can be inferred based on the results of the analysis was the recommendation to maintain the maximum rotational motion ($36.68\frac{rad}{s}$) and no significant change in the particle feeding rate compared to the specified value ($0.56\frac{kg}{s}$). The following are also inferred according to the results:

- According to the modal analysis, the current rotating speed of the device would not lead to destructive or intensified vibrations.
- According to the modal analysis, the natural frequency of the desired set and the inner basket would not cause vibration problems in different modes.
- According to the transient state dynamic behavior analysis performed on the inner basket subset, the importance of stress distribution on the floor plane in the center has been identified as the most important and the least important was found to be in the middle ring.

- The range of displacements observed in the dynamic analysis of the transient state showed that the displacements around the assembly were in the range of small values and would not be problematic.
- Although the range of stress values and the resulting displacements is not considerable mechanically, increasing the feed rate, considering the linear and rotational inertial forces created, might lead to a change in the working vibration frequency of the device. Therefore, the possibility of resonance increases due to the differences obtained with the set and subset. Thus, it is suggested to increase the particle feed rate with caution and even after the experimental test if possible.
- Considering the required mechanical strength range, the use of lighter and even less strong materials could be appropriate for improving the performance of the device; Not only does it facilitate the process of fabrication and assembling the device, but also the inertial forces caused by the mass of the members and the tendency to run away from the center and damage to the bearings will be reduced.

REFERENCES

[1] Ergun, S., Orning, A. A., Fluid Flow through Randomly Packed Columns and Fluidized Beds. Industrial & Engineering Chemistry, Vol. 41, No. 6, 1949, pp. 1179-1184.

[2] Leung, W. W. F., Industrial Centrifugation Technology, McGraw-Hill Education, 1998.

[3] Romani Fernández, X., Nirschl, H., Multiphase CFD Simulation of a Solid Bowl Centrifuge. Chemical Engineering & Technology, Vol. 32, 2009, pp. 719-725.

[4] Stahl, S., Spelter, L. E., and Nirschl, H., Investigations on the Separation Efficiency of Tubular Bowl Centrifuges. Chemical Engineering & Technology, Vol. 31, No. 11, 2008, pp. 1577-1583.

[5] Ambler, C. M., The Theory of Scaling Up Laboratory Data for The Sedimentation Type Centrifuge, Journal of Biochemical and Microbiological Technology and Engineering, Vol. 1, No. 2, 1959, pp. 185-205.

[6] Pang, C., et al., Simulating Multiphase Flow in a Two-Stage Pusher Centrifuge Using Computational Fluid Dynamics, Frontiers of Chemical Science and Engineering, Vol. 6, No. 3, 2012, pp. 329-338.

[7] Bürger, R., F. Concha, Settling Velocities of Particulate Systems: 12, International Journal of Mineral Processing, Int J Miner Process, Vol. 63, 2001, pp. 115-145.

[8] Yan, F., Farouk, B., Numerical Simulations of Flows Inside a Partially Filled Centrifuge, Journal of Fluids Engineering, Vol. 125, 2003, pp. 1033.

[9] Anlauf, H., Recent Developments in Centrifuge Technology, Separation and Purification Technology,Vol. 58, No. 2, 2007, pp. 242-246.

[10] Wang, Y., et al., CFD Simulations of Membrane Filtration Zone in A Submerged Hollow Fibre Membrane Bioreactor Using a Porous Media Approach, Journal of Membrane Science, Vol. 363, No. 1, 2010, pp. 57-66.

[11] Ferry, J., Balachandar, S., A Fast Eulerian Method for Disperse Two-Phase Flow, International Journal of Multiphase Flow, Vol. 27, 2001, pp. 1199-1226.

[12] Nwogu, C., Design and Development of an Industrial Centrifuge for Small and Medium Scaled Industries, Innovative Systems Design and Engineering, 2015, pp. 6.

[13] Brouwers, J. J. H., Innovative Methods of Centrifugal Separation. Separations, Vol. 10, No. 3, 2023, pp. 181.

[14] Anlauf, H., Sorrentino, J. A., The Influence of Particle Collective Characteristics on Cake Filtration Results, Chemical Engineering & Technology, Vol. 27, No. 10, 2004, pp. 1080-1084.

[15] Bentz, M., Hartmetz, O., and W., Stahl, Particle Destruction Effects in Pusher Centrifuges during Solids-Liquid Separation, Chemical Engineering & Technology, Vol. 27, No. 10, 2004, pp. 1075-1080.

[16] Deshmukh, S., Joshi, J., Flow Visualization and Three-Dimensional CFD Simulation of the Annular Region of an Annular Centrifugal Extractor, Industrial & Engineering Chemistry Research - IND Eng Chem Res, 2007, pp. 47.

[17] Leung, W. W. F., Shapiro, A. H., Improved Design of Conical Accelerators for Decanter and Pusher Centrifuges, Filtration & Separation, Vol. 33, No. 8, 1996, pp. 735-738.

Int. J. Advanced Design and Manufacturing Technology, 2025, Vol. 18, No. 1, pp. 51-63

DOI: ***ISSN: 2252-0406*** ***https://admt.isfahan.iau.ir***

Transient Vibration Analysis of an Optimized FML Cylindrical Shell Based on Maximum Reliability

Alireza Pourmoayed *
Department of Mechanical Engineering,
University of Khatamul-Anbiya Air Defense, Iran
E-mail: a.pourmoayed@khadu.ac.ir
*Corresponding author

Keramat Malekzadeh Fard
Department of Structural Analysis and Simulation, Aerospace Research Institute, University of Malek Ashtar, Iran
E-mail: kmalekzadeh@mut.ac.ir

Ali Nazari
Department of Aerospace Engineering, Aerospace Research Institute, Iran
E-mail: nazariali23@yahoo.com

Received: 26 September 2024, Revised: 23 December 2024, Accepted: 1 January 2025

Abstract: The transient vibration analyses of optimised Fibre Metal Laminates Cylindrical shells were examined in this paper. One of the most innovative aspects of this study is identifying an applied trend for optimizing the FML cylindrical shell construction to achieve maximum reliability. The FML shell reliability is determined using the First Order Reliability Method (FORM) and the Hashin failure criteria. To achieve this objective, the Shell is constantly subjected to a static load, and the resulting tensions within the FML layers of the shell are measured. The maximum tension is determined using the Hashin method, and the stability of the shell is subsequently estimated. Next, the amounts of reliability are certified according to shell stability. To maximize the FML shell reliability, the sequence of the composite-metal layers and fibre orientation are often modified, and for each case, the sample reliability is calculated. The second section of this study examines the effect of the optimized structure of the FML shells on the acceleration and displacement of these shells under dynamic loading. The energy approach is used to obtain the Equations of motion, whereas the mode superposition method is employed for transient vibration analysis.

Keywords: Fiber Orientation, FML Shell, Layup, Reliability, Transient Vibration

Biographical notes: Ali Reza Pourmoayed is an Associate Professor of Aerospace Engineering at the University of Khatamul-Anbiya Air Defence, Iran. He received his PhD in Airspace Engineering from Malek-Ashtar University of Technology in 2017. **Keramat Malekzadeh Fard** received his PhD in Mechanical Engineering from the University of K. N. Toosi in 2005. He is currently a Professor at the Department of Aerospace Engineering, Malek-Ashtar University of Technology, Tehran, Iran. **Ali Nazari** received his PhD from Aerospace Research Institute in 2019.

Research paper

1 INTRODUCTION

In general, industrial structures are subjected to dynamic loads, which can lead to vibration, buckling, or fatigue. One of the more useful parts of many transportation vehicles is the composite shell. One of the primary issues with these shells is that they will be significantly deformed under dynamic loads, which results in a perceptible reduction in the strength of composite shells. One of the methods that decreases this negative effect of dynamic loads is using of fiber metal laminates which are briefly called FML.

Many researchers have been done on the Transient vibration of composite cylindrical shells, for example, Lee et al. [1] analyzed the dynamic response of simply supported-simply supported Cross-Ply laminated circular cylindrical shells under impulse loads based on first-order shear deformation theory. They did not consider the pre-stress effect in the governing Equations of motion. Lam and Loy [2] examined the effects of boundary conditions on a slender rotating cylindrical shell made of layers using Love's first approximation and the Galerkin method. Chen [3] investigated the transient dynamic response analysis of an orthotropic circular cylindrical shell under external hydrostatic pressure. The researchers employed conventional shell theory and took into account the boundary requirements of simply supported. Karagiozova et al. [4] conducted a study on the transient deformation process of FMLs subjected to localized blast loading. They used the finite element method to analyze the deformation mechanism caused by highly localized pressure pulses, which result in permanent deformations and damage observed in FML panels during experiments. They demonstrated that the reaction of the FML panels is highly responsive to changes in the spatial and temporal distribution of pressure resulting from the blast loading. The study conducted by Khalil et al. [5] examined the dynamic behaviour of pre-stressed Fibre Metal Laminate (FML) circular cylindrical shells under lateral pressure pulse loads. The shell's equilibrium Equations were derived using the First-Order Shear Deformation Theory (FSDT), while the strain-displacement relations were based on Love's first approximation theory. The Galerkin method was employed to solve the equilibrium Equations for buckling, free vibration, and forced vibration problems of the shell.

Malekzadeh et al. [6] examined the Transient Dynamic response of multilayer circular cylindrical shells made of hybrid composite materials when exposed to a lateral impulse force. The boundary conditions are assumed to be clamped on one end and free on the other end. Both isotropic (metal) and orthotropic (composite) layers are used simultaneously in the hybrid Lamination. First-order shear deformation theory (FSDT) and Love’s first approximation theory are utilized in the shell’s equilibrium Equations. Equilibrium Equations for free and forced vibration problems of the shell are solved using Galerkin method. Finally, the time response of displacement components of Fiber-Metal Laminate (FML) cylindrical shells is derived using the mode superposition method. The non-linear dynamic instability of laminated composite cylindrical shells subjected to periodic axial loads is analyzed by Darabi et al. [7]. Dynamic instability of thin laminated composite cylindrical shells subjected to harmonic axial loading is investigated based on nonlinear analysis. The Equations of motion are developed using Donnell’s shallow-shell theory and with von Karman-type nonlinearity. The nonlinear large deflection shallow-shell Equation of motions is solved by using Galerkin’s technique that leads to a system of nonlinear Mathieu–Hill Equations.

Also, some research has been done on the optimization of composite cylindrical shells. For example, Haichao et al. [8] investigated the Simultaneous Optimization of Stacking Sequences and Sizing with Two-Level Approximations and a Genetic Algorithm. A new optimization model is first established by involving both stacking sequence and sizing variables. Within a single procedure, the genetic algorithm is used to solve a first-level approximate problem which includes both types of variables, while a second-level approximate problem is addressed for the individual fitness calculations. Numeric applications are presented to demonstrate the efficacy of this optimization strategy. Sen et al. [9] presented a Design optimization procedure for fiber metal laminates based on fatigue crack initiation. The state-of-the-art design method is a solution-oriented analysis, where only selected lay-ups are assessed for satisfying the design criteria. They aim to develop a reversed design procedure where the lay-ups are obtained as design solutions. Therefore, a genetic algorithm procedure is developed to find the optimal lay-up satisfying the required fatigue life. Ali Haeri et al. [10] presented the efficient reliability of laminated composites using an advanced Kriging surrogate model. To demonstrate a computationally efficient and accurate approach to the reliability analysis of laminated composites, an advanced Kriging model is applied to approximate the mechanical model of the structure. To construct the surrogate model, the structural response is simulated through the finite element method based on the classic theory of laminates. Tsai–Wu criterion is adopted to define limit state function in reliability analysis. A high-quality surrogate is achieved using a probabilistic classification function together with a metric for refinement of the model.

Malakzadeh Fard and Pourmoayed investigated the dynamic instability problem of beams built of Functionally Graded Materials (FGM) [11]. For this objective, the first-order shear deformation (or

Timoshenko) beam theory is examined in conjunction with the effects of geometric nonlinearity. The governing Equations, as well as various forms of common boundary conditions, are obtained by analyzing the energy functions of the system and applying Hamilton's principle. Ma et al. [12] focused on the dynamic analysis of FMLs, considering both macromechanical and micromechanical scale features. Additionally, the optimization studies on Fibre Metal Laminates (FMLs) within the context of dynamic analysis were investigated. The analysis and optimization of fibre-metal laminate cylindrical shells subjected to transverse impact loads were examined by Azarafza and Davar [13]. In order to achieve this objective, the genetic algorithms method is implemented to optimize the combination of the objective functions, which include weight and transverse impact response, as well as two constraints, which include critical buckling loads and principal strains.

The transient dynamic analysis of grid-stiffened composite conical shells is reviewed by Zamani et al. [14]. The influence of many parameters on forced vibrations has been studied, including fiber angle, geometric ratios, type, and so on. Also, this study examined the consequences of using grid-stiffened structures to strengthen the conical shell. Davar et al. [15] conducted a study on the reaction of laminated composite cylinder shells to low-velocity impacts under coupled pre-loads. Their findings revealed that regardless of the kind of axial pre-load (tensile or compressive), changes in contact characteristics during impact are linearly proportional to temperature changes. In addition, the changes in radial pressure are almost linear when there is a tensile axial pre-load, but they are nonlinear when there is a compressive axial pre-load. Alibeigloo and Talebitooti [16] conducted the study. The study examines the transient response of a cylindrical panel made of Functionally Graded Material (FGM) that is simply supported. The panel is equipped with sensor and actuator piezoelectric layers and is exposed to an electric field and thermal shock. The investigation is conducted using generalized coupled thermoelasticity, which is based on the Lord-Shulman theory. The study investigates the influence of a constant relaxation temperature, applied voltage, and thermal shock on the thermoelastic response of a cylindrical panel made of Functionally Graded Material (FGM). The parametric investigation revealed that the presence of material inhomogeneity has considerable effects on the coupled thermoelastic response of the hybrid FGM cylindrical panel. Khalili et al. [17] conducted a novel study on the dynamic analysis of a continuous SMA hybrid composite beam. The study considered the instantaneous phase transformation and material nonlinearity effects at any given moment for every point along the beam. This research and such analysis are conducted for the first time. The results revealed the accuracy of the proposed model and the corresponding solution algorithm. Additionally, the presence of hysteresis behaviour in shape memory alloys (SMAs) causes a damped response in both SMA hybrid composite beams and complete SMA beams.

Pourmoayed et al. [18] examined the characteristics of free vibrations in a sandwich structure with viscoelastic piezoelectric composite face sheets reinforced by Functionally Graded Carbon Nanotubes (FG-CNTs). The study utilized a new and enhanced higher-order sandwich panel theory and considered simply supported boundary conditions. The study examined the influence of key elements, including the length-to-thickness ratio, volume percentages of fibers, core thickness, elastic foundation, temperature and humidity variations, magnetic field, viscosity, and voltage, on the free vibration response of a sandwich structure. Fu and Hu [19] investigated the transient response of fibre metal laminated (FML) shallow spherical shells with interfacial damage under the influence of an unstable temperature field. The current model offers a highly efficient approach for conducting nonlinear dynamic analysis on composite laminated structures that have interfacial degradation and are exposed to transient temperature fields. The shell's displacements and stresses increase over time and remain constant when the temperature is at a constant level.

The current study is the first to optimize the structure of FML cylindrical shells, intending to achieve maximum reliability, by modifying the sequence of composite–metal layers and fibre orientation. The effectiveness of optimizing the FML structure on the dynamic response of FML shells is also being researched. The energy approach is employed for establishing the Equation of motion, whereas the mode superposition method is utilized for dynamic analysis. The Galerkin method is employed to solve the equilibrium Equations for transient vibration problems of the shell.

2 THEORY AND FORMULATION

2.1. Basic Assumptions

In this study to decrease negative effects of dynamic loads on the strength of the FML shell, an applied designing process is used for optimization of the FML shell’s structure based on maximum reliability. In the second part of this study, transient vibration of the FML shell structures which have the maximum and minimum reliability have been studied and acceleration and displacement of these structures due to applied dynamic load have been considered in all directions. Finally, the effect of optimized structure of the FML shells on the acceleration and displacement of these shells are investigated. The significance of this study lies in the fact that electronic equipment can be installed on the shells of certain transportation vehicles. However, many of these electronic components are susceptible to acceleration resulting from high-frequency dynamic loads. Therefore, it is important to determine the acceleration and displacement of these shells caused by dynamic loads. Using the determined maximum acceleration in each direction, it is possible to use electronic equipment capable of withstanding these accelerations.

The applied dynamic load refers to a high-frequency sinusoidal load that is applied over a short duration. To optimize the FML cylindrical shell structure to reach maximum reliability, the sequence of the composite-metal layers and the composite layer orientation of the FML shell are regularly changed. Each sample is subjected to a consistent static load, and the resulting tension stresses in the FML shell layers are measured to determine the maximum tension stress. The stability of all the FML shell samples is determined by applying Hashin's failure criteria and considering the ultimate strength of the FML layer's material. After determining the stability of all samples, the first-order reliability method is used to determine the reliability of the system. At last, an optimum structure with maximum reliability will be chosen for the FML shell. In order to perform the explained process, a prepared MATLAB program was linked to the finite element ABAQUS software. Various shells with different layer sequences and fibre orientations are generated and analyzed during the optimization process. This comprehensive program is able to analyze the FML shells with various arrangements of composite–metal layers, fiber orientation, and boundary conditions. In this investigation, free-clamp boundary conditions are used on the edges.

The sample analyzed in this research is a six-layer FML shell consisting of two layers made of aluminium and four layers made of glass/epoxy. This work employs a laminate coding technique to define the FML laminates. The coding system of the FML shell consists of six layers, denoted as AL/GE-i-j, [m,n,o,k]. A case study of a laminate FML shell is defined by the variables: i=2, j=4, m=n=0, o=k=90, and AL/GE-2-4. In this shell, the second and fourth layers are constructed of aluminium, while the other layers are made of glass/epoxy. The fibre orientation of the layers is [0,0,90,90] degrees, respectively. AL is an abbreviation for aluminium, whereas GE stands for glass-epoxy. The arrangement of metal and composite layers, as well as the orientation of composite layers, in the FML shell are from the inside to the outside. An example of a 3-layer FML (Fibre Metal Laminate) shell consists of layers of AL/Glass-Epoxy/Glass-Epoxy with a [0/90] angle configuration. The interior surface is composed of aluminium, the second layer is made of glass/epoxy with a 0-degree angle, and the outside layer is built of glass/epoxy with a 90-degree orientation.

2.2. Procedure of Calculation of FML Shell Reliability

In this study, the Hashin yield criterion to calculate the FML shell stability was applied. Then the reliability of the shell using shell stability was determined. In composite shells, increasing the stress to more than critical stress causes imperfection rather than serious fracture because the yield stress should be greater than critical stress. With continued loading, the defect in composite shells expands inch by inch, causing the shell to crack. In this study, it is assumed that the fracture of one layer causes the fracture of the entire laminate, hence the top level of permitted loading is defined by the fracture of one layer. For reliability study, the initial step should be modeling the FML laminate shell in finite element software, then subjecting this shell to constant static load and calculating the stress of the matrix and fiber failure threshold for each layer.

For stress analysis, Abaqus software is used. In the second stage, this information is used for a Matlab program to generate β reliability criteria for each failure mode of fiber and matrix based on an algorithm explained in the next portions. Finally, the reliability of the shell is assessed using the normal distribution table and the reliability criterion.

In this article, g_f and g_m fiber and matric fracture criteria are respected. However, X_T, X_C, Y_T, Y_C, S are random basic variables. S is shear strength, Y_C is bearing strength along the vertical line of fiber, Y_T is tensile strength along the vertical line of fiber, X_C is bearing strength along of fiber, X_T is tensile strength along of fiber. Then, the laminate was modeled and analyzed in Abaqus software to derive fiber stress and matric fracture criterion.

2.2.1. Hashin Criteria

The Hashin method divides the failure criteria into four components in order to increase accuracy. These sections include fibers rupture and matrix in tension and compression force. The tensile rupture of fibres caused by shear stresses is equivalent to:

$$\left(\frac{\sigma_{11}}{X_T}\right)^2+\frac{{\sigma_{12}}^2+{\sigma_{13}}^2}{{\sigma_{12}}^2}=\begin{cases}\geq 1\,fail\\ \prec 1 Intact\end{cases} \tag{1}$$

Additionally, fibre compression rupture is:

$$\left(\frac{\sigma_{11}}{X_C}\right)^2=\begin{cases}\geq 1\,fail\\ < 1 Intact\end{cases} \tag{2}$$

Matrix tensile rupture in case of $\sigma_3+\sigma_2 \succ 0$ is:

(3)

$$\frac{\sigma_{22}^2+\sigma_{33}^2}{Y_T^2}+\frac{\sigma_{23}^2+\sigma_{22}\sigma_{33}}{S_{23}^2}+\frac{\sigma_{12}^2+\sigma_{13}^2}{S_{12}^2}=\begin{cases}\geq 1\, fail\\ <1 Intact\end{cases}$$

For Matrix tensile rupture if $\sigma_3+\sigma_2 \prec 0$:

$$\left[\left(\frac{Y_C}{2S_{23}}\right)^2-1\right]\left(\frac{\sigma_{22}+\sigma_{33}}{Y_C}\right)+\frac{\sigma_{22}^2+\sigma_{33}^2}{4S_{23}^2}+\frac{\sigma_{23}^2+\sigma_{22}\sigma_{33}}{S_{23}^2}+\frac{\sigma_{12}^2+\sigma_{13}^2}{S_{12}^2}=\begin{cases}\geq 1\, fail\\ <1 Intact\end{cases} \tag{4}$$

In the aforementioned Equations, σ_3 represents lateral shear resistance and is equivalent to the permissible shear tension in the (3-2) plane. Conversely, the permissible shear tension in the (3-1) plane can be regarded as equal to that in the (2-1) plane, denoted as S. The Hashin criteria under plane tension conditions in the tension coordinate system are represented in “Fig. 1”, illustrating the principal directions of the material.

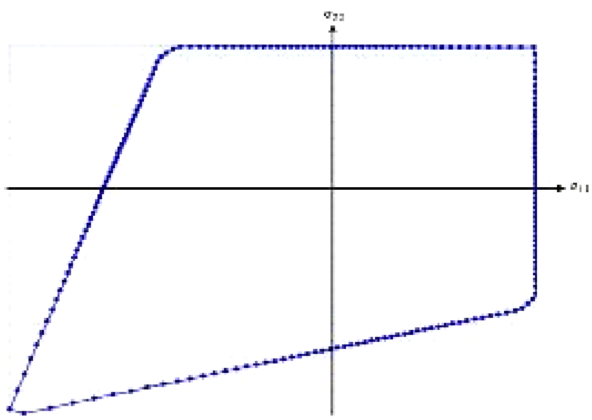

Fig. 1 Hashin criteria in plane shear tension condition

2.2.2. First Order Reliability Method

This work uses the first-order reliability method to calculate the reliability of FML shells. Some explanations for this strategy are presented as follows. The function G(X) is defined as an operation function, where $X=\left[X_1, X_2, \ldots, X_n\right]$ is a vector of random variables for this function. The region of g(x)>0 is a safe zone, the region of g(x) <0 is a failure zone and the region of g(x) =0 is a boundary zone. Reliability is defined as:

The probability of X random variables being in such a way that the operation function is in the safe zone (g(X)>0). If the probability density function of the X variable is $f_X(X)$, the probability of failure is defined as:

$$P_f=P\{g(X)<0\}=\int_{g(X)<0} f_x(x)dx \tag{5}$$

And reliability is calculated as:

$$R=1-P_f=P\{g(X)>0\}=\int_{g(X)>0} f_x(x)dx \tag{6}$$

The probability density function is typically nonlinear, and the integration limits of g(X) are multidimensional and nonlinear. Thus, the first-order reliability method uses intricate computations. These complex functions are the linear approximation of integration limits and the probability density function $f_X(X)$. Typically, tailor series are employed for these functions. The first-order reliability method is used from first-order multinomial for approximation. The first-order reliability method can be summarized as follows:

- Converting the main random variable from the x zone to the normal standard zone
- Search of MPP (Most Probable point) in U zone and calculating β reliability index
- Calculating reliability as follows:

$$R=\phi(\beta) \tag{7}$$

The choice of the probability density function can be made based on the nature of the problem, such as normal, lognormal, Weibull, gamma, etc.

2.2.3. Rosenblatt Transformation

This section presents the Rosenblatt Transformation. This function is utilized to attain reliability. In the first step, the random variable from the x zone, $X=\lfloor X_1, X_2, \ldots, X_n \rfloor$, should be transformed to standard normal zone. When the zone is changed, the probability density functions become regular. There are random variables in the U zone, $U=\lfloor U_1, U_2, \ldots, U_n \rfloor$, that follow a normal distribution. This transformation is true if the random variable cumulative distribution function is to be fixed after and before transformation. This transformation is named Rosenblatt Transformation.

Finally, the probability density function (PDF) for the normal distribution, denoted as Ø(U), has been obtained.

$$\phi_U(u)=\prod_{i=1}^{n}\frac{1}{\sqrt{2\pi}}\exp\left(-\frac{1}{2}u_i^2\right) \tag{8}$$

$$P_f=\int\int g(u_1,u_2,\ldots,u_n)\prod_{i=1}^{n}\frac{1}{\sqrt{2\pi}}\exp\left(-\frac{1}{2}u_i^2\right)du_1du_2\ldots du \tag{9}$$

3 PROCEDURES OF OPTIMIZATION OF FML CYLINDRICAL SHELL

The design variable in this study is the sequence of the composite-metal layers and the fiber orientation of the composite layers in the FML cylindrical shell. The optimization goal is to achieve maximum reliability. Table 1 introduces the parameters of optimization.

Table 1 Introduction parameters used in the optimization process

Parameter name	Parameter definition
M	Number of metal layer of FML shell
N	Number of composite layers of FML shell
R	number of stances of fibers orientation for every layer
S	number of stances of composite–metal layers positioning order
U	number of total stances of fibers orientation for all of the composite layers
N.L.S	Number of considered layers sequences
N.L.U	Number of considered fibers orientation

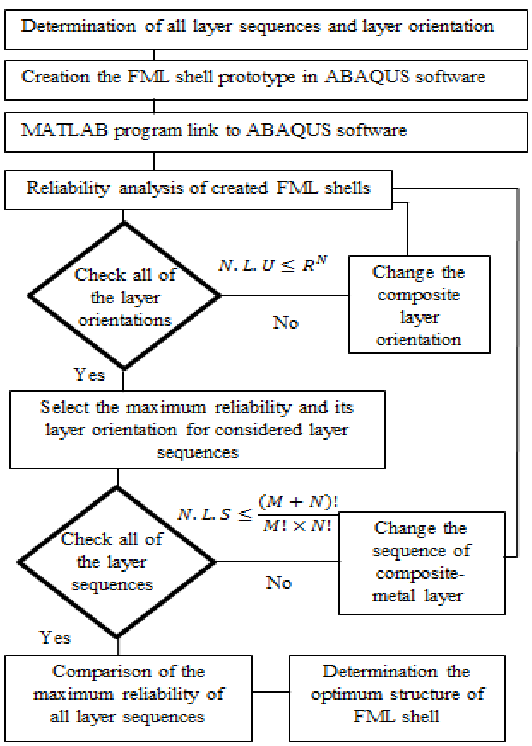

Fig. 2 Flowchart of design and optimization of cylindrical FML shell.

In order to optimize the performance, it is necessary to determine the number of positions for the composite-metal layers in the first step of the optimization method. For this purpose, "Eq. (10)" is used:

$$S = \frac{(M+N)!}{M! \times N!} \tag{10}$$

The number of fiber orientation stances of composite layers should be computed in the second stage using "Eq. (11)".

$$U = R^N \tag{11}$$

The total number of possible structures for an FML cylindrical shell with M metal layers and N composite layers can be found using "Eqs. (10) and (11)". Then, the optimum structure that causes the maximum reliability among all available structures should be determined. The flowchart of the design and optimization of the cylindrical FML shell is illustrated in "Fig. 2". The design constraints are as follows:

Maximize Reliability

$$0 < N.L.S \le \frac{(M+N)!}{M! \times N!} \qquad 0 < N.L.U \le R^N \tag{12}$$

4 GOVERNING EQUATIONS

The dynamic analysis of an optimized FML cylindrical shell employs the equilibrium Equations of the shell, using the First Order Shear Deformation Theory (FSDT) and Love's First Approximation Theory. The purpose of dynamic analysis is the calculated response of the shell under high-frequency sinusoidal load that is applied in a short time. Figure 3 shows a circular cylindrical shell with a mean radius of R, thickness h, and length L. The origin of the orthogonal coordinate system (X, φ, Z) is placed at the mid-surface at the end of the cylinder. The displacement of the cylinder in X φ and Z directions are defined by *u*,*v*, and *w*, respectively.

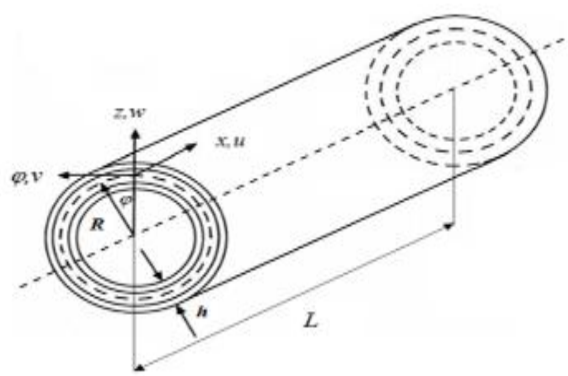

Fig. 3 Geometry of cylindrical shell and the associated coordinate system

The shell deformations are assumed to be small. According to first-order shear deformation theory, the equilibrium Equations for a cylindrical shell are as follows:

$$\frac{\partial N_x}{\partial x} + \frac{1}{R}\frac{\partial N_{x\varphi}}{\partial \varphi} = I_1 \frac{\partial^2 u}{\partial t^2} + I_2 \frac{\partial^2 \theta_x}{\partial t^2} \tag{13}$$

$$\frac{\partial N_{x\varphi}}{\partial x}+\frac{1}{R}\frac{\partial N_{\varphi}}{\partial \varphi}+\frac{Q_{\varphi}}{R}=\left(I_1+\frac{2I_2}{R}\right)\frac{\partial^2 v}{\partial t^2}+\left(I_2+\frac{I_3}{R}\right)\frac{\partial^2\theta_{\varphi}}{\partial t^2}$$
$$\frac{\partial Q_x}{\partial x}+\frac{\partial Q_{\varphi}}{\partial \varphi}-\frac{N_{\varphi}}{R}+q_r\left(x,\varphi,t\right)=I_1\frac{\partial^2 w}{\partial t^2}$$
$$\frac{\partial M_{x\varphi}}{\partial x}+\frac{\partial M_{\varphi}}{\partial \varphi}-Q_{\varphi}=\left(I_2+\frac{I_3}{R}\right)\frac{\partial^2 v}{\partial t^2}+I_3\frac{\partial^2\theta_{\varphi}}{\partial t^2}$$
$$\frac{\partial M_x}{\partial x}+\frac{\partial M_{x\varphi}}{\partial \varphi}-Q_x=I_2\frac{\partial^2 u}{\partial t^2}+I_3\frac{\partial^2\theta_x}{\partial t^2}$$

In the above Equations θ_x and θ_{φ} are the slopes in planes of x-z and $\varphi-z$ respectively. Also q_r is the external force that excites the shell.
The correlations between the force resultants and the stress components of the shell are as follows:

$$\left(N_x,N_{\varphi},N_{x\varphi},Q_x,Q_{\varphi}\right)=\int_{-\frac{h}{2}}^{\frac{h}{2}}\left(\sigma_x,\sigma_{\varphi},\sigma_{x\varphi},\sigma_{xz},\sigma_{\varphi z}\right)dz \tag{14}$$

The relationship between the moment resultants and the stress components of the shell is as follows:

$$\left(M_x,M_{\varphi},M_{x\varphi}\right)=\int_{-\frac{h}{2}}^{\frac{h}{2}}\left(\sigma_x,\sigma_{\varphi},\sigma_{x\varphi}\right)zdz \tag{15}$$

In Equation (13), the mass inertia is defined by the following relation:

$$\left(I_1,I_2,I_3\right)=\int_{-\frac{h}{2}}^{\frac{h}{2}}\rho_k\left(1,z,z^2\right)dz \tag{16}$$

In “Eq. (16)”, ρ_k is the density of each layer. Damping terms are excluded from the equilibrium Equations in the transient dynamic response analysis for the specified loading circumstances since the effect of structural damping is negligible. The stress-strain relations for a cylindrical shell are as follows:

$$\left\{\sigma_x,\sigma_{\varphi},\sigma_{x\varphi},\sigma_{xz},\sigma_{\varphi z}\right\}^T=\left[\overline{Q_{ij}}\right]\left(\varepsilon_x,\varepsilon_{\varphi},\varepsilon_{x\varphi},\varepsilon_{xz},\varepsilon_{\varphi z}\right)^T \ \& \quad i,j=1,2,4,5,6 \tag{17}$$

$\overline{Q}_{ij}$ is the reduced stiffness matrix. The strain components in “Eq. (17)” are defined under Love's first approximation theory as follows:

$$\varepsilon_x=\varepsilon_x^0+z\kappa_x \qquad \varepsilon_{\varphi}=\varepsilon_{\varphi}^0+z\kappa_{\varphi} \qquad \varepsilon_{x\varphi}=\gamma_{x\varphi}^0+2z\kappa_{x\varphi}$$
$$\varepsilon_{xz}=\gamma_{xz}^0 \qquad \varepsilon_{\varphi z}=\gamma_{\varphi z}^0 \tag{18}$$

Strain and curvature are associated with the displacement component of the cylindrical shell according to Love's first approximation theory as follows:

$$\left\{\varepsilon_x^0,\varepsilon_{\varphi}^0,\varepsilon_{x\varphi}^0\right\}=\left\{\frac{\partial u}{\partial x},\frac{1}{R}\frac{\partial v}{\partial\varphi}+\frac{W}{R},\frac{1}{R}\frac{\partial u}{\partial\varphi}+\frac{\partial v}{\partial x}\right\}$$
$$\left\{\kappa_x,\kappa_{\varphi},\kappa_{x\varphi}\right\}=\left\{\frac{\partial\beta_x}{\partial x},\frac{1}{R}\frac{\partial\beta_{\varphi}}{\partial\varphi},\frac{1}{R}\frac{\partial\beta_x}{\partial\varphi}+\frac{\partial\beta_{\varphi}}{\partial x}\right\} \tag{19}$$
$$\left\{\gamma_{xz}^0,\gamma_{\varphi z}^0\right\}=\left\{\beta_x+\frac{\partial W}{\partial x},\beta_{\varphi}+\frac{1}{R}\frac{\partial W}{\partial\varphi}-\frac{V}{R}\right\}$$

The boundary conditions for the cylindrical shell contain a combination of clamped and free conditions at its curving edges on both ends.

$$@\,x=L,N_x=\left(N_{x\varphi}+\frac{M_{x\varphi}}{R}\right)=\left(Q_x-\frac{\partial M_{x\varphi}}{R\partial x}\right)=M_x=0$$
$$@\,x=0,u=v=w=\beta_x=\beta_{\varphi}=0 \tag{20}$$

To fulfil the boundary conditions, u, v, w, β_x and β_{φ} are expressed by double Fourier series as follows:

$$u=\sum_m\sum_n A_{mn}\frac{d\eta_u\left(x\right)}{dx}\cos n\varphi T_{mn}\left(t\right)$$
$$v=\sum_m\sum_n B_{mn}\eta_V\left(x\right)\frac{d}{dx}\sin n\varphi T_{mn}\left(t\right)$$
$$w=\sum_m\sum_n C_{mn}\eta_w\left(x\right)\cos n\varphi T_{mn}\left(t\right)$$
$$\beta_x=\sum_m\sum_n D_{mn}\frac{d\eta_{\beta_x(x)}}{dx}\cos n\varphi T_{mn}\left(t\right) \tag{21}$$
$$\beta_{\varphi}=\sum_m\sum_n E_{mn}\eta_{\beta_x(x)}\sin n\varphi T_{mn}\left(t\right)$$
$$\eta_{i(x)}=\alpha_1\cosh\frac{\lambda_m x}{L}+\alpha_2\cos\frac{\lambda_m x}{L}-\sigma_m\left(\alpha_3\sinh\frac{\lambda_m x}{L}-\alpha_4\sin\frac{\lambda_m x}{L}\right)$$
$$\left(i=u,v,w,\beta_x,\beta_{\varphi}\right)$$

In “Eq. (21)”, T_{mn} is the function of time, also, A_{mn}, B_{mn}, C_{mn}, D_{mn}, E_{mn} are the constant coefficients of the natural mode shapes. These numbers are related to the free vibration problem and are found by using the fact that mode shapes are orthogonal to the mass matrix. M is the axial half-wave number and n is the circumferential wave number. The values of α_i, σ_m and λ_m in “Eq. (21)” can be derived from the relevant boundary conditions.

5 TRANSIENT VIBRATION ANALYSES

This section defines external excitation and calculates the transient response of the acceleration and displacement components.

5.1. Definition of Dynamic Loading Condition

The term $q_r\left(x,\varphi,t\right)$ in "Eq. (13)" is the external force that excites the shell. The area of applied load $\left(2L_1 \times 2L_2\right)$ is variable and the coordinates of the center point of this area $\left(x_L \times \varphi_L\right)$ can be everywhere on the shell as:

$$\begin{aligned} &x_2 - x_1 = 2L_2 \quad R\left(\psi_2 - \psi_1\right) = 2L_1 \quad x_L = \left(x_2 + x_1\right)/2 \\ &\varphi_L = \left(\psi_2 + \psi_1\right)/2 \end{aligned} \tag{22}$$

The dynamic sinusoidal loading that stimulates the shell is delineated according to "Eq. (23)".

$$F(t) = 100\sin(5500t) \qquad 0 \le t \le 0.05 \tag{23}$$

The superposition approach is employed for dynamic analysis. This method transforms a continuous system into a discrete N-DOF linear system with a defined mode shape. The node displacement was characterised by the N component at an arbitrary time, with the u vector representing the node displacement. The Equations of motion are articulated by the mathematical statement provided in "Eq. (24)".

$$M\ddot{u}\left(t\right) + C\dot{u}\left(t\right) + ku\left(t\right) = p\left(t\right) \tag{24}$$

Where M is the mass matrix, C is the system viscous damping matrix and K is stiffness matrix in generalized coordinates U and p(t) is harmonic force and (.) denotes differentiation for time. The initial stage in a mode superposition solution involves determining the natural frequencies and natural modes of the system that fulfill the algebraic eigenvalue problem. The pivotal stage in the mode-superposition method is to implement the coordinate transformation.

$$u\left(t\right) = \sum_{m=1}^{N} \phi_m q_m\left(t\right) \tag{25}$$

The coordinates $q_m\left(t\right)$ will be referred to as principal coordinates or modal coordinates. "Eq. (25)" is substituted into "Eq. (24)" and the resulting Equation is multiplied by ϕ_m. To derive the Equation of motion in principal coordinates, solve "Eq. (26)" for each mode shape to determine the node displacement of the shell, using "Eq. (23)".

$$\sum_{m=1}^{N} M\phi_m \ddot{q}_m\left(t\right) + C\phi_m \dot{q}_m\left(t\right) + k\phi_m q_m\left(t\right) = p\left(t\right) \tag{26}$$

To solve the dynamic response issue, equilibrium Equations are incorporated into the strain-displacement and curvature-displacement relationships. Consequently, the resultant Equations may be expressed in the following manner:

$$\left[L_{ij}\right]\left\{u,v,w,\beta_x,\beta_\theta\right\} = \left\{0,0,q_r,0,0\right\}^T \qquad ij = 1,....,5 \tag{27}$$

The applied impulsive load is defined as:

$$q_r\left(x,\varphi,t\right) = \sum_{m=1}^{\infty}\sum_{n=0}^{\infty} P_{mn} \sin\lambda x \cos n\varphi\, f\left(t\right) \tag{28}$$

In "Eq. (28)", $f(t)$ is function of time, P_{mn} is the constant Fourier coefficient that is calculated from the position, size, and profile of the applied load. The Galerkin method is employed to obtain a solution for "Eq. (27)".

6 VALIDATIONS OF THE RESULT

The mode convergence should be verified to ensure the validity of the result. In order to obtain the correct dynamic analysis response, the number of modes must be determined so that the structure response remains constant as the number of modes changes. This study assumes the maximum acceleration at the endpoint of the cylindrical shell in the w direction to evaluate the response convergence of the shell structure. In the current research, evaluating the response convergence for two distinct shell structures, the number of modes is set to 100, as increasing the number of modes beyond 100 does not change the structure's response. Figure 4 illustrates the convergence of responses from two distinct shells.

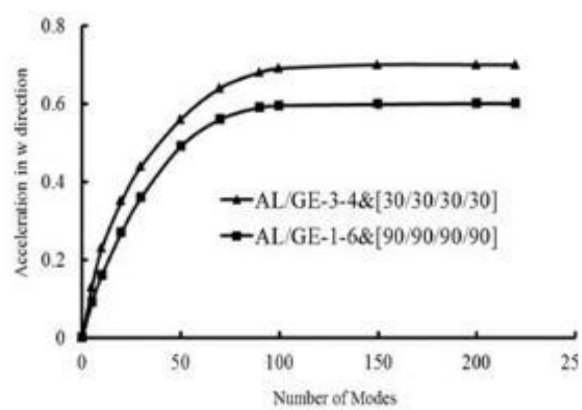

Fig. 4 Mode convergence plot

The validity and precision of the current study are evaluated by comparing the results with the transient dynamic response of clamp-free hybrid composite circular cylindrical shells as presented by Malekzadeh and Khalili [6], illustrated in "Fig. 5". Dynamic analysis of a three-layer composite shell subjected to sinusoidal loading is taken into account for this purpose. Results are obtained for a clamped-free cylindrical shell with stacking sequence [45/0/45], the geometries of the considered shell are radius=2m, length =6m, and similar thickness for every layer=1mm. The material properties of the composite shell that was employed for the validation are demonstrated in “Table 2”.

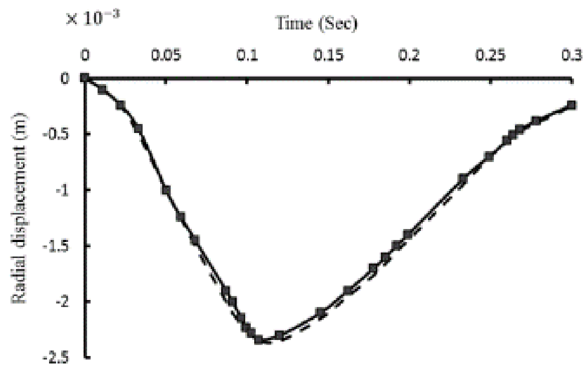

Fig. 5 Comparison of the dynamic analysis of composite shell (—■—present study,- - - Malekzadeh and Khalili [6]).

Table 2 Material properties used for composite shell for validation

ρ (kg/ m)	G12 (Gpa)	G23 (Gpa)	J_{12}	E_{22} (Gpa)	E_{11} (Gpa)
1643	4.1	1.3	0.26	7.6	19.0

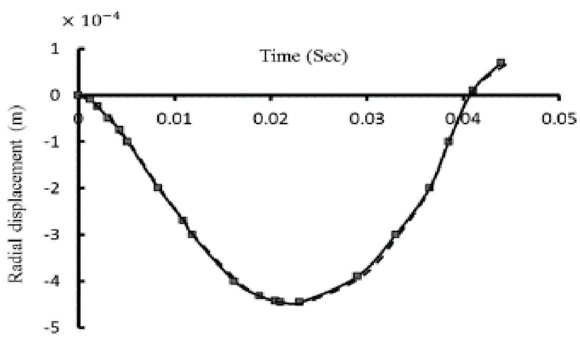

Fig. 6 Comparison of the dynamic analysis of FML shell (—■—present study,- - - Malekzadeh and Khalili [6]).

Additionally, a five-layer FML shell with a construction of AL/GFRP 0° / AL/GFRP 0° /AL] is considered for the validation of the dynamic response of the FML shell The results are compared with the transient dynamic response of clamp-free hybrid composite circular cylindrical shells as presented by Malekzadeh and Khalili [6]. In “Fig. 6”, the geometries of the considered shell are radius=0.6m, length =2m, and similar thickness for every layer=2mm. Table 3 displays the material properties of the FML shell that was employed for this verification.

Table 3 Material properties used for FML shell for validation

material	ρ (kg/m^3)	G12 (Gpa)	G23 (Gpa)	J_{12}	E_{22} (Gpa)	E_{11} (Gpa)
GFRP	1390	1.8	0.69	0.35	5.1	14.34
Al 2024	2770	28	28	0.33	72.4	72.4

For this optimization process, an FML shell with two layers of aluminium and four layers of glass-epoxy is used. Table 4 shows the qualities of the material that was used to make this FML shell.

Table 4 Aluminum and glass/epoxy properties used for FML shells

material	density (kg/m^3)	Shear module (Gpa)	Poison ratio	Elastic module (Gpa)
Aluminum	$\rho = 2700$	G_{12}=27.8 G_{13}=27.8 G_{23}=27.8	$\vartheta_{12} = 0.3$ $\vartheta_{13} = 0.3$ $\vartheta_{23} = 0.3$	E_{11}=72.4 E_{22}=72.4 E_{33}=72.4
Glass-epoxy	$\rho = 2500$	G_{12}=4.7 G_{13}=4.7 G_{23}=3.28	$\vartheta_{12} = 0.25$ $\vartheta_{13} = 0.25$ $\vartheta_{23} = 0.42$	E_{11}=50 E_{22}=15.2 E_{33}=15.2

7 DETERMINATIONS OF SIX-LAYER FML SHELL OPTIMAL STRUCTURE UNDER CLAMP-FREE BOUNDARY CONDITION

Tables 5 and 6 present the maximum and minimum reliability indices, the corresponding maximum and minimum reliability values, and the fibre orientations that yield maximum and lowest reliability for all lay-up configurations of the six-layer FML shell.

The findings of the reliability analysis for the FML shell considered in this study, as presented in “Tables 5 and 6”, indicate that the AL/GE-1-6 & [0/0/0/90] structure has the highest reliability, while the AL/GE-3-4 & [90/90/90/90] structure has the lowest reliability. Figure 7 shows the level of reliability for the best and worst structures of the FML cylindrical shells under consideration in this study.

Table 5 Comparison of the maximum reliability criteria and maximum reliability of clamp-free FML cylindrical shell for different kinds of layer sequences

Lay up	Maximum reliability criteria	Layer orientation that causes maximum reliability	Maximum reliability
AL/ GE-1-2	2.8611	0/0/0/90	99.77%
AL/ GE-1-3	2.7943	0/0/0/90	99.73%
AL/ GE-1-4	2.7957	0/0/0/90	99.74%
AL/ GE-1-5	2.8738	0/0/0/90	99.78%
AL/ GE-1-6	2.877	0/0/0/90	99.79%
AL/ GE-2-3	2.5763	90/0/0/90	99.50%
AL/ GE-2-4	2.577	90/0/0/90	99.50%
AL/ GE-2-5	2.7765	90/0/0/90	99.72%
AL/ GE-2-6	2.8122	90/0/0/0	99.75%
AL/ GE-3-4	2.5079	90/0/0/90	99.39%
AL/ GE-3-5	2.5369	90/0/0/90	99.44%
AL/ GE-3-6	2.7828	90/0/0/0	99.73%
AL/ GE-4-5	2.522	90/0/0/90	99.41%
AL/ GE-4-6	2.679	90/0/0/0	99.63%
AL/ GE-5-6	2.7889	90/0/0/0	99.73%

Table 6 Comparison of the minimum reliability criteria and minimum reliability of clamp-free FML cylindrical shell for different kinds of layer sequences

Lay up	Minimum reliability criteria	Layer orientation that causes minimum reliability	Minimum reliability
AL/ GE-1-2	1.3065	90/90/90/90	90.43%
AL/ GE-1-3	1.3072	90/90/90/90	90.44%
AL/ GE-1-4	1.3097	60/60/30/30	90.48%
AL/ GE-1-5	1.311	60/60/60/30	90.5%
AL/ GE-1-6	1.3131	60/60/60/30	90.54%
AL/ GE-2-3	1.2953	90/90/90/90	90.23%
AL/ GE-2-4	1.3034	90/90/90/90	90.37%
AL/ GE-2-5	1.3088	30/60/60/30	90.46%
AL/ GE-2-6	1.3107	60/60/60/30	90.5%
AL/ GE-3-4	1.2939	90/90/90/90	90.21%
AL/ GE-3-5	1.3064	90/90/90/90	90.42%
AL/ GE-3-6	1.3095	90/90/90/90	90.48%
AL/ GE-4-5	1.302	90/90/90/90	90.35%
AL/ GE-4-6	1.3081	90/90/90/90	90.45%
AL/ GE-5-6	1.3087	90/90/90/90	90.46%

Figure 8 shows the amount of reliability for four different layer sequences. It should be observed that the fibre orientation for the four different layer sequences depicted in "Fig. 8" is the same, specifically [60/30/0/90]. As can be seen in "Fig. 8", changing the fiber–metal layers sequence causes to high variation of shell reliability.

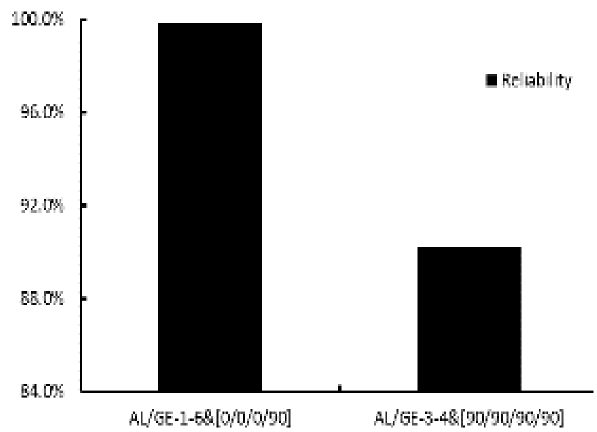

Fig. 7 Variation of reliability of FML cylindrical shell for the best and worst construction under free-clamp boundary conditions.

Figure 9 shows the effect of varying the composite layer orientation on the reliability of the FML shell under consideration in this work. Also, "Fig. 9" shows that changing the orientation of the composite layer has a small effect on the FML shell's reliability.

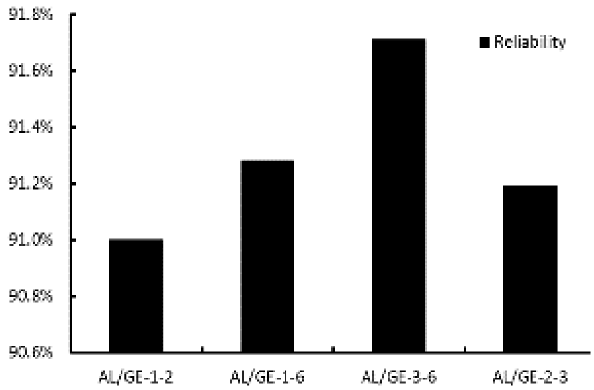

Fig. 8 Comparison of FML cylindrical shell reliability with [60,30,0,90] layup for four various layer sequences.

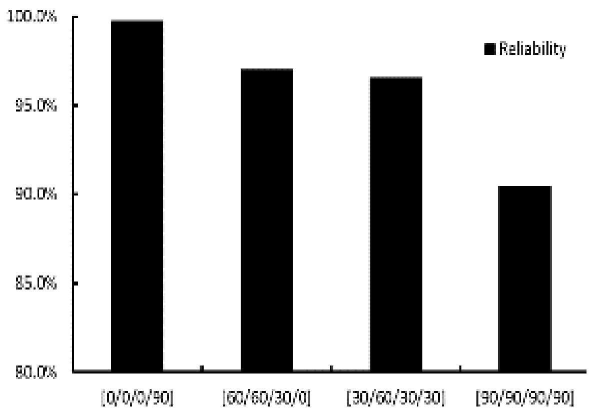

Fig. 9 Comparison of reliability of FML cylindrical shell with AL/GE-3-4-layer sequences for four various layer orientations.

The displacement variation of the best and worst FML shell structures under dynamic loading in the *u*, *v*, and *w* directions is shown in “Figs. 10-12” of this study.

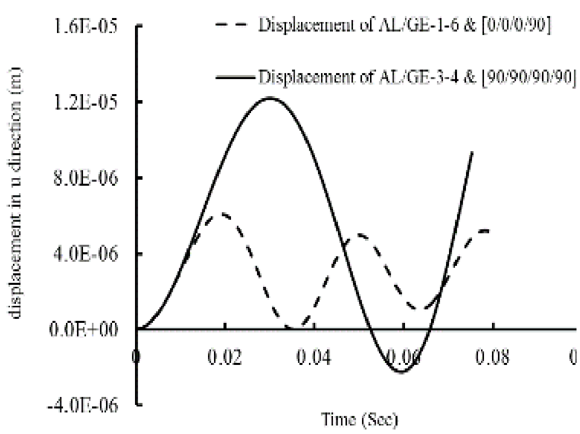

Fig. 10 Variation of displacement at the endpoint of FML cylindrical shell for the best and worst structure in the u direction.

Based on the data presented in “Fig. 10”, it can be estimated that the displacement of the AL/GE-1-6 & [0/0/0/90] structure is approximately 130% smaller than that of the AL/GE-3-4 & [90/90/90/90] structure in the u direction. Based on the information shown in “Fig. 11”, it can be inferred that the displacement of the AL/GE-1-6 & [0/0/0/90] structure is about 160% smaller than that of the AL/GE-3-4 & [90/90/90/90] structure in the vertical direction (v direction).

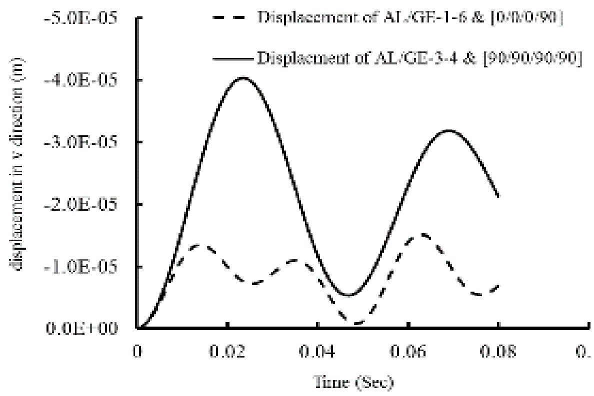

Fig. 11 Variation of displacement at the endpoint of FML cylindrical shell for the best and worst structure in v direction.

Figure 12 shows that the displacement of the AL/GE-1-6 & [0/0/0/90] structure in the w direction is approximately 130% smaller than that of the AL/GE-3-4 & [90/90/90/90] structure. Also, the analysis of Figures 10-12 indicates that optimizing the structure of the FML shell has a significant impact on the displacement of the FML shells when subjected to dynamic loading.

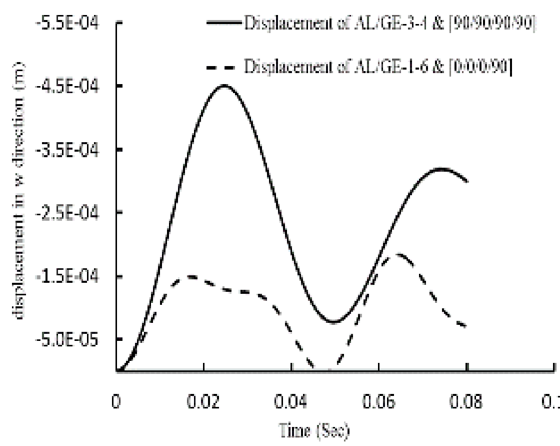

Fig. 12 Variation of displacement at the endpoint of FML cylindrical shell for the best and worst construction in w direction.

\

In this study, the FML shell's acceleration reaction in *u*, *v*, and *w* directions for the best and worst structures in terms of reliability is shown in “Table 7”.

Table 7 Comparison of the acceleration at the endpoint of FML cylindrical shell for the best and worst structure in a) u, b) v, c) w directions

Shell structure	Maximum acceleration in u direction	Maximum acceleration in v direction	Maximum acceleration in w direction
AL/GE-1-6 & [0,0,0,90]	1.63e-6	6.75e-6	6.07e-8
AL/GE-3-4 & [90,90,90,90]	1.77e-6	7.03e-6	7.08e-8

Table 7 indicates that, in the u, v, and w directions, respectively, the acceleration of the AL/GE-1-6 & [0/0/0/90] structure is approximately %8, %4, and %16 less than that of the AL/GE-3-4 & [90/90/90/90] structure.

8 CONCLUSIONS

In this paper, transient vibration analyses of optimized Fiber Metal Laminates Cylindrical Shells were studied. Energy method is used to derive the Equations of motion and the mode superposition method is utilized for transient vibration analysis. The free-clamp boundary conditions are used on the edges in the present study. The first-order reliability method and Hashin failure criteria are used to determine the FML shell reliability. For this purpose, the shell is subjected to constant static load, and the resulting tensions within FML layers of the shell are measured. In the second part of this study, the effect of the optimized structure of the FML shells on the acceleration and displacement of these shells under dynamic loads are investigated. The results of this study can be summarized as follows:

- One of the most significant innovations of this work is the development of a valuable approach for optimising FML shells based on maximum reliability.
- A program is developed using MATLAB to optimise the performance. This program is coupled to the ABAQUS finite element software.
- The optimisation procedure of this study considers an FML shell consisting of 2 aluminium layers and 4 glass-epoxy layers. The best structure for maximum reliability is AL/GE-1-6 & [0/0/0/90], while the worst structure for minimum reliability is AL/GE-3-4 & [90/90/90/90].
- The displacement variation for the best and worst FML shell structures is illustrated in Figures 10, 11, and 12, corresponding to the u, v, and w directions, respectively. The figures indicate that optimising the FML shell structure significantly improves the displacement of these shells under dynamic loads.

REFERENCES

[1] Lee, Y., Lee, K. D., On the Dynamic Response of Laminated Circular Cylindrical Shells Under Impulse Loads, Journal of Computers & Structures, Vol. 35, 1997, pp. 149-57.

[2] Lam, K. Y., Loy, C. T., Influence of Boundary Conditions for A Thin Laminated Rotating Cylindrical Shells, Compos Struct, Vol. 41, 1998, pp. 215–28.

[3] Chen, Li., Transient Dynamic Response Analysis of Orthotropic Circular Cylindrical Shell Under External Hydrostatic Pressure, J Sound Vib, Vol. 257, 2002, pp. 967–76.

[4] Karagiozova, D., Langdon, G. S., Nurick, G. N., and Kim Yuen, C., Simulation of the Response of Fiber-Metal Laminates to Localized Blast Loading, Int. J. Impact Eng, Vol. 37, 2010, pp. 766-82.

[5] Khalili, S. M. R., Malekzadeh, and K., Davar, A., Dynamic Response of Pre-Stressed Fiber Metal Laminate (FML) Circular Cylindrical Shells Subjected to Lateral Pressure Pulse Loads, Journal of Composite Structures, Vol. 92, 2010, pp. 1308-17.

[6] Malekzadeh, K., Khalili, S. M. R., and Davar, A., Transient Dynamic Response of Clamp-Free Hybrid Composite Circular Cylindrical Shells, Journal of Apply Composite Material, Vol. 17, 2010, pp. 243-57.

[7] Darabi, M., Non-Linear Dynamic Instability Analyzes of Laminated Composite Cylindrical Shells Subjected to Periodic Axial Loads, Composite Structures, Vol. 147, 2016, pp. 168–84.

[8] Haichao, A., Chen, S., Huang, H., Simultaneous Optimization of Stacking Sequences and Sizing with Two-Level Approximations and A Genetic Algorithm, Composite Structures, Vol. 123, 2015, pp. 180–89.

[9] Sen, I., Alderliesten, R. C., and Benedictus, R., Design Optimization Procedure for Fiber Metal Laminates Based on Fatigue Crack Initiation, Journal of Composite Structures, Vol. 120, 2015, pp. 275-284.

[10] Haeri, A., Fadaee, M., Efficient Reliability Analysis of Laminated Composites Using Advanced Kriging Surrogate Model, Composite Structures, Vol. 149, 2016, pp. 26–32.

[11] Malakzadeh Fard, K., Pourmoayed, A., Dynamic Stability Analysis of FGM Beams Based on the Nonlinear Timoshenko Model, Journal of Computational Methods in Engineering, Vol. 42, 2023, pp. 63-76.

[12] Ma, Q., Merzuki, M. N. M., Rejab, M. R. M., Sani, M. S. M., and Zhang, B., A Review of The Dynamic Analysis and Free Vibration Analysis on Fiber Metal Laminates (FMLs), Functional Composites and Structures, Vol. 5. 2023, pp. 012003.

[13] Azarafza, R., Davar, A., Analysis and Optimization of Fibre-Metal Laminate Cylindrical Shells Subjected to Transverse Impact Loads, AUT Journal of Mechanical Engineering, Vol. 4, 2020, pp. 535-52.

[14] Zamani, M., Davar, A., Beni, M. H., and Jam, J. E., Transient Dynamic Analysis of Grid-Stiffened

Composite Conical Shells, Journal of Solid Mechanics, Vol. 14, 2022.

[15] Davar, A., Azarafza, R., Eskandari Jam, J., and Labbafian Mashhadi, A., Low-Velocity Impact Response Analysis of Laminated Composite Cylindrical Shells Subjected to Combined Pre-Loads, Journal of Stress Analysis, Vol. 6, 2021, pp. 139-56.

[16] Alibeigloo, A., Talebitooti, M., Three Dimensional Transient Coupled Thermoelasticity Analysis of FGM Cylindrical Panel Embedded in Piezoelectric Layers, Mechanics of Smart Structures, Vol. 1, 2020.

[17] Khalili, S. M., Dehkordi, M. B., and Shariyat, M., Modeling and Transient Dynamic Analysis of Pseudoelastic SMA hybrid composite beam, Applied Mathematics and Computation, Vol. 219, 2013, pp. 9762-82.

[18] Pourmoayed, A., Malakzadeh Fard, K., and Rousta, B., Free Vibration Analysis of Sandwich Structures Reinforced by Functionally Graded Carbon Nanotubes, Compos. Mater. Eng, Vol. 3, 2021, pp. 1-23.

[19] Fu, Y., Hu, S., Nonlinear Transient Response of Fibre Metal Laminated Shallow Spherical Shells with Interfacial Damage Under Unsteady Temperature Fields, Composite Structures, Vol. 106, 2013, pp. 57-64.